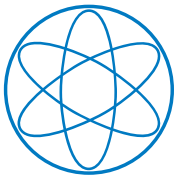

Technische Universität München
Fakultät für Physik

Characterization of Radiation Damage in Tungsten

Barbara Dorota Wieluńska

Vollständiger Abdruck der von der Fakultät für Physik der Technischen Universität München zur Erlangung des akademischen Grades eines

Doktors der Naturwissenschaften

genehmigten Dissertation.

Vorsitzende: Prof. Dr. Nora Brambilla

Prüfer der Dissertation:

1. Prof. Dr. Rudolf Neu
2. Prof. Dr. Peter Böni
3. Prof. Dr. Małgorzata Lewandowska

Die Dissertation wurde am 18.12.2019 bei der Technischen Universität München eingereicht und durch die Fakultät für Physik am 16.03.2020 angenommen.

Abstract

Tungsten is a promising plasma-facing material for a future fusion reactor due to its low erosion yield, high melting point and low hydrogen solubility. However, irradiation by energetic neutrons created by the fusion processes will induce radiation defects in the material, which can strongly increase hydrogen retention. Therefore, it is important to understand the mechanism of defect creation and its influence on hydrogen retention in tungsten. Neutron displacement damage is often simulated by irradiations with high mass ions. It is not clear to what extent the displacement damage created by the different ion species in tungsten is comparable among the different ion species themselves and to what extent it resembles that of neutrons. To study the radiation damage and D retention behavior caused by irradiation with different ions, polished and recrystallized tungsten samples were irradiated with H, D, He, Si, Fe, Cu, W at energies between 0.3 and 20 MeV. As different ions with different energies were used, the primary recoil spectra and damage rates were also different. Hence, the effect of the primary recoil energy spectrum and the damage rate on damage creation and deuterium uptake could be investigated. The displacement damage in tungsten irradiated by the here used ions was calculated using SRIM. At low damage levels, D retention in self-damaged tungsten increases linearly with the damage level. At higher damage levels, the D retention saturates. In order to represent the linear and the saturation regimes, two different damage levels of 0.04 dpa and 0.5 dpa (in the damage maximum) were used. The microstructure of the damage zone was investigated by transmission electron microscopy (TEM) and positron annihilation lifetime spectroscopy (PALS). For TEM observations, single crystalline tungsten samples were used to ensure the same crystal orientation during the ion irradiations and subsequent observations. Lamellas perpendicular to the sample surface were prepared to image the damage depth profile. The tungsten samples were observed under four different two-beam diffraction conditions. The damage zone of tungsten irradiated by Si and W up to 0.04 dpa and 0.5 dpa was investigated, as representatives for medium to high mass ions. In the 0.04 dpa case, the damage zone consists of small dislocation loops and dislocation loop clusters. The difference in the average loop size was up to 20%. In the 0.5 dpa samples, a

dislocation line network was found. The difference in the dislocation line density between Si-irradiated and self-irradiated tungsten was about 10%. Compared to the differences in ion energy and ion mass, these differences are small. Hence, a similar damage zone can be expected for the other heavy ions. By comparison with the SRIM calculated damage depth profile, a loop-to-line transition was found to happen at about 0.08 - 0.1 dpa in these samples.
Tungsten was irradiated by H, D, He up to 0.04 dpa and only by He up to 0.5 dpa. The damage zone showed significant differences compared to the damage zone obtained by the higher mass ion irradiations. In the damage zone three to four distinct subzones were observed. The thicknesses of these zones and the appearance of the zone found in the region of the damage peak were ion dependent. Tungsten irradiated by He to 0.04 dpa and 0.5 dpa did not show the loop-to-line transition.
Positron annihilation lifetime spectroscopy was performed with 16 to 18 keV energetic positrons on polycrystalline tungsten samples irradiated by the different ions. No significant difference in the open-volume defect structure in tungsten irradiated by medium to high mass ions was found.
For studying the hydrogen retention in defects polycrystalline, damaged tungsten samples were exposed to a low-temperature D plasma at 370 K sample temperature to decorate the defects. The D depth distribution was measured with nuclear reaction analysis (NRA) using the D(^{3}He, p)α reaction and D desorption spectra were derived by thermal desorption spectroscopy (TDS). The region of increased D retention seen in the D depth profiles is in good agreement with the damage range calculated by SRIM and the damage range seen in TEM. Tungsten irradiated by medium to high mass ions (Si, Cu, Fe, W) up to 0.5 dpa shows similar D depth profiles. Tungsten irradiated by He shows a significantly different D depth profile with a higher D concentration in the peak. From the comparison of the measured D depth profiles with the SRIM damage depth profiles, it was found that the D saturation is already reached at 0.13 - 0.15 dpa. Tungsten irradiated by medium to high mass ions shows also very similar deuterium desorption spectra in the 0.04 dpa and 0.5 dpa case, i.e. the D retention is comparable. Despite the large differences in the recoil energy spectra between the different medium to high mass ion irradiations, the microstructure and D retention obtained was always similar. For tungsten irradiated by light ions (H, D, He), the D desorption spectra show significant differences in the low to medium temperature range between 400 - 700 K. From this work it can be concluded that both the microstructure and the D retention behavior of tungsten irradiated by different medium to high mass ions (Si, Fe, Cu, W) is identical for high damage levels (>0.2 dpa) and similar for low damage levels (<0.1 dpa).

Contents

Chapter 1

Introduction

The world's energy demand is continuously growing and predicted to increase by 28% from 2016 to 2040 [1]. The energy demand is growing fast, especially in China and India. Today, beside the limited fossil fuel resources (oil, gas, coal), renewable energies (water power, solar, wind, biomass) and fission are available. Renewable energy sources (solar and wind energy) suffer from discontinuous availability and limited storage capacity. Fission has an unsolved radioactive waste problem, and, at least in Germany, is missing public acceptance. Therefore, developing a sustainable and clean mid- and long-term energy strategy becomes more and more important [1]. Nuclear fusion is a potential sustainable source of energy and a potential solution for the world energy problem [2, 3].

In a future fusion reactor the power will be obtained by a nuclear reaction between deuterium (D) and tritium (T). The products of the reaction are helium atoms and neutrons carrying a substantial amount of energy. This fusion reaction is most promising as it has a high value of the reaction parameter at relatively low energies, i.e., a relatively low plasma temperature is needed compared to the other fusion reactions of hydrogen isotopes[4]. To initiate the fusion reaction, the D-T fuel has to be heated up to about 10–20 keV (corresponding to 150 MK) to overcome the Coulomb repulsion. At such high temperatures the fuel is in the plasma sate. It will be heated by ohmic heating, neutral beam injection and high frequency electromagnetic waves. The energy released by the nuclear reactions can be used to maintain the hot plasma and to produce electricity [4]. As no material is able to withstand such high temperatures, the plasma is kept away from the reactor wall by a strong magnetic field (magnetic confinement). Today's tokamak experiments have reached the plasma temperatures and densities needed for fusion. However, the sizes of these devices is too small to gain energy as the thermal losses of the plasma are too

high, to achieve a burning plasma. Nevertheless, the tokamak Joint European Torus (JET) at Culham, UK reached about 60% of the fusion power needed to maintain the plasma temperature [5, 6]. The International Thermonuclear Experimental Reactor (ITER) is the next generation tokamak being built in Cadarache, France. It should demonstrate a ten times higher power production by fusion than the external heating power. The Demonstartion Power Plant (DEMO) should be the last step before building a commercial fusion reactor and should demonstrate fuel self-sufficiency and electrical power production [6].

One key issue in the successful fusion reactor operation is the plasma-wall interaction [7]. Even with good magnetic confinement, there are areas where the edge of the plasma comes into contact with the reactor wall. This is necessary to allow pumping of the fusion reaction product helium, which otherwise would accumulate and dilute the fuel, degrading the fusion efficiency. In modern devices the magnetic field lines guide the edge of the plasma towards a specially designed region of the wall, the so called divertor to allow the pumping of He. Hence, plasma-wall interactions are not avoidable, but an integral part of the plant operation [8]. The divertor is subjected to significantly higher particle and heat fluxes than the rest of the wall. In ITER, the expected typical ion and neutral particle fluxes at the divertor plasma strike point are above $10^{24}\,\mathrm{m^{-2}s^{-1}}$. This corresponds to total fluences over $10^{26}\,\mathrm{m^{-2}}$ for each ITER pulse. The expected surface temperatures around the divertor strike point are between 800 K and 1300 K, depending on the exact localization [7]. Hence the plasma-facing materials and components have to withstand these high particle fluxes and temperatures. The plasma interaction with the plasma-facing materials can strongly influence the plasma operation. The erosion of the plasma-facing materials limits their lifetimes and the impurities entering the plasma cool down the plasma and dilute it. Deposition on the plasma-facing materials change their surface and hence their properties. Dust generation due to erosion is also an important operational and safety issue. For radiation safety, it is important to keep the T retention as low as possible. In ITER, the total in-vessel T inventory has to be kept below 700 g [7].

Among several candidates, tungsten is a promising plasma-facing material due to its low sputtering yield, high melting temperature and low hydrogen retention. The hydrogen retention in tungsten varies from below 10^{-4} for single crystalline W and $3{\cdot}10^{-3}$ at.% for polycrystalline W [9]. As discussed above, tungsten will be exposed to high fluxes of energetic deuterium and tritium ions, atoms and molecules as well as to high fluxes of 14 MeV neutrons from the DT-fusion reaction. This n irradiation will produce defects in the tungsten crystal lattice in which hydrogen isotopes can be

retained, resulting in an increase of the hydrogen retention in damaged tungsten by orders of magnitudes compared with the undamaged material [10]. Understanding the nature and development of radiation damage in tungsten and the hydrogen isotopes retention in n irradiated tungsten is, therefore, a key issue for the safe operation of future fusion devices.

To investigate the material response under fusion neutron irradiation, a high flux 14 MeV neutron source is needed. Unfortunately, such a source is not yet available. Fission neutrons have a significantly different energy spectrum compared with fusion neutrons, with an average energy of < 2 MeV. Therefore, they can be used only to a certain extent to investigate the effects of n irradiation in a future fusion reactor. Moreover, experiments with tungsten damaged by fission neutrons are typically difficult to conduct because of the long exposure times in a fission reactor and the long cooling-down times due to the activation of the samples. Additionally, such irradiations are often not well defined in terms of temperature and dose rate [11]. Ion irradiation is comparatively fast and does not activate the samples. Different ion species with keV - MeV energies are used to simulate the fusion neutron displacement damage in tungsten. According to [12–14] heavy ions are a good proxy for neutrons as they generate dense collision cascades with large defect clusters which is also typical for neutron irradiation. In hydrogen isotopes retention studies, ion irradiation has been used for many years to create displacement damage in tungsten. D retention in tungsten was extensively studied at different damage levels and different ion fluences and fluxes [15–19]. As various ions at different energies are used, the primary tungsten recoil energy spectrum for the damage creation is also different. This may affect the damage distribution and consequently the D uptake. It is an open question to what extent the displacement damage and the resulting D retention in tungsten irradiated by different ions is comparable with each other and with displacement damage created by neutrons. The aim of this thesis is to characterize the radiation damage in tungsten caused by different ions and to correlate the observed microstructure to the obtained D retention. A detailed description of the aims and used techniques is found in Sect. 2.5.

Chapter 2

Background

2.1 Radiation damage

The first wall and divertor of a future fusion reactor will be subjected to large fluxes of energetic ions and neutral atoms from the plasma and fast neutrons (with energies up to 14 MeV) originating from fusion reactions. These particles, impinging on the wall, cause radiation damage. Energetic neutrals and ions will cause radiation damage up to a few μm depth due to their higher stopping power. The 14 MeV neutrons, however, exhibit only a small stopping power in the material and can cause radiation damage throughout the bulk of the material. The incident particles collide with the plasma-facing target atoms, either elastically or inelastically. Elastic collisions lead to atomic displacements, called displacement damage, which result in lattice defects. Inelastic collisions can lead to transmutations.

2.1.1 Lattice defects

Fig. 2.1 shows the main types of lattice defects: vacancies, interstitials, vacancy and interstitial clusters, and dislocations [20]. Some of these defects are intrinsic, like vacancies, dislocations, grain boundaries, pores, etc. Others can be, for example, a consequence of the irradiation of the material with energetic particles (radiation damage). Interstitials in tungsten are already mobile at room temperature and migrate to sinks, such as dislocations, grain boundaries and surfaces or form clusters. There are two types of dislocations: edge dislocations and screw dislocations shown in Fig. 2.2 a and Fig. 2.3 a. These two types can either be of vacancy-type or interstitial-type, shown in Fig. 2.1 [20, 21]. The crystallographic orientation of a dislocation is described by the Burgers vector **b**. A Burgers circuit in a crystal lattice containing a dislocation is a closed loop connecting atom to atom. It is drawn in Fig. 2.2 a and Fig. 2.3 a as the circuit MNOPQ containing the dislocation. When transferring the same circuit into a dislocation free lattice, the loop will not close, compare Fig. 2.2 b, Fig. 2.3 b. The vector **QM**, required to close the circuit in this dislocation free lattice, is called Burgers vector **b** and is an important parameter to describe the crystallographic orientation of a dislocation.

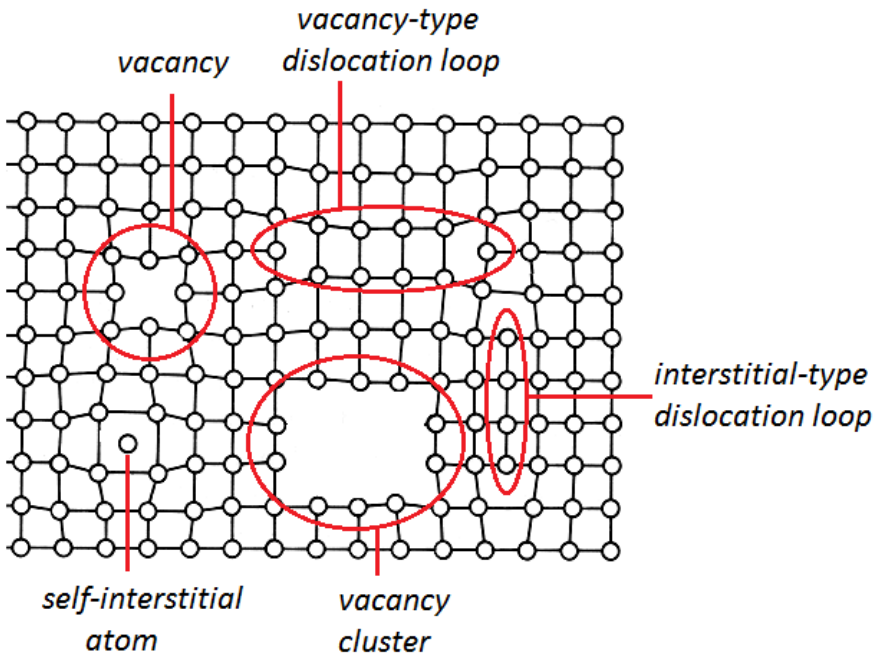

Fig. 2.1: Main types of lattice defects [20].

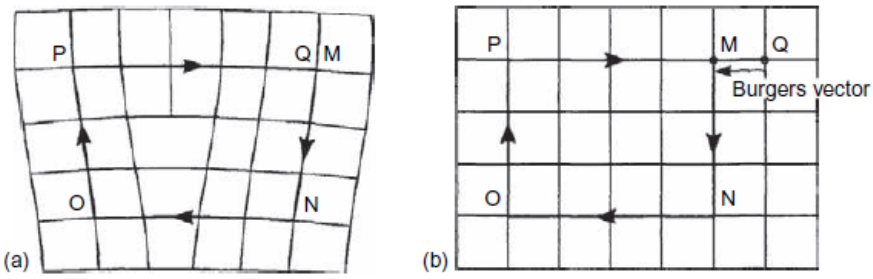

Fig. 2.2: a) Burgers circuit around an edge dislocation. b) The same circuit drawn in a perfect crystal does not close. The vector needed to close the circuit is the Burgers vector. *Reprinted from "Introduction to dislocations", D. Hull and D. J. Bacon, Elsevier Ltd, (2011), with permission from Elsevier [21].*

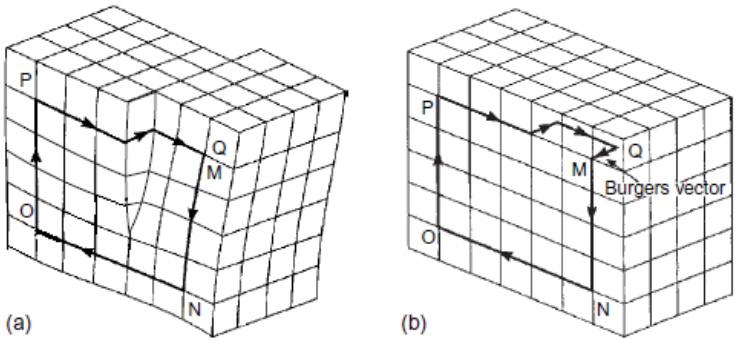

Fig. 2.3: a)Burgers circuit around an screw dislocation. b) The same circuit drawn in a perfect crystal does not close. The vector needed to close the circuit is the Burgers vector. *Reprinted from "Introduction to dislocations", D. Hull and D. J. Bacon, Elsevier Ltd, (2011), with permission from Elsevier [21].*

2.1.2 Displacement damage

An impinging energetic particle can undergo elastic collisions with target atoms. A target atom hit by the incident particle, which receives enough energy to leave its lattice site, is called primary recoil. This primary recoil itself undergoes elastic collision and will displace further target atoms and so on if its kinetic energy is high enough. The initial energy is dissipated in about 100 fs [22].

Whether a recoil is produced in a collision depends on the amount of energy transferred during the collision event. The average threshold energy E_d in metals, for permanently displacing atoms, is typically in the range of 10-50 eV [12, 23]. If the atom receives a kinetic energy $E \geq E_d$, it is permanently displaced.

This threshold energy depends on the crystallographic direction. The average value is the effective displacement threshold energy. In tungsten the threshold energies

for the main crystallographic directions ⟨100⟩, ⟨111⟩, ⟨110⟩ were determined experimentally to be 42 eV in ⟨100⟩, 44 eV in ⟨111⟩, and 70 eV in ⟨110⟩ direction [24]. This gives an effective threshold energy of 55.3 eV [24]. Despite of these experimentally determined values, the American Society for Testing and Materials (ASTM) recommends using 90 eV for the effective threshold energy in tungsten [25]. This value has been used in many studies and is also used for reasons of comparability for all damage calculations in this thesis.

One aim of collision cascade theory is to calculate the number of recoils N(E,T) with initial kinetic energies between T and T+dT produced by a primary recoil slowing down from energy E [22, 26]. In a collision, the primary recoil with energy E transfers the kinetic energy T to the target atom. The target atom will be permanently displaced if the transferred kinetic energy T minus the binding energy to the lattice site E_b is larger than the threshold energy E_d for displacing atoms: $T - E_b \geq E_d$. The incident ion will continue to move if its energy E minus the transferred energy T is larger than the energy E_c needed to capture a slow projectile by a vacant lattice site: $E - T \geq E_c$. With this, two inequalities the multiplication threshold energy can be defined as [22, 26]:

$$L = E_b + E_c + E_d \tag{2.1}$$

When the energy of the incident particle is larger than the multiplication threshold ($E \geq L$) two particles are moving after a collision. If $E < L$, only one particle moves after the collision as the other is captured by the vacant lattice site. With this, the total number of displaced atoms $\nu(E)$ can be calculated [22, 26]:

$$\nu(E) = 1 + \int_L^E N(T, E)dT \tag{2.2}$$

The leading term in Eq. 2.2 is the primary recoil and the integral describes the secondary, tertiary... recoils, i.e. the multiplication by the cascade [22].

Under the assumption of hard-sphere scattering for $E \gg T$, transport theory gives:

$$\lim_{T/E \to 0} N(T, E) = \frac{cE}{T^2} \text{ with } c = 1 \tag{2.3}$$

Inserting Eq. 2.3 in Eq. 2.2 gives:

$$\nu(E) = cE/L \tag{2.4}$$

This result assumes that deviations from Eq. 2.3 are negligible when T→ E. As the number of low energetic recoils is much higher than the number of high energetic recoils this assumption is justified. Kinchin and Pease [12, 22, 27] used hard sphere scattering with c=1 and chose E_b=0 and $E_{cut} = E_d$. It was assumed that at energies

higher than the cut-off energy E_{cut}, the recoils will loose their energy entirely through electronic stopping. Below E_{cut}, electronic stopping is ignored and only hard-sphere elastic collisions with target atoms occur. This results in Eq. 2.4 with $L = 2E_d$ and gives the Kinchin Pease (KP) model for atomic displacements [12, 22, 27].

$$\nu(E) = \begin{cases} 0 & E < E_d, \\ 1 & E_d < E < L, \\ \frac{E}{L} & L < E < E_{cut}, \\ \frac{E_{cut}}{2E_d} & E_{cut} < E < \infty \end{cases} \quad \text{with } L = 2E_d \tag{2.5}$$

This equation was further refined by Norgett, Robinson and Torrens (NRT) due to results of computer simulations using binary collision approximation. It was found that L should be defined as $L = 2E_d/0.8$. The new factor was found to be energy and material independent. This is called the modified Kinchin Pease equation or NRT equation [22, 26, 28].
Knowing the total number of displaced atoms, one can easily calculate the displacement per atom, called dpa, which is the number of displaced atoms divided by the number of material atoms in the same volume:

$$dpa = \frac{Number\,of\,displaced\,atoms}{Number\,of\,material\,atoms\,in\,this\,volume} \tag{2.6}$$

The number of displaced atoms is calculated either with the Kinchin Pease (KP) or the Norgett Robinson Torrens (NRT) model.
The dpa concept is well known and widely used due to its simplicity. However, it has been shown experimentally that the actual defect concentration found in a material after irradiation is not identical to the dpa value but is usually much smaller [29]. This is the case because the assumptions made in this model are only justified for temperatures at 0 K, when no subsequent defect migration occurs.
Molecular dynamics (MD) simulations can give a deeper understanding of collision cascades. In MD simulations the evolution of the trajectories of interacting atoms with time is calculated by numerical solving of Newton's equations of motions. By using interatomic potentials, the forces between the interacting atoms and the potential energies are determined. MD simulations are very close to reality. A significant drawback of these simulations is their long computing time. Usually, these kinds of simulations are limited to timescales of below 1 μs [30, 31].

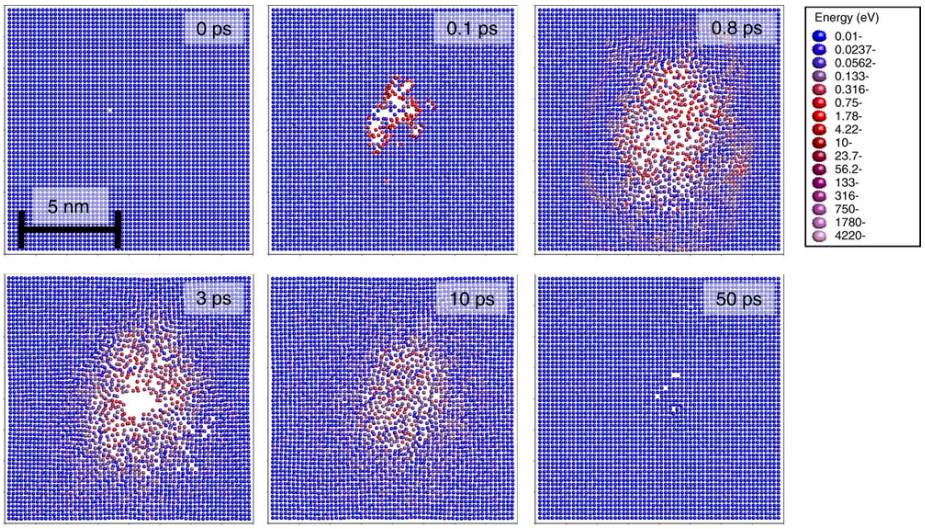

Fig. 2.4: MD simulation of a cascade in gold initiated by a 10 keV gold recoil at a material temperature of 0 K [29, 32]. The subimages illustrate the time evolution of a cascade. The dots indicate the atom positions and their color stands for their kinetic energy. It can be recognized that a large number of atoms is displaced in the first stage of the cascade. During the cooling down of the cascade, almost all displaced atoms recombine with vacant sites. *Reprinted from "Improving atomic displacement and replacement calculations with physically realistic damage models", K.Nordlund et al., Nature Communications, (2018), open access article (CC BY license)[32].*

Fig. 2.4 [29] shows the temporal evolution of a collision cascade initiated by a 10 keV gold primary recoil in gold. In the first 0.2 ps, a huge number of atoms is displaced through ballistic collisions. The number of displaced atoms is similar to the prediction of the NRT equation. Through subsequent collisions between the displaced atoms the collision cascade becomes a heat spike. A heat spike is a dense region of many body collisions which is underdense in the center of the cascade and overdense at the cascade tails. It eventually has a Maxwell-Boltzmann like distribution of kinetic energies and lasts for a few tens of picoseconds. After this phase, the heat spike cools down within a few ps which can be seen as a recrystallisation process, i.e. the crystal anneals (interstitials and vacancies recombine). Hence, the remaining radiation damage is much smaller than the primary damage in the cascade, as can be seen in the last image of Fig. 2.4 [29, 32].
Therefore, the dpa concept can not be interpreted as the actual defect concentration but should be understood as a measure of radiation exposure, which simplifies the comparison between different particle irradiations (neutrons, protons, ions).
MD simulations of collision cascades in tungsten gave a better understanding of the mechanisms in a collision cascade. A. Sand conducted several MD simulations of

150 keV collision cascades in tungsten using different interatomic potentials [33, 34]. It was found that the extent of the molten area in a cascade measured after 250 ps corresponds well to the final damage distribution. Large self-interstitial clusters are found around the molten area. Single self-interstitial atoms are found further outside this region. Vacancy and vacancy clusters are located in the cascade core. At 150 keV, no subcascades were found, nevertheless, the molten area of the cascades was strongly elongated which is a sign that the energy was very close to the threshold energy for cascade fragmentation.
In the MD simulations both vacancy type and self-interstitial type dislocation loops were calculated to exist. Dislocations with b=$\langle 100 \rangle$ and b=$\langle 111 \rangle$ were found as a result of the collision cascade [33, 34]. However, no dislocations of type b=$\langle 110 \rangle$ were observed in the simulations. The in-situ TEM study using 150 keV self-irradiated tungsten performed by [35, 36] confirmed the results of the simulations.
It was found that the distribution of defects as a function of their size is following a power law up to around 300 point defects constituting a cluster. For larger clusters a deviation from the power law was observed [37, 38]. The power law size scaling and the upper size limit was confirmed by in-situ TEM studies at temperatures of 30 K at low doses. As at such low temperatures, the lattice defects had reduced mobility and the observation of the initial damage after a cascade was possible [39]. Due to the short timescales of MD simulations effects like long time defect evolution can not be simulated. All above described MD calculations were conducted at 0 K, hence thermal activated defect mobility was not taken into account.

2.1.3 Thermal evolution of radiation defects

At higher temperatures additionally defect migration plays an important role. Interstitials and vacancies can migrate in the material by thermally activated diffusion and annihilate at surfaces, grain boundaries and dislocations. They can also recombine or agglomerate to more stable defects such as vacancy clusters, interstitial clusters or dislocation loops [12, 40]. There are five defect annealing stages known in irradiated metals. Stage I is the onset of self-interstitial mobility, which is found to be at around 100 K in tungsten. Stage II corresponds to the mobility and/or dissociation of small interstitial clusters and is found to be between 100 K and 620 K in tungsten. Stage III stands for the onset of vacancy migration and its onset is found to be at about 620 K in tungsten. The higher stages are still under discussion, Stage IV may stand for the migration or dissociation of vacancy impurity clusters. The onset temperature for stage IV in tungsten is at about 910 K. Stage V

corresponds probably to the dissociation of defect clusters or formation of voids. Stage V starts at about 1240 K in tungsten [40, 41]. Hence, at room temperature the interstitials in tungsten are mobile. There are many studies about radiation damage in tungsten and its recovery. TEM is a powerful tool to characterize the radiation damage. Dislocations, voids and defect clusters can be observed in irradiated tungsten. The defect evolution in irradiated tungsten was studied by many authors with transmission electron microscopy at different temperatures, just to name few:[35, 36, 40, 42–44]. Nonetheless, TEM studies provide only a part of the sought information due to its limited resolution of 1 nm, i.e. single vacancies and small clusters are not visible in TEM. Therefore, there are many studies of the defect evolution at different temperatures with Positron Annihilation Spectroscopy [45–48]. Defect annealing studies were also performed analyzing the D retention in irradiated tungsten. Through analyzing the D retention with nuclear reaction analysis and thermal desorption spectroscopy conclusions about the defect microstructure and its evolution at different temperatures can be made [49, 50].

2.1.4 Transmutations

Elastic collisions of the incident particles in the material result in displacement damage, discussed in Sect. 2.1.2. Inelastic collisions can result in nuclear reactions. However, the energy of the neutral atoms and ions reaching the first wall or the divertor in a fusion reactor is in general too low to undergo nuclear reactions. Hence, they collide inelastically only with electrons.
Neutrons, however, can induce various nuclear reactions with tungsten resulting in long reaction chains. Gilbert et al. [51] calculated the elemental composition of pure W after 5-full-power years (5 x 365 d) irradiation in DEMO. Fig. 2.5 shows the result of the calculation. Beside significant concentrations of Re and Os also Ta, Hf and other elements are found. For all W isotopes, the main reactions with a high cross section are the (n,γ) and (n, 2n) reactions. The (n,γ) reactions are dominant for low energetic neutrons with energies below 100 keV whereas the (n 2n) reactions become dominant above 1 MeV neutron energy [52]. This changes the original material and its properties. E.g., the addition of 5% Re to pure W reduces the thermal diffusivity by half. The development of precipitations can change the materials properties dramatically [53, 54]. Problematic are also the nuclear reactions that produce gaseous products like helium and hydrogen. Due to the low solubility of He in W, He bubbles form which can lead to substantial swelling of the material [55]. Another problem is that some of the created nuclids are radioactive thus activating

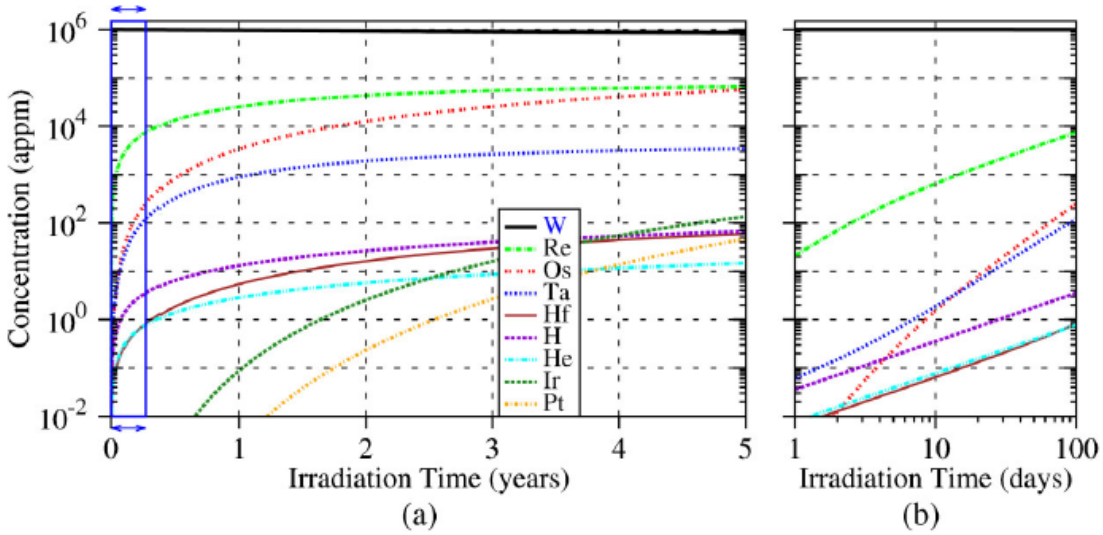

Fig. 2.5: Transmutations of pure W during 5 full-power years neutron irradiation in DEMO first wall conditions. *Reprinted from "Inventory Simulations under Neutron Irradiation: Visualization Techniques as an Aid to Materials Design", Nuclear Science and Engineering 177 p. 291, M. R. Gilbert et al., Taylor & Francis (2014), Taylor & Francis reuse for dissertations [51].*

the material. The induced radioactivity of W in a fusion reactor is mainly due to ^{186}Re. Around 100 years of cooling down will be required in order to sufficiently reduce the activity of W armor from a fusion reactor [52].

2.2 Neutron energy spectra of a fusion and fission reactor

The 14 MeV fusion neutrons are producing radiation damage throughout the material. Therefore, one key issue in fusion research is to understand the materials behavior under such energetic neutron irradiation [11]. The response of the material to neutron irradiation depends on the exact neutron flux and energy spectrum. Gilbert et al. [55] calculated neutron energy spectra for different areas of DEMO with a neutron transport code (the calculation was done for the DEMO design proposed by CCFE in 2009) and found that they differ depending on the location in the reactor. The flux decreases by several orders of magnitude and the energy spectrum becomes softer with increasing distance of the plasma-facing component from the plasma core. This shows the complexity of the problem and demonstrates that carefully designed calculations and experiments are needed to understand the

Irradiation parameter	DEMO first wall 3 MW/m^2	IFMIF high flux test module	HFR position F8
n total flux [1/cm^{2}s]	$1.3{\cdot}10^{15}$	$5.7{\cdot}10^{14}$	$3.8{\cdot}10^{14}$
Damage [dpa/fpy]	30	20-55	2.5
H [appm/fpy]	1240	1000-2400	1.9
He [appm/fpy]	320	250-600	0.8

Table 2.1: Displacement damage and gas production in iron for different neutron irradiation facilities [14]

materials response.

To investigate the material response on fusion neutron irradiation dedicated facilities are required. No fusion reactor is available nowadays which is operating with D-T fuel and producing the typical fusion neutron energy spectrum. Unfortunately, also no 14 MeV neutron source with sufficient large fluxes is available. The International Fusion Materials Irradiation Facility (IFMIF) is planned to be constructed. IFMIF will produce a neutron flux by the nuclear reaction Li(d,xn) with a broad peak at 14 MeV [56].

Fig. 2.6 shows the calculated neutron energy spectra for the first wall of DEMO and a typical neutron spectrum of a pressurized water fission reactor (PWR) [55]. Significant differences are observed especially at high energies which are dominant in a fusion reactor. Significant fluxes above 12 MeV are observed, resulting in higher damage levels and an increase of the probability for threshold nuclear reactions [55]. The average energy of fission neutrons is typically below 2 MeV. Nevertheless, fission neutrons can be used to study the expected material response in a fusion reactor to some extend. These fission neutrons slow down in the material creating displacement damage similar to fusion neutrons. Transmutations typical for the low energy range can also be studied. One problem of such reactor experiments is the control of the irradiation parameters like flux, temperature, exact irradiation time making the results difficult to interpret. Due to the significantly different energy spectra of fission neutrons these will not produce this high amount of displacement damage and these substantial amounts of gaseous transmutation products (H, He) which are typical for a fusion reactor. Tab. 2.1 shows the expected irradiation parameters of DEMO for the first wall, for IFMIF, and for a fission high flux reactor (HFR). Significant differences in the displacement damage production and gas production between DEMO and HFR reactor are obvious. IFMIF shows more similarity to DEMO [14].

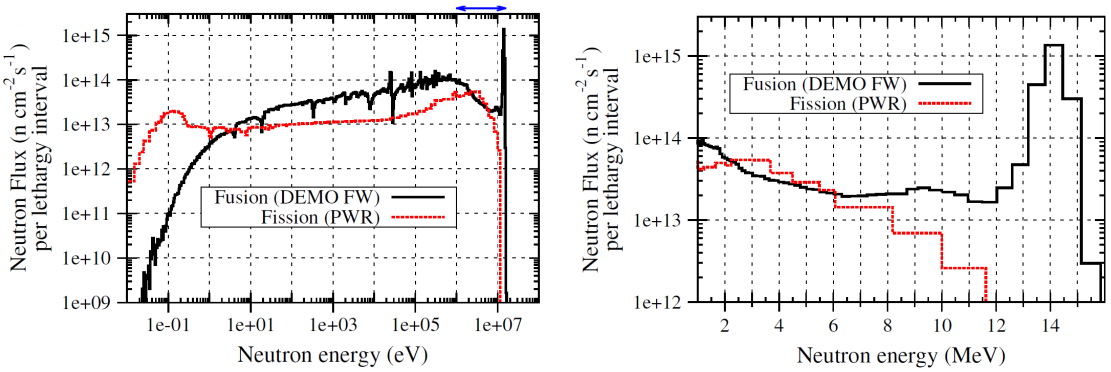

Fig. 2.6: Neutron energy spectra of DEMO for the first wall and a typical neutron spectrum of a pressurized water fission reactor (PWR). The left image is showing the whole energy range in eV. The right image is showing the neutron energy spectrum between 1 - 15 MeV. Note please the change from logarithmic to linear scale. *Reprinted from Publication "Neutron-induced dpa, transmutations, gas production, and helium embrittlement of fusion materials", Journal of Nuclear Materials Vol. 442 pp. 755 - 760, M.R. Gilbert, S.L. Dudarev, D. Nguyen-Manh, S. Zheng, L.W. Packer and J.-Ch. Sublet, Elsevier (2013), with permission from Elsevier* [55].

2.3 Ion irradiation as proxy for neutron irradiation

Due to the lack of a 14 MeV neutron source and the significant differences between the neutron energy spectra of fission and fusion neutrons, ions are often used as proxy for neutrons. The irradiation parameters during ion irradiations are much better defined than in fission reactor neutron irradiations. The knowledge of ion energy, flux, dose rate and irradiation temperature allows fundamental radiation effects studies. It is well known that most of the radiation effects observed in neutron irradiated materials can be reproduced by using different ions [57]. Typical neutron irradiations in fission reactors require 1-3 years exposure time to reach damage levels relevant for fusion research. This is accompanied by activation of the sample which requires at least one year of cooling down time. Such long time spans allow only few irradiations which makes an understanding of the physical phenomena difficult. In contrast to neutron irradiations, ion irradiations are much faster due to the higher damage rate of ions. Damage levels in the range of 1-10 dpa are usually reached within a few to a few ten hours of ion irradiation with little or no induced sample activation. Hence, ion irradiations are much easier to handle, rendering ions an important alternative to neutrons [12].

However, experiments have to be planned carefully taking into account the differences to neutrons. Ions show large differences in the energy deposition along the particle track compared to neutrons. They are slowed down continuously due to electronic stopping and the long range Coulomb interactions. The interaction of neutrons with target nuclei can be well described by hard sphere scattering. Neutrons and target atoms do not interact until the distance between them is equal to the hard sphere radius. These different potentials result in different recoil energy spectra: In a 1 MeV self-ion irradiation of Cu over 80% of the primary recoils have energies below 1 keV, whereas a 1 MeV neutron irradiation of Cu results in about 80% of the primary recoils having energies between 30-60 keV [26, 57].
Also other differences occur between ion irradiation and neutron irradiations. Ion irradiations typically exhibit a high dose rate in comparison to neutron irradiations. This results in different defect arrival rates at sinks (grain boundaries, dislocation, defect clusters). To obtain comparable defect arrival rates at sinks Mansur et al. [58, 59] suggested to perform ion irradiations at higher temperatures than neutron irradiations. In ion irradiation a focused ion beam is often used which rasters the sample surface in order to obtain uniform irradiation. However, it was experimentally shown that using rastered or pulsed beams can result in a different microstructure compared to static ion beam irradiations [60–62]. Gigax et al. [61] observed in self-ion irradiated iron a reduction of swelling due to ion beam rastering. It is predicted that such beam pulse effects vanish at very high frequencies. Hence, care is needed when using pulsed ion beams. When performing ion irradiations, surface effects should also be taken into account as they can change the observed radiation damage discussed in detail by Zinkle et al.[57]. During ion irradiations the ions get implanted in the material thus changing the initial material and its response to radiation [57, 63]. Neutron induced transmutations can not be simulated by ions. In addition to the limited ion damage depth, it is difficult to investigate bulk properties such as thermal conductivity or mechanical properties [57].
When using ions to simulate neutron irradiation, it is important to choose the best suiting ion species for the problem to be investigated.
Let us assume that the displacement damage of 14 MeV neutrons should be investigated. Naively one might assume that protons should be a good proxy for neutrons as they have an almost identical mass. However, the answer depends on the primary recoil energy spectrum. Not the number of recoils of a particular energy is most important but the number of defects produced by every primary recoil is essential. Hence, the primary recoil spectrum has to be weighted by the number of defects produced by the primary recoils. The fraction of defects

produced by the primary recoils is described by the weighted recoil spectrum W(T). As an example, Fig. 2.7 shows the calculated weighted recoil spectrum for neutrons, protons and heavier ions (Ne, Kr) with 1 MeV incident energy in copper [12, 26]. To calculate the weighted recoil spectrum for neutrons or protons, the hard sphere interaction or the Coulomb interaction was used, respectively. The weighted recoil spectra for the other particles were calculated using screened Lindhardt cross section [12, 26]. From Fig. 2.7, one can see that over 70% of the calculated damage from the irradiation with 1 MeV protons are due to primary recoils with energies below 10 keV. In comparison, only 2% of the damage from the irradiation with 1 MeV neutrons originates from primary recoils with energies below 10 keV. Therefore, protons are only a poor proxy for neutrons. Neutrons form dense collision cascade whereas proton irradiation produces mainly small sparse cascades and isolated Frenkel pairs. The weighted recoil spectrum of Ne or Kr shows more similarities to that of neutrons. For 1 MeV Kr irradiation of copper, only up to 30 % of the calculated damage originate from primary recoils with energies below 10 keV (Fig. 2.7). Hence, to simulate displacement damage caused by neutrons heavy ions should be used [12, 26]. However, it is not possible to obtain all aspects of the microstructure with ion irradiation originate from 14 MeV fusion neutron irradiation due to the evident differences between ions and neutrons. Nevertheless, ions provide the opportunity to investigate the very complex radiation processes. Depending on the radiation effect to be investigated different ion species are used. For studying the formation of cavities in materials light ion irradiations like H or He have been used [64–66]. To investigate transmutation reactions in tungsten high energetic proton irradiations can be useful [67]. To understand the displacement damage by neutrons, different heavy ions are widely used [68–71]. There is only a limited number of studies dealing with the comparison of the response of tungsten to different ion irradiations and a systematic work is needed to get a deeper understanding of the radiation damage in tungsten caused by different ion species.

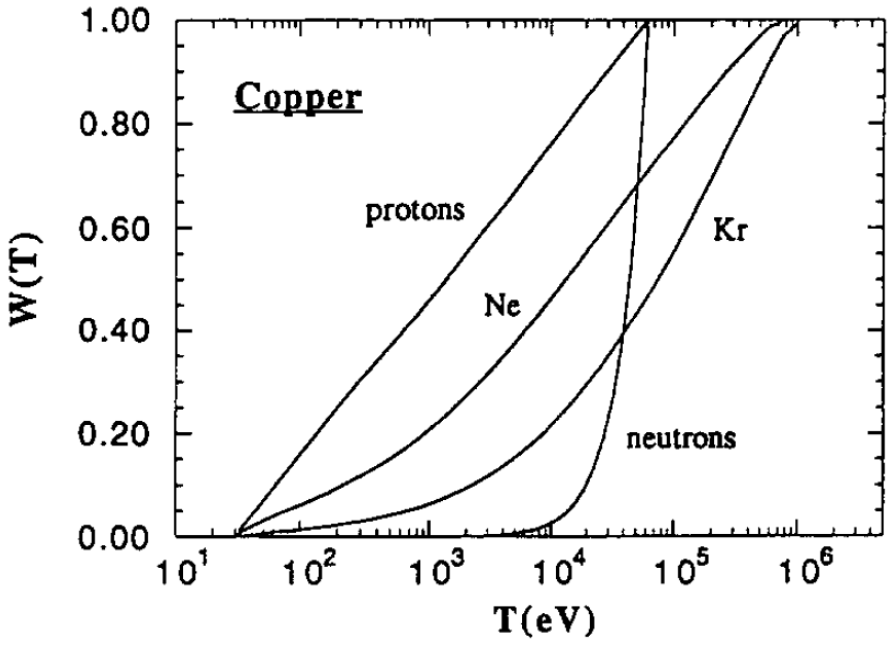

Fig. 2.7: Weighted recoil spectra calculated for different 1 MeV particles in Cu. *Reprinted from "Atomic displacement processes in irradiated metals", Journal of Nuclear Materials 216, p.49 , R.S. Averback, Elsevier (1994), with permission from Elsevier [26].*

2.4 Hydrogen in tungsten

Tungsten is a promising plasma-facing material due to its low sputtering yield, high melting temperature and low hydrogen retention. The hydrogen retention in tungsten ranges from below 10^{-4} at.% for single crystalline W to $3{\cdot}10^{-3}$ at.% for polycrystalline W [9, 72]. In a future fusion reactor it is important to keep the T-retention as low as possible for radiation safety reasons. For example in ITER, the total in-vessel T inventory should be kept below 700 g [7]. Therefore, the hydrogen retention in tungsten is a key issue for safe operation of a future fusion reactor. Tungsten will be exposed to high fluxes of energetic deuterium and tritium ions, atoms and molecules as well as to high fluxes of 14 MeV neutrons from the DT-fusion reaction. The irradiation with D, T ions produces radiation damage in near surface layers while n-irradiation produces radiation damage throughout the whole W bulk. Experiments and atomistic calculations show that lattice defects in metals trap hydrogen [73, 74]. Hence, the hydrogen retention in irradiated tungsten can be increased by several orders of magnitude [10, 75].

Fig. 2.8 shows schematically the potential energy diagram for H in W. The surface is indicated by the dashed, vertical line. The energy of a H_2 molecule is defined to be zero at infinity. As can be seen in Fig. 2.8, the uptake from H in W is endothermal, as the potential energy of hydrogen in the tungsten bulk is higher by ΔE_S compared to the energy of a H_2 molecule in the vacuum ,i.e. it has a positive heat of solution. Molecular hydrogen has to be dissociatively adsorbed at the surface before being absorbed into tungsten, whereas atomic hydrogen can be absorbed directly. The absorption into tungsten requires the energy ΔE_{S-B}. Of course, an absorbed hydrogen atom can enter back into the adsorbed state at the surface and can be released as H_2 after recombination with another adsorbed atomic hydrogen. In the bulk, hydrogen can be either in the solute state or can be trapped in lattice defects. Density functional theory (DFT) calculations show that solute hydrogen occupies tetrahedral interstitial sites [76], which is confirmed by ion channeling experiments [77]. The hydrogen atom jumps from one site to another obtaining the needed energy ΔE_D from thermal oscillations of the atomic lattice. This process is called thermally activated diffusion. The interstitial positions are shallow minima in the potential energy diagram for hydrogen in tungsten. The diffusive flux is described by Fick's first law:

$$\mathbf{J}(\mathbf{r}, t) = -D\nabla C_s(\mathbf{r}, t) \tag{2.7}$$

with D being the hydrogen diffusion coefficient and C(**r**,t) the local concentration of solute hydrogen. There exists only a limited number of studies which determined the solubility and diffusivity of hydrogen in tungsten. It is generally accepted that the hydrogen solubility in tungsten is very low. Frauenfelder's measurements [78] of the solubility and diffusivity are seen as most reliable as the measurements were performed at high temperatures of 1100-2400 K, at which the amount of hydrogen trapped in lattice defects should be negligible. Hence, the solubility in tungsten can be described as:

$$S(T) = 9 \cdot 10^{-3} exp\left(\frac{-1.04\,eV}{k_B T}\right) \quad \left[\frac{H}{W \cdot atm^{1/2}}\right] \tag{2.8}$$

with the heat of solution $E_S = 1.04$ eV and the solubility constant $S_0 = 9 \cdot 10^{-3}$ determined by Frauenfelder [78]. DFT calculation [76, 79] of E_S give a value from 0.86 to 1.04 eV which is in good agreement with [78]. The hydrogen diffusivity is described by the following equation [78]:

$$D(T) = 4.1 \cdot 10^{-7} exp\left(\frac{-0.39\,eV}{k_B T}\right) \quad \left[\frac{m^2}{s}\right] \tag{2.9}$$

with the activation energy for hydrogen diffusion $E_D = 0.39$, and the diffusion constant is $D_0 = 4.1 \cdot 10^{-7}$[78]. DFT calculations [76, 79] of the hydrogen diffusivity give a value of about $E_D = 0.2$ eV which is significantly different to the measured value of 0.39 eV. It was suggested by Heinola et al. [80] to omit the data at 1100 K-1500 K in Frauenfelder's experiment as at these temperatures hydrogen trapping in defects might be not negligible. The extrapolation to low temperatures without these data gives a value of 0.25 eV, much closer to the DFT value.

Due to the low solubility of hydrogen in tungsten, the hydrogen retention is governed by the amount of hydrogen trapped in defects. These defects can be either intrinsic or introduced by neutron/ion irradiation. Hydrogen gets trapped in lattice defects due to the reduced electron density at the lattice defects which attracts hydrogen atoms. Different trap sites have different hydrogen binding energies. Single vacancies trap hydrogen less strongly than vacancy clusters, i.e. the binding energy is smaller. The trap energy ΔE_{Trap} in Fig. 2.8 describes the energy needed to escape the trap. The trapped hydrogen can be released through thermally activated detrapping. Hence, the amount of trapped hydrogen atoms decreases with increasing temperature. The role of individual defects on hydrogen retention is difficult to define as it seems that some defects species have similar trapping energies [81, 82]. The detrapping energy of single vacancies is 1.43±0.02 eV as measured by Eleveld and van Veen [83]. Poon et al. [84] derived a trap energy of 1.34 for the first D atom at a

vacancy, based on modeling of D thermal desorption spectra. Zibrov et al. measured an energy of 1.56±0.06 eV [85]. DFT calculations predict for the detrapping energy values between 1.27-1.79 eV [79, 80, 86, 87]. The DFT calculation show that a single vacancy can trap up to 6-12 hydrogen atoms. With increasing number of trapped hydrogen atoms the detrapping energies decrease [73, 88].
Vacancy clusters bind hydrogen more strongly. Nevertheless, the detrapping energy with respect to the cluster size is unknown. Experimental measurements assign a detrapping energy of about 2.05 eV [89] or 2.1 eV [84, 90]. The detrapping energies assigned to dislocations vary strongly in literature. Ogorodnikova et al. [16] estimated a rather low detrapping energy of 0.85 eV from dislocation and grain boundaries. Manhard [91] assigned an energy of 1.25±0.11 eV to dislocations. The detrapping energy of dislocations depends on the type of the dislocation, whether it is a vacancy type, interstitial type, screw or edge dislocation. In [92] DFT calculations gave a detrapping energy of 0.53 eV for a screw dislocations and 0.89 eV for an edge dislocations. In [93] the upper limit for the binding energy of a H atom to the core of a dislocation was predicted to be 0.97 eV for edge dislocation and 0.57 eV for screw dislocations.
As described above, hydrogen in tungsten can be either in the solute state or trapped in defects. Following equations describe the hydrogen diffusion and trapping in one dimension [46, 94–96]:

$$\frac{\partial C_s(x,t)}{\partial t} = \left(D(T)\frac{\partial^2 C_s(x,t)}{\partial x^2}\right) - \sum_{i=1}^{p}\frac{\partial C_t^i(x,t)}{\partial t} + S(x,t) \tag{2.10}$$

The first term on the right side of in Eq. 2.10 describes the diffusive flux (the solute hydrogen). $D(T)$ is the hydrogen diffusivity (compare Eq. 2.9) and $C_s(x,t)$ is the local concentration of solute hydrogen. The second term gives the temporal variation of the concentration of trapped hydrogen in traps of type i, $C_t^i(x,t)$, summed over all possible trap types up to p. The third term S(x,T) stands for the hydrogen source which can be hydrogen implantation. The temporal variation of the concentration of trapped hydrogen is governed by trapping and detrapping from defects. This is described in the following equation:

$$\frac{\partial C_t^i(x,t)}{\partial t} = \alpha^i(T)C_s(x,t)\cdot(\eta_t^i(x,t) - C_t^i(x,t)) - C_t^i(x,t)\beta^i(T) \tag{2.11}$$

$$\text{with } \alpha^i(T) \text{ for trapping into trap } i \text{ (s}^{-1}\text{):} \qquad \alpha^i(T) = \nu_t^i exp\left(\frac{-E_t^i}{k_B T}\right)$$

$$\text{with } \beta^i(T) \text{ for detrapping from trap } i \text{ (s}^{-1}\text{):} \quad \beta^i(T) = \nu_{dt}^i C_t^i(x,t) exp\left(\frac{-E_{dt}^i}{k_B T}\right)$$

In Eq. 2.11 C_t^i(x,t) is the local concentration of trapped hydrogen in trap type i and ν_t^i and ν_{dt}^i are the trapping and detrapping frequencies of trap type i. η_t^i is the concentration of trap type i [46, 94–96].
In this model it is assumed that one trap can hold only one hydrogen atom. However, DFT calculations and experimental results show that one defect can trap several hydrogen atoms with different trap energies [76]. This is described by the fill-level model from K. Schmid et al. [88, 96]. This fill-level dependent model is able to describe the isotope exchange in metals at low temperatures. For experiments using only one hydrogen isotope the classical and fill-level dependent models yield the same results [96]. To solve Eqs. 2.10 and 2.11 boundary conditions have to be chosen. Experiments [81, 95, 97] suggest that the recombination rate at the surface can be assumed as infinitely high which leads to an hydrogen surface concentration equal to zero: C(x=0, t)=0. Unfortunately, analytic solutions can be calculated only for few simple problems. A number of computer programs, like for example TMAP7 [98] TESSIM [99, 100] or MHIMS [101] and others [102, 103], is used to solve the problem numerically.
It was observed that the exposure of tungsten to hydrogen with an energy below the displacement energy can results in the formation of blisters and cracks in tungsten. Whether blisters and cracks occur depends on the material temperature, incident ion energy, flux and fluence. This blister and cracks can enhance the hydrogen retention immensely [91, 104, 105].
As hydrogen gets retained in lattice defects acting for it as trap sites, the hydrogen retention in irradiated tungsten increases with damage level. D retention studies of self-damaged tungsten [106, 107] showed that the D retention at low damage levels increases linearly. At higher damage levels the D retention starts to saturate. At 0.20 - 0.25 dpa (dpa value calculated in the Kinchin Pease mode in SRIM) the D retention in tungsten is saturated and reaches at room temperature a maximum value of about 1.8±0.1 at.% deuterium in tungsten [108].

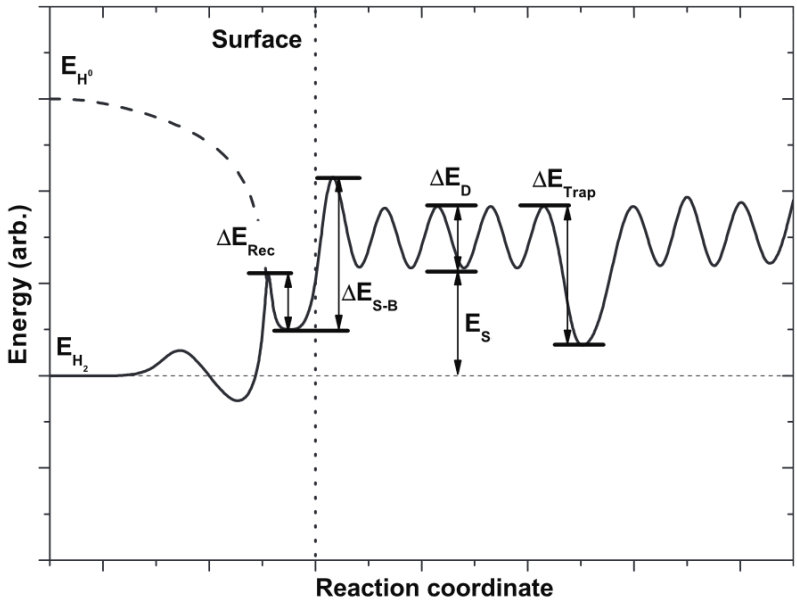

Fig. 2.8: Potential energy landscape for H at the W surface and W bulk. ΔE_{Rec} is the energy needed for recombination of atomic H to H_2 at the surface and vice versa, ΔE_{S-B} is the energy for absorption, ΔE_S the heat of solution, ΔE_D the energy for diffusion, ΔE_{Trap} the detrapping energy [9]. *Republished with permission of IOP Publishing, from "Hydrogen in tungsten as plasma-facing material", J. Roth and K. Schmid, Physica Scripta, volume 2011, 014031 (2011); permission conveyed through Copyright Clearance Center, Inc.*

2.5 Objectives of the present thesis

As tungsten is a promising plasma-facing material, large efforts are made to understand the radiation damage of tungsten induced by neutrons and its influence on hydrogen retention. As described in section 2.2, neutron sources with an energy spectrum characteristic for fusion are not available and different ion species (Sect. 2.3) are used to simulate neutron radiation damage in tungsten. It is not clear to what extent the radiation damage and the subsequent hydrogen retention created by the different ion species is comparable and to what extent it resembles that of neutrons. Only few works exists which deal with the systematic comparison of the response of tungsten to different ion irradiations [68–71]. These works often compare only one aspect like the microstructure or the hydrogen retention. Therefore, the main objectives of the thesis are the following:

- Characterization of the microstructure of the damage zone in tungsten irradiated by different ions.
- Investigation of the D retention in tungsten irradiated by different ions.
- Investigation of the correlation between the microstructure of the damage zone and the D retention.

In order to tackle the above mentioned objectives, tungsten was irradiated by different ion species (H, D, He, Si, Fe, Cu and W) to damage levels of 0.04 dpa and 0.5 dpa at the Max-Planck Institut für Plasmaphysik (IPP). This ion irradiation produced displacement damage in tungsten. In the following work, the expression damage always means displacement damage.
To study the microstructure of the irradiated tungsten, transmission electron microscopy (TEM) at the Warsaw University of Technology (WUT) and positron annihilation lifetime spectroscopy (PALS) at the research neutron source (FRM-II) was used. TEM is a widely used method to investigate dislocations. To investigate the whole damage zone, TEM lamellas were cut out of the tungsten samples perpendicular to the surface with focused ion beam microscopy (FIB). This provided the possibility to investigate the dislocation structure throughout the whole ion damage range. As with TEM vacancies and small vacancy clusters can not be resolved, PALS was used to investigate these kind of defects.
To study the D retention in tungsten the samples were D loaded at the low-flux deuterium plasma device PlaQ at IPP. The plasma conditions during D loading

were chosen such to prevent additional displacement damage during loading. To investigate the D retention behavior in tungsten nuclear reaction analysis (NRA) and thermal desorption spectroscopy (TDS) were performed at IPP. With NRA using the reaction D(^{3}He, p)α D concentration depth profiles were derived. Through TDS the D desorption spectra were obtained.
In the next chapter 3, most of the experimental and analysis techniques are introduced. In chapter 4, the damage calculation with SRIM and the irradiation parameters are described. The following chapters 5 and 6 are presenting the results of this work. In chapter 5, the results about the microstructure obtained by TEM (Sect. 5.1) and PALS (Sect. 5.2) are presented. In the following chapter 6, the results on the D retention in tungsten are described. In chapter 7, a discussion of the results obtained by all three methods is given and a short outlook on possible future research topics.

Chapter 3

Experimental apparatus and analysis

3.1 Sample preparation prior to irradiation

Single crystalline W samples were cut from a high-purity single crystalline tungsten rod (diameter 10 mm). It was grown along the ⟨100⟩ crystallographic direction by electron-beam floating zone melting at the Institute of Solid State Physics in Chernogolovka, Russia [109, 110]. The accuracy of the crystallographic orientation of the rod is ±2°. Samples with a thickness of 1.5 mm were cut by spark erosion from the rod. Before cutting into slices, two sides of the rod were removed resulting in the sample shape shown in Fig. 3.1, with a long edge and a short edge. This shape was chosen in order to have the possibility to orient the crystal with respect to its primitive cell. To remove residue from the spark erosion the samples were mechanically polished with a final grinding step of P4000 SiC paper. After mechanical polishing the samples were cleaned in an ultrasonic bath successively with acetone, isopropanol, high purity acetone and finally followed by rinsing with distilled water. In the next step, the samples were electro-polished with 1.5 % NaOH at 19 V for 3 min to mirror-like finish with the machine LectroPol-5 from Struers. Laue X-ray diffraction was conducted at the Technical University Munich from several polished samples. It was found that the surface normal was within 4° from the ⟨100⟩ direction. The ⟨100⟩ direction in the x, y plane was found to be about 43° ±1° with respect to the long edge of the sample. Prior to the irradiation, the samples were outgassed at 1200 K for 30 min and annealed at 2000 K for 5 min by electron bombardment in an ultra high vacuum ($<10^{-5}$ Pa). Polycrystalline W

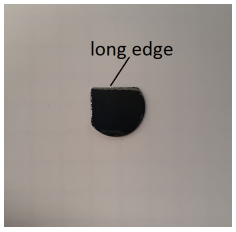

Fig. 3.1: Shape of the single crystalline W samples.

samples of a size of 10 x 10 x 0.7 mm^3 and a purity of 99.97 wt.% manufactured by Plansee SE, Austria were used [111]. All samples were from the same manufacturing batch, i.e. the texture and purity of the samples was comparable. These samples were mechanically polished with a final grinding step of P2500 SiC paper and then cleaned as the single crystalline samples in an ultrasonic bath. In the next step, they were electro polished with 1.5 % NaOH at 19 V for 15 min in a in-house made apparatus to mirror-like finish. After polishing the samples were outgassed at 1200 K in an ultra high vacuum for 30 min. To reduce intrinsic defects and to anneal the distortions introduced by the polishing process, the samples were annealed at 2000 K for 5 min by electron bombardment in an ultra high vacuum ($<10^{-5}$ Pa). After the re-crystallization process, the initial (as delivered) dislocation density is reduced by about two orders of magnitude to $1.9 \pm 1.4 \cdot 10^{12} m^{-2}$ [112].

3.2 Irradiation of the samples at the Tandem accelerator

Irradiations of the samples were performed at the implantation beamline of the 3 MV tandem accelerator of the Max-Planck Institut für Plasmaphysik. For the irradiations the samples were mounted on a water-cooled copper holder to prevent temperature rise of the samples during irradiation, Fig. 3.2. In order to suppress channeling of the incident ions, the single crystalline samples were not mounted directly on the water-cooled sample holder but were tilted in two perpendicular directions. A wedge-shaped top piece was designed to be placed on the sample holder. On top of this wedge, the single crystalline W samples were mounted using a circular molybdenum mask with an opening area of 7 mm in diameter, see Fig. 3.2a. The samples were tilted of about 12° in one direction. Additionally, the sample holder was rotated by 8° to tilt the sample in the second direction. This gives an angle of about 14° between the ion beam direction and the surface normal. This procedure ensured the irradiation of the single crystal in an arbitrary

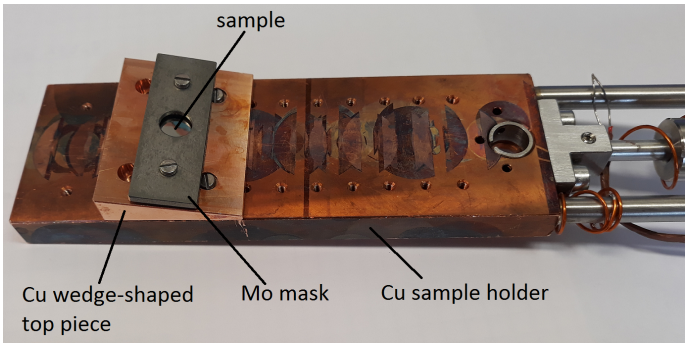

(a) Sample holder used for damaging of single crystalline W samples.

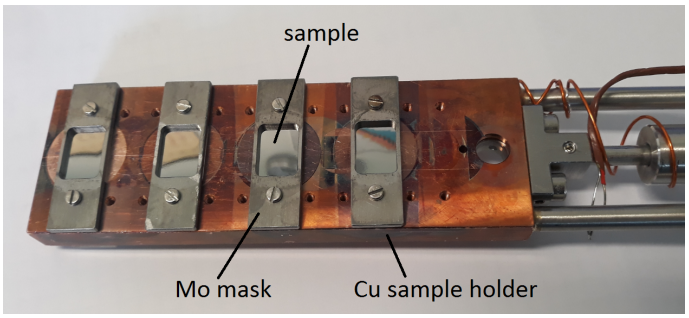

(b) Sample holder used for damaging of polycrystalline W samples.

Fig. 3.2: Sample holders used during sample irradiation with different ions.

crystallographic direction far away from the three main axis ⟨100⟩, ⟨110⟩, ⟨111⟩. Ion beam channeling in axial direction was, therefore, suppressed. The single crystalline samples were always oriented in the same way ±4° (due to the uncertainty of the crystal orientation) to ensure the same crystallographic orientation during irradiation.

The poly-crystalline W samples were fixed directly with a molybdenum mask with an opening area of $9 \cdot 9$ mm^2 to the water-cooled copper holder, compare Fig. 3.2b. To measure the ion current during irradiation a water-cooled aperture with four Faraday cups at the corners is placed in front of the sample holder. In order to damage the whole sample surface homogeneously and to measure the current with the Faraday cups, the ion beam is scanned over the area of the front aperture and the faraday cups. Due to this current measurement the ion flux incident on the sample can be calculated. The W irradiation was found in [113] to be homogeneous within 2%.

3.3 Electron microscopy

During this work mainly six different electron microscopes were used. Due to the different strengths and weaknesses of the different devices, different microscopes had to be used depending on the sample to be observed and the problem to be solved. Five of the used microscopes are operated at the material science department at the Warsaw University of Technology (WUT).
For imaging the surface after irradiation and D loading, two scanning electron microscopes were used: FEI Helios NanoLab 600 at IPP Garching and Hitachi SU 8000 at WUT. Both microscopes are equipped with detectors for secondary electrons and backscattered electrons. The observations at the FEI Helios NanoLab 600 and Hitachi SU 8000 microscopes were conducted at an acceleration voltage of 10 kV. Helios is additionally equipped with an ion beam column, which uses Ga^+ ions up to an energy of 30 keV for cross sectioning allowing in situ cross-sectioning and imaging of the sample. This microscope was used for the investigation whether blisters were formed on the sample surface or just below the sample surface during D loading.
The lamella preparation for TEM observations was made using the focused ion beam microscope FIB FB-2100 Hitachi at WUT which uses Ga^+ ions at an acceleration voltage of 40 keV for cutting.
During the thinning of the FIB lamella with precision electro polishing the surface state and the transparency of the lamellas were monitored using the microscope Hitachi 5500 in WUT. This microscope is a SEM equipped with a STEM detector. The operator can use either the SEM or the STEM modus in one apparatus, thus reducing setup-times. Beside the normal entry for macroscopic samples this microscope has a side-entry for TEM holders, making observations of TEM lamellas very convenient. The observations were conducted at an acceleration voltage of 10-20 kV for the SEM modus and 30 kV in the STEM modus.
During thinning of the TEM lamella with the ion milling machine (Gentle mill 2HI Technoorg LINDA), the lamellas were observed using a STEM Hitachi HD 2700 both at WUT, which uses the same TEM holder as the ion milling machine. This STEM is Cs-corrected and was operated at 200 kV, which allows a nominal resolution down to 0.1 nm. It was also used for further investigations of the radiation-damage zone. It is equipped with various detectors, namely a bright field (BF) detector, a high-angle annular dark field (HAADF) detector (also called Z-contrast) and a secondary electron (SE) detector, providing complementary contrasts.
For the investigation of the dislocation structure of the damage zone mainly the classical TEM Jeol Jem 1200 at WUT was used. A classical TEM in comparison

to a STEM has the strength that it allows easily observations under well defined diffraction conditions. It has also a better diffraction contrast than a STEM. To achieve well defined diffraction conditions a Gatan double tilt holder was used with which the sample can be tilted in both axes by ±20°.

3.4 Sample preparation for TEM

For TEM observations, the samples have to be sufficiently thin to be transparent for electrons. Therefore, sample preparation is challenging. As tungsten is a high Z material, tungsten samples are transparent at thicknesses of about 100 nm and below at an electron energy of 120 keV.
In this work, the radiation-damage zone as a function of depth should be investigated. Hence, a method is needed enabling to take out a thin piece of the material perpendicular to the sample surface. This can be achieved by cutting a lamella with a focused ion beam.
For optimal transparency, the lamella should be very thin (<100 nm). If the lamella gets too thin during the preparation, the lamella will start to bend which results in bend contours (appearing as dark shadows) in the image. This makes the observation more difficult or even impossible. The challenge of lamella preparation is, therefore, to get a lamella as thin as possible and not too much bent. The thickness of tungsten lamellas at which they show a good transparency and are not yet too much bent for observation is 80±10 nm.
The TEM lamellas were prepared in two steps: first a lamella of a thickness of 200-300 nm was prepared using the FIB FB 2100 Hitachi microscope. In a second step, this lamella was thinned by a gentle Ar beam of 0.5-1 keV to the desired thickness of 80±10 nm using the ion mill machine: Gentle Mill (2HI) Technoorg LINDA.
For systematic studies of the dislocation microstructure, it was required to have lamellas with a similar crystallographic orientation. To achieve this, the tungsten single crystal was rotated in the vacuum chamber of the microscope such that the surface of the cut out lamella was normal to the ⟨100⟩ direction within ± 3°. To protect the lamella surface from the ion beam during the cutting process, the desired area was coated with tungsten by ion-driven sputter deposition, Fig. 3.3a. In the next step, the material surrounding this region is removed by ion-beam sputtering, Fig. 3.3b. Only a thin connection between the future lamella and the bulk material is retained, compare Fig. 3.3b. In the next step, the sample is tilted by 60° and the floor of the lamella is cut by the ion beam from the bottom. Then the sample is

tilted back to 0° and a manipulator is inserted into the vacuum chamber, Fig. 3.3c. This manipulator is attached to the lamella by W deposition. Then the bridge to the bulk material is removed by sputtering and the lamella can be lifted out, Fig. 3.3d. At this stage, the lamella is around 1 μm thick. The lamella is then moved to a special grid for TEM lamellas, Fig. 3.3e. After attaching the lamella to the grid by W deposition, the manipulator can be detached by sputtering. The lamella is then thinned gradually using ion beams with gradually lower currents until a thickness of 200-300 nm is reached, Fig. 3.3f.

The described preparation of the lamella with the focused ion beam introduces radiation damage by the beam, called FIB damage. To reduce this FIB damage, the lamella has to be further thinned with a method which does not introduce further radiation damage or at least introduces much less. A promising method was precision electro polishing described in [114]. In this method, the sample is electropolished at about 7 V with an electrolyte solution containing 300 g H_2O, 9 g NaOH and 450 g glycerol. Due to the addition of glycerol the polishing process is slowed down. This method was studied extensively during this thesis. It turned out that the method was not usable for thinning relatively thick lamellas of 200-300 nm, because the lamellas were not uniformly thinned resulting in the appearance of holes in the lamella. Even at the edges of the holes the lamellas were not transparent. This method, therefore, requires much more investigation in order to become practically applicable.

Therefore, it was decided to use gentle ion milling for thinning the lamellas. In this process, the lamella was exposed to the low energetic Ar ion beam of 0.5-1 keV in the Gentle Mill (2HI) Technoorg LINDA for three minutes. After this time the surface quality and transparency of the lamella was checked by the microscope STEM HD using its SE and STEM modus. Depending on its transparency, the lamella was further thinned for another three minutes. This process was repeated several times until the desired transparency, i.e. thickness was reached. In sum, every lamella had to be thinned for around 10-20 min. Nearly every lamella survives this thinning process and can be used for further investigations. Every second lamella is of very good quality. During the gentle milling with low energetic Ar ions, the FIB damage on the lamella surface is reduced. As tungsten is very sensitive to any kind of ion irradiation also an Ar ion beam of only 0.5 keV will introduce itself radiation damage. This damage is very close to surface due to the small Ar energy and is seen as small dislocation loops which do not disturb the observations. Such a prepared lamella is then ready for TEM observations.

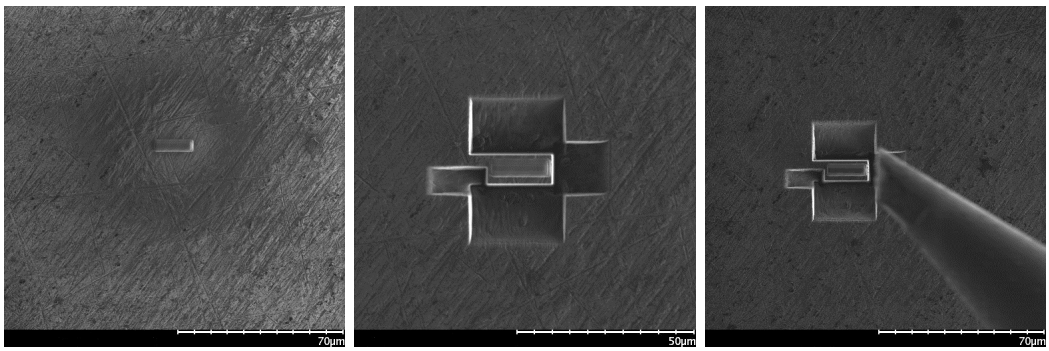

(a) W depostion to protect the lamella surface

(b) Sputtering of the material surounding the lamella

(c) Insertion of a manipulator

(d) Lifting out of the lamella using the manipulator

(e) Placing the lamella on the TEM grid

(f) Further thinning of the lamella to the desired thickness

Fig. 3.3: Steps in the preparation of a TEM lamella with a FIB microscope [115].

3.5 TEM and TEM observation

In a TEM a parallel electron beam is transmitted through the sample to form the image. The sample has to be very thin to be transparent for the electrons. The image arises due to the interaction of the electrons with the specimen. It is then magnified and focused on a fluorescent screen or a CCD camera. Fig. 3.4 shows the TEM setup after the electrons passed the specimen [116]. A TEM has two main operation modes: the diffraction mode and the imaging mode. The operator is able to change between the diffraction pattern and the image of the specimen just by changing the strength of the intermediate lens.
The two most important image contrasts in a TEM are the mass thickness contrast and the diffraction contrast. The mass thickness contrast arises between thicker or higher Z parts versus thinner or lower Z regions in the specimen. Electrons are more strongly scattered at high Z materials or thicker regions meaning that less electrons reach the image plane and these regions appear darker in the image. For crystalline specimens the strongest image contrast is due to the diffraction of the electrons at planes which satisfy the Bragg condition, called diffraction contrast.
By using the selective area diffraction (SAD) aperture it is possible to observe the diffraction pattern of a specific region of the sample, called selective-area diffraction. Every diffraction pattern shows a bright central spot which contains the electrons which passed the specimen without diffraction (direct beam) and additional bright spots which contain the electrons diffracted at certain planes (diffracted beams). The image can be formed using either the direct beam, or all, or some of the diffracted electrons. To form an image from the direct beam, the central spot in the diffraction pattern is chosen by inserting the objective aperture and changing the strength of the intermediate lens to get the image. Such an image is called bright field image (BF image). In a BF image all regions which do not diffract the beam appear bright and regions with other crystallographic orientation, dislocations or distortions of the crystal lattice, which diffracted the beam, appear dark. When the diffracted electrons are used to form the image the image is called dark field image [116–118]. The strongest contrast in a BF image is achieved if the sample is tilted such that only two spots are visible in the diffraction pattern, i.e. the direct beam and one diffracted beam. This situation appears when one set of planes (corresponding to the diffraction vector $\mathbf{g}$) satisfies or nearly satisfies the Bragg condition. This two-beam conditions has to be set up carefully by observing the Kikuchi diffraction

pattern [1] and by maximizing the contrast in the BF image [116–118]. The Bragg condition is satisfied when the Kikuchi lines intersect the direct beam spot and the diffracted beam spot, then the deviation parameter **s** [2] is exact zero, Fig. 3.5. Under such conditions the contrast is very sensitive to any kind of deviation from the diffraction condition. This is called dynamical BF image. Dislocations, weak lattice strains, weak distortions of the crystal lattice are well visible. An image with a contrast less sensitive to any kind of strain but more confined to the physical size of the diffracting dislocations is the kinematical BF image. A kinematical BF image is taken under a specific two-beam condition with a **s**-parameter ≥ 0, which means that the Kikuchi lines are shifted from the diffraction spots, see Fig. 3.5. The operator first sets a BF image with **s**=0 and then tilts the specimen slightly away from the Bragg condition by observing either the Kikuchi lines or until the image shows the best contrast between dislocations and background (the contrast due to weak strain fields disappears) [117–119].

When observing dislocations with a TEM under a specific diffraction condition **g**, one has to keep in mind that only dislocations with Burgers vector **b** not perpendicular to **g** are visible. If $\mathbf{b} \circ \mathbf{g} = 0$ is set, the dislocations will disappear [116–118]. It has been observed in [120] that the determined dislocation densities can differ from one diffraction condition to another due to the invisibility criterion. Therefore, defect densities should not be measured based on just one TEM image taken under a specific diffraction condition. They should be determined under several diffraction conditions. When comparing TEM images from different samples it is important to compare always images recorded under the same diffraction condition [120].

Therefore, the damaged tungsten samples were observed under four different diffraction conditions. The Burgers vectors **b** of the dislocations are low indices vectors of type $\langle 111 \rangle$, $\langle 110 \rangle$, $\langle 100 \rangle$ [3] as this dislocation orientations have the lowest formation

1. The Kikuchi diffraction pattern arises from electrons which were incoherently scattered and pass the sample at random directions. A part of these incoherently scattered electrons satisfies the Bragg condition and are diffracted at the crystal planes. This diffraction pattern appears as lines beside the normal diffraction spots. The Kikuchi lines are very sensitive to every kind of tilting the specimen, therefore they are used to orient the crystal properly.
2. The deviation parameter s is a vector in the reciprocal space which is a measure of the deviation from the Bragg condition. s=0 means the Bragg conditions is exactly satisfied.
3. Bracket convention as in [21]: Square brackets [ ] are used for specific directions.
   Angle brackets ⟨ ⟩ denote a group of directions of the same crystallographic type.
   Round brackets ( ) are used for planes and
   curly brackets { } are used for a family of planes of the same type.
   For vector **g** plane brackets are used, as this vector corresponds to the diffraction at the planes respectively.

energy. Experimental observations show that interstitial dislocations have either the Burgers vector $\mathbf{b}=a_0/2\langle 111\rangle$ or $\mathbf{b}=a_0\langle 100\rangle$ with a_0 the lattice constant. Eyre and Bullough [121] expect that interstitial point defects aggregate on the $\{110\}$ plane as a single platelet of $\mathbf{b}=a_0/2\langle 110\rangle$. The dislocation core is a high energy stacking fault and is removed by the following two equations:

$$\frac{a_0}{2}[110] + \frac{a_0}{2}[00\bar{1}] \rightarrow \frac{a_0}{2}[11\bar{1}] \tag{3.1}$$

$$\frac{a_0}{2}[110] + \frac{a_0}{2}[\bar{1}10] \rightarrow a_0[010] \tag{3.2}$$

However, the reaction 3.2 has a very low probability at room temperature. In [122] small loops of $\mathbf{b}=1/2\langle 110\rangle$ up to a size of 0.9-2 nm were observed in tungsten irradiated by 60 keV Au. Therefore, the authors stated that after reaching a critical size the loops shear to remove the stacking fault by Eq. 3.1 [122]. Masters [123] suggests that two mobile loops of $\mathbf{b}=\pm\langle 111\rangle$ can undergo the following reaction:

$$\frac{1}{2}[111] + \frac{1}{2}[\bar{1}\bar{1}1] \rightarrow [001] \tag{3.3}$$

This statement is supported by the results of [120]. MD simulations [33, 34] show that vacancy-type and interstitial type dislocation exists. Dislocations of $\mathbf{b}=\langle 100\rangle$ and $\mathbf{b}=\langle 111\rangle$ were found to be a direct result of the collision cascade suggesting that due to the high energy in the collision cascade the probability of reaction 3.2 increases. Interstitial type and vacancy type loops of Burgers vector $\mathbf{b}=\langle 111\rangle$ and $\mathbf{b}=\langle 100\rangle$ were observed to be present in self-irradiated tungsten [35]. From the above discussion dislocations with a Burgers vector of $\mathbf{b}=\langle 111\rangle$ and $\mathbf{b}=\langle 100\rangle$ can be expected. It is important to choose such diffraction vectors $\mathbf{g}$ which are perpendicular to this kind of Burgers vectors, to investigate which kind of dislocations disappear under which diffraction condition [120]. Fig. 3.6 show the diffraction pattern of the low index zone axes in a bcc crystal [118]. For a quantitative analysis a zone axis should be chosen which contains the desired $\mathbf{g}$ vectors and in which the $\mathbf{g}$ vector can be easily distinguished. Therefore, the zone axis [100] and [110] would be good choices as their diffraction patterns are not fully symmetric (Fig. 3.6 a and b). The [111]-zone (Fig. 3.6 c) axis would be not a good choice as the diffraction pattern is symmetric and it is impossible to index the diffraction spots at different diffraction pattern in the same way, as the diffraction pattern may be rotated.
It was decided to take the [100] zone axis (Fig. 3.6 a).
The lamella was tilted to the zone axis [100]. After obtaining the diffraction pattern of the zone axis [100], the specimen was tilted such to get the different two-beam

conditions with the four diffraction vectors **g**= (-200), (020), (-110), (110). The images were taken at these four diffraction conditions in the kinematical BF mode to get the best possible contrast as described above.
Table 3.1 shows under which diffraction condition **g** which dislocations with Burgers vector **b** vanish. To determine the Burgers vector of a specific dislocation, one should trace the specific dislocation through different diffraction conditions and find the **g** at which the dislocation disappears. However, at high dislocation densities this is impossible. To determine the relative contribution of different Burgers vectors and their densities, the statistical method described in Prokhodtseva et al. [120] may be helpful. In this method, the families within the Burgers vector are treated equally and three independent families with the Burgers vector of type $\langle 100 \rangle$, $\langle 111 \rangle$, $\langle 110 \rangle$ are considered, respectively. As it is known which dislocation orientations are observed, the following equations can be derived for the used diffraction conditions (-200), (020), (-110), (110), see Eq. 3.4. $N_{\mathbf{g}}$ stands for the dislocation density observed under the diffraction vector **g** and $N_{\mathbf{b}}$ is the dislocation density of the Burgers vector **b**.

$$\begin{aligned} N_{\mathbf{g}=(-200)} &= \frac{1}{3}N_{\mathbf{b}=\langle 100 \rangle} + N_{\mathbf{b}=\langle 111 \rangle} + \frac{1}{2}N_{\mathbf{b}=\langle 110 \rangle} \\ N_{\mathbf{g}=(020)} &= \frac{1}{3}N_{\mathbf{b}=\langle 100 \rangle} + N_{\mathbf{b}=\langle 111 \rangle} + N_{\mathbf{b}=\langle 110 \rangle} \\ N_{\mathbf{g}=(-110)} &= \frac{2}{3}N_{\mathbf{b}=\langle 100 \rangle} + \frac{1}{2}N_{\mathbf{b}=\langle 111 \rangle} + \frac{3}{4}N_{\mathbf{b}=\langle 110 \rangle} \\ N_{\mathbf{g}=(110)} &= \frac{2}{3}N_{\mathbf{b}=\langle 100 \rangle} + \frac{1}{2}N_{\mathbf{b}=\langle 111 \rangle} + \frac{3}{4}N_{\mathbf{b}=\langle 110 \rangle} \end{aligned} \tag{3.4}$$

When single dislocations are clearly visible the dislocation density for a known lamella thickness can be determined by two methods. One method is counting the total number of dislocations in a part of the image which gives the number of dislocations in a certain volume ($\frac{1}{m^3}$). The second method, especially useful at higher dislocation densities, is the line intersection method. In the line intersection method arbitrary lines are drawn in the image and the number of intersection of the lines with the dislocations are counted. Having the number of intersections N and knowing the lamella thickness t and the length of the drawn lines l, the dislocation density ρ can be calculated with Eq. 3.5 giving the dislocation density in the units of $\frac{m}{m^3}$ [124, 125].

$$\rho = \frac{N}{l \cdot t} \tag{3.5}$$

Having the dislocation densities under different diffraction conditions, these can be inserted in Eq. 3.4 [120].

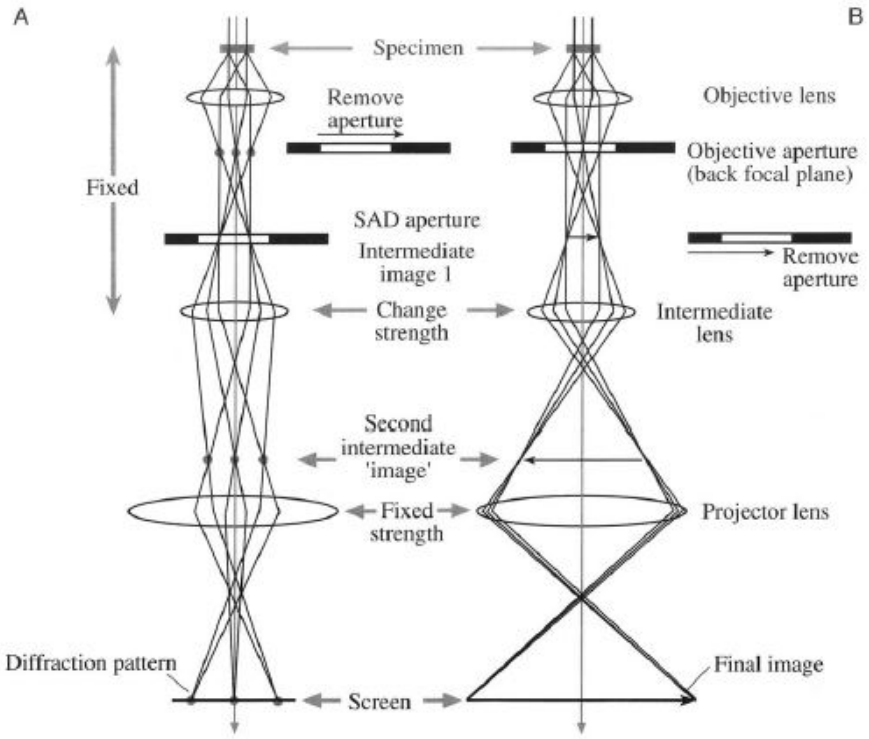

Fig. 3.4: TEM imaging lens setup. Note please that this image shows only the TEM lens setup after the incident electrons passed the specimen. It shows the two main operation modes of a TEM:
A) projection of the diffraction pattern on a viewing screen and B) projection of the image on the viewing screen.
For imaging the diffraction pattern the intermediate lens selects the back focal plane of the objective lens as object to magnify. In imaging mode the strength of the intermediate lens is set such that the image plane of the objective lens (the image) is magnified.
Reprinted by permission from Springer Nature: Springer "Transmission Electron Microscopy Basics I" by David B. Williams, C.Barry Carter, Springer Nature, (1996) [116]

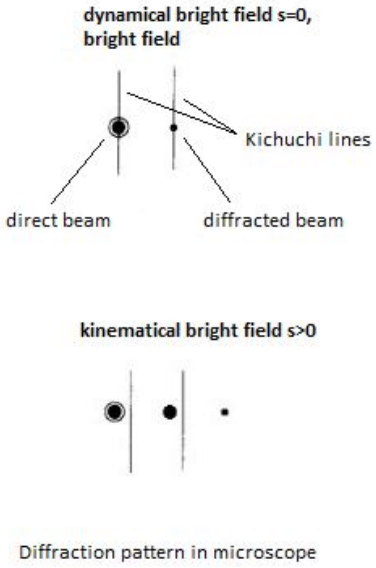

Fig. 3.5: The upper part of the image shows the position of the Kickuchi lines and the diffraction points in a dynamical bright field image. The lower part shows the position of the Kikuchi lines versus the diffraction spots in a kinematical bright field image [119]. *Reprinted from "Characterisation of radiation-damage microstructures by TEM", Journal of Nuclear Materials 216, 124 (1994), M.L. Jenkins, Elsevier (1994), with permission from Elsevier [119].*

g \ **b**	100	010	001	111	-111	1-11	11-1	110	-110	011	01-1
⟨-200⟩	v	i	i	v	v	v	v	v	v	i	i
⟨020⟩	i	v	i	v	v	v	v	v	v	v	v
⟨-110⟩	v	v	i	i	v	v	i	i	v	v	v
⟨110⟩	v	v	i	v	i	i	v	v	i	v	v

Table 3.1: Invisibility criteria for dislocation depending on their Burgers vector **b** and the diffraction condition **g**. visible (v), invisble (i)

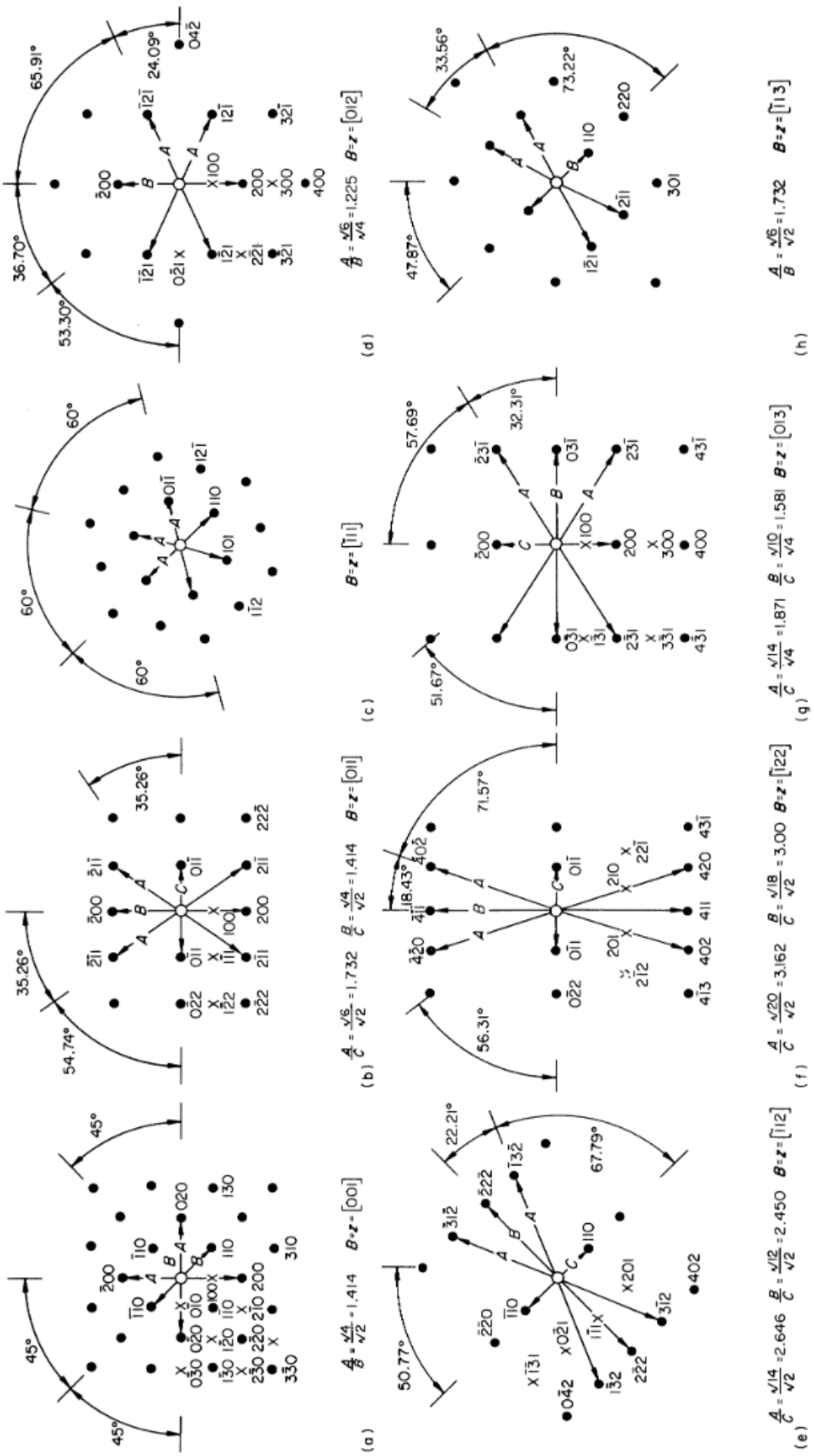

Fig. 3.6: Diffraction patterns of low index zone axis in a bcc crystal [118]. The central spot in each diffraction pattern is the direct beam and the other spots are the diffracted beams at the respective planes. *Reprinted from "Practical Electron Microscopy in Materials Science, Monograph Two Electron Diffraction in the Electron Microscope", J. W. Edington, MACMILLAN Philips Technical Library, 1974, with permission from Springer Nature*

3.6 Positron annihilation lifetime spectroscopy

Positron annihilation lifetime spectroscopy (PALS) is a method to detect open-volume defects like vacancies, vacancy clusters, dislocations and grain boundaries. As a non destructive method it allows repeating measurements to observe the defect evolution after different treatments of the sample [126–128].
Fig. 3.7 shows schematically the principle of the technique.

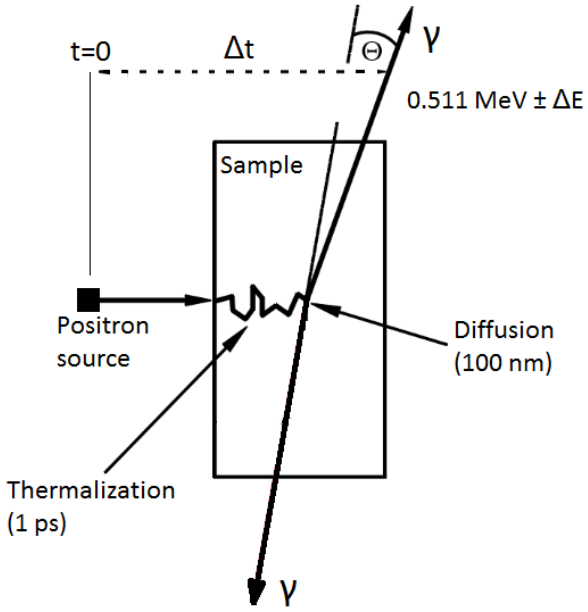

Fig. 3.7: Schematic illustration of positron annihilation. In Positron lifetime spectroscopy the time between the positron implantation and its annihilation in the bulk is measured, as schematically marked by the dashed line. In Doppler broadening spectroscopy the energy and angular deviation of the two γ quanta is measured, giving information about the momenta of the annihilating electrons.

In this technique an energetic positron is injected into the material. Within few picoseconds the positron looses its energy by ionization, excitation of atoms and scattering at phonons until it is thermalized. Then it diffuses through the solid. It can be described as a wave package being delocalized over many elementary cells. A positron experiences a repulsion from the positive atomic nuclei, therefore, every open-volume defect is a minimum in the potential energy landscape for the positron. Hence, the positron can be trapped there. Trapped in a defect it is in a localized state. The positron will finally annihilate with an electron either from the free state in the bulk or from the trapped state in the defect with one of the surrounding

electrons. The electron density in an open volume defect is reduced thus increasing the lifetime of the positron being trapped. In this way, the lifetime of a positron reflects the size of the open volume defects [126, 129]. The positron electron pair turns in most cases into two γ rays which in the center of mass system fly exactly in the opposite direction carrying the energy of 511 keV each. In the lab system, a deviation θ from 180° and an energy shift ΔE is observed due to the momentum of the annihilating electron. In positron lifetime spectroscopy, the time between the injection of the positron and the annihilation of the positron is measured. The number of annihilation events in time is detected, giving the lifetime spectrum Z(t). It can be described by a sum of exponential decays with relative intensities I_i and lifetimes τ_i convoluted with an instrumental time resolution function R(t) and a constant background B.

$$Z(t) = R(t) \otimes \left(\sum_{n=0}^{N} \frac{I_i}{\tau_i} e^{\left(\frac{t}{\tau_i}\right)} \right) + B \tag{3.6}$$

I_i and τ_i are the relative intensities and positron lifetimes from the defect type i and I_0 and τ_0 represent the annihilation from the free bulk state. The sum over the intensities should add to unity: $\sum_{i=0}^{N} I_i = 1$. The average lifetime of a positron in the investigated material is defined as: $\tau_{av} = \sum_{i=0}^{N} I_i \tau_i$ [126]. For PALS measurements typically a Na^{22} β^+ source is used. The positrons emitted by Na^{22} have a broad energy spectrum up to 0.5 MeV. This results in mean positron implantation depths of 10-160 μm depending on the material to be investigated. For studying near surface layers a low energetic positron beam is needed. There are also positron sources which produce positrons by pair production with lower energies [126], resulting in smaller implantation depths. The positron implantation profile $\rho(x, E)$ is described with:

$$\rho(x, E) = \frac{\pi x}{2R_p^2} \cdot \exp\left(-\frac{\pi x^2}{4R_p^2}\right) \tag{3.7}$$

with the mean implantation depth approximated by $R_p = (40/\rho)E^{1.6}$ [nm], E the incident positron energy in keV and ρ [g/cm^3] the density of the material. Fig. 3.8 show the implantation profiles in tungsten obtained from Eq. 3.7.

In this work, PALS was performed at the pulsed low-energy positron beam system (PLEPS). This system is attached to the high-intensity positron beam source NEPOMUC[4] at the research reactor FRM-II in Garching [127, 130, 131]. In NEPOMUC thermal neutrons from the reactor are directed on a 80% enriched ^{113}Cd and based on the nuclear reaction ^{113}Cd(n,γ)^{114}Cd high energetic γ rays are produced. Through a

4. NEPOMUC: NEutron-induced POsitron source MUniCh

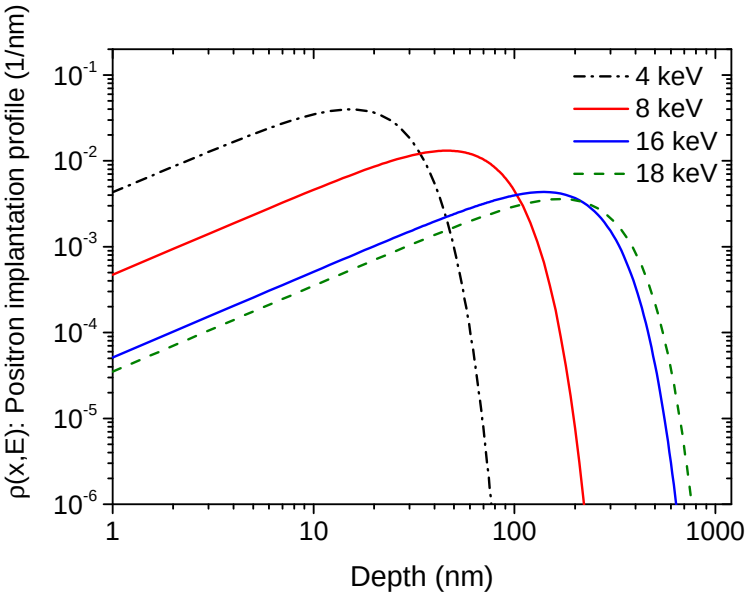

Fig. 3.8: Positron implantation depth calculated with Eq. 3.7 for different positron incident energies. Note the positron implantation profile is normalized to unity.

structure of Pt foils the positron are produced through pair production, i.e. γ rays are converted into positron electron pairs. Pt is also applied as a moderator for the positrons. The primary positron beam is then guided through a magnetic field. To further moderate the beam and to improve the beam brightness the positron beam is directed on a 100 W single crystal resulting in few eV positrons [130]. Such a beam enters the PLEPS system, schematically shown in Fig. 3.9 At the entrance to the PLEPS system, the positrons pass an energy filter to further narrow the energy distribution of the beam. The pulsed positron beam of 150 ps FWHM at a frequency of 50 MHz is produced in the pulsing system consisting of a pre-buncher a chopper and a buncher. The positrons pass through a drift tube to keep the transit time from the exit of the pulsing system to the target constant for all implantation energies. Then they are accelerated to the desired energy between 0.1-18 keV. A Wien filter in front of the target chamber is used to suppress backscattered positrons from the sample. The positron pass then through a field free Faraday cage and are implanted in the sample. The annihilation γ quanta are detected by a photomultiplier with a BaF_2 scintillator located behind the sample. The lifetime spectrum is collected. The time between the annihilation and the following pulse is measured by an external clock [127, 131].

In this work, in order to collect the lifetime spectrum, positron implantation energies of 16-18 keV were used. In each spectrum $4{\cdot}10^6$ events are collected. The count rate is up to 10^4 counts/s. The instrument function is determined with a p-type SiC reference sample with a well known bulk and surface lifetimes.
The lifetime spectra were evaluated using the POSWIN software developed at the Technical University of Denmark. It performs an iterative least square fitting of a model function described by Eq. 3.6. Fig. 3.10 shows as an example a measured lifetime spectrum fitted with four exponential functions, corresponding to four different lifetimes.

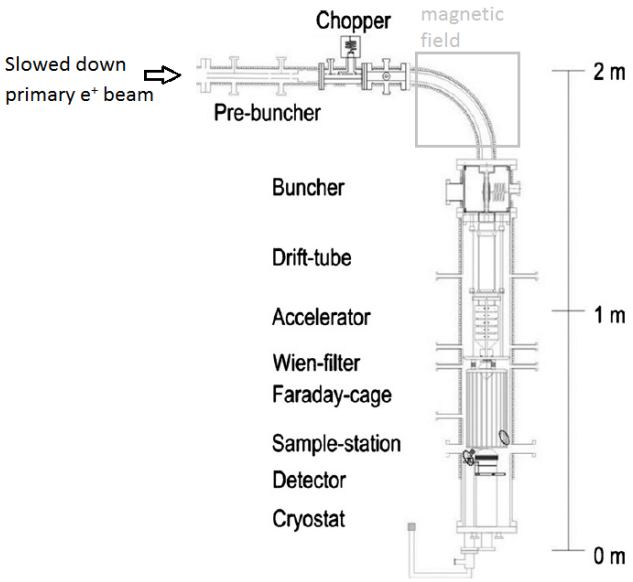

Fig. 3.9: Schematic view of the pulsed low-energy positron beam system PLEPS [131]. *Reprinted from "Status of the pulsed low energy positron beam system (PLEPS) at the Munich Research Reactor FRM-II ", Applied Surface Science 255, p.35 , P. Sperr, Elsevier (2008), with permission from Elsevier*[131]

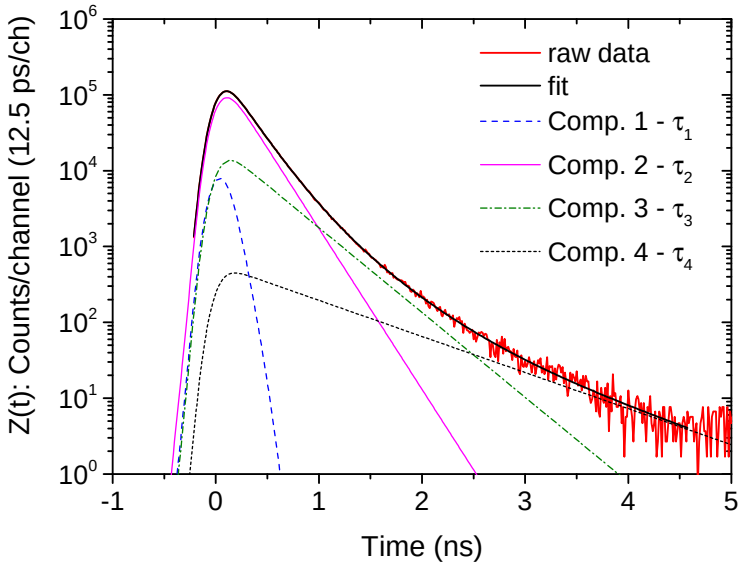

Fig. 3.10: Positron lifetime spectrum fitted with four exponential functions.

3.7 Deuterium plasma exposure - PlaQ

To study the D retention in damaged tungsten, the irradiated samples were D loaded. For this purpose, the samples were exposed to a low temperature D plasma from the electron-cyclotron-resonance (ECR) plasma source PlaQ [132]. Fig 3.11 shows the PlaQ device schematically [132]. The magnetic field of 87.5 mT for the ECR plasma is created by a water-cooled magnetic coil. The magnetic field is chosen such to get the electron cyclotron resonance. The standard conditions for a discharge are a D_2 gas pressure of 1 Pa and a microwave power of about 140 W. The plasma is confined in a steel mesh cage with an aperture at the bottom of the cage. The plasma beam reaches the sample holder through this aperture. A tungsten grid is mounted behind the aperture to shield the samples from the microwave radiation. The base vacuum pressure being in the range of $2{\cdot}10^{-5}$ to $3{\cdot}10^{-5}$ Pa which is achieved by overnight pumping. Prior to each plasma exposure, the plasma beam is blocked by a shutter not to reach the samples for the first 30 min-60 min. This is done in order to reach stable plasma conditions and to remove impurities of the plasma exposed surfaces. Up to 8 samples can be mounted on the target holder for simultaneous deuterium loading. Electrically conductive samples like tungsten can be biased up to $U_{Bias} = -600\,V$ through the sample holder with a DC power supply for varying the D impinging energy. Under standard operating conditions the ion flux was quantified in [132] and consists of 94% D_3^+ ions, 3% D_2^+ and 3% D^+. The total ion flux is between 10^{19} and 10^{20} D/m^{2}s and is assumed to be constant when using the same experimental conditions. The mean ion energy taking into account the plasma potential of -15 V and the negative bias set on the sample holder U_{Bias} gives an average ion energy of E=eU_{Bias}+15 eV. The mean energy per deuteron of the dominant ion species D_3^+ is, hence, one third of the average ion energy. The sample holder temperature and, hence, the sample temperature is stabilized with an open circuit thermostat filled with silicon oil [132].

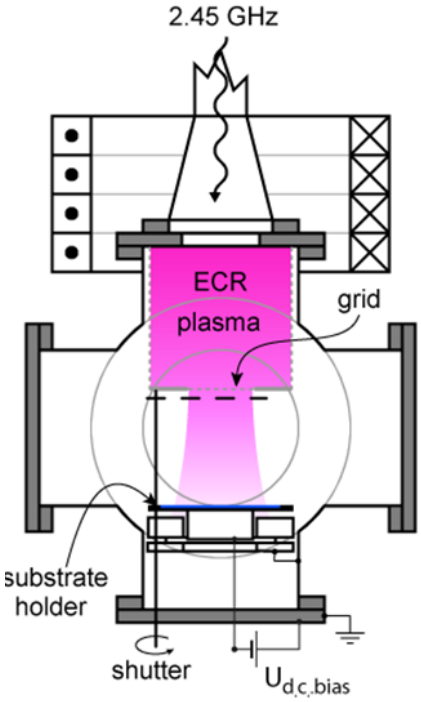

Fig. 3.11: Schematic overview of the electron-cyclotron-resonance plasma source PlaQ [132]. *Republished with permission of IOP Publishing, from "Quantification of the deuterium ion fluxes from a plasma source", A.Manhard et al., Plasma Sources Science and Technology 20, 015010 (2011) ; permission conveyed through Copyright Clearance Center, Inc.*[132]

All samples damaged to the same dpa value were exposed to the deuterium plasma simultaneously. The D exposure time for the 0.5 dpa samples was 86 h and 48 h for the 0.04 dpa samples. These exposure times were chosen based on preparatory measurements ensuring the whole damage zone to be D loaded. The temperature of the samples during implantation was kept at 370 K with a bias voltage of -10 V bias during loading. These conditions result in a mean energy of 8 eV/D and a D flux of 7.2 $\cdot 10^{19}$ $\frac{D}{m^2 s}$ and were chosen such to prevent additional displacement damage during the loading and to prevent blistering. As blisters can considerably enhance D retention [133] the surfaces of the loaded samples were checked by the scanning electron microscope FEI Helios NanoLab 600 at IPP Garching.
At selected places of the samples focused ion beam cross sectioning was conducted to check whether blisters occur in the near surface layers. No blisters at all were found on the samples.

3.8 Nuclear reaction analysis

Nuclear Reaction Analysis (NRA) is an important method for composition analysis, especially of light elements in heavier materials. In this method, an ion beam is directed on a sample containing the light element to be analyzed. The beam ions can undergo a nuclear reaction with the target atoms. Detecting the reaction products provides information about the amount and depth profile of the element under consideration.
The nuclear reaction D(^{3}He,p)α is commonly used to detect deuterium in solids [134], [135]. By the analysis of the α energy spectra and proton energy spectra, depth profiles of D can be derived. This nuclear reaction is the most suitable reaction for deuterium depth profiling due to its high Q-value of 18.4 MeV. Using incident energies of 0.5–4.5 MeV results in high energetic protons of 12.0–13.5 MeV (at the proton detector position at 135°) and α's of 1.2–3.1 MeV (at the α detector position at 102°). These high energies are advantageous as the backscattered ^{3}He particles can be easily stopped by a foil installed in front of the detector. Hence, the signal of the high-energetic protons is usually background free [134]. The total cross section of this reaction has a broad maximum around 630 keV with a maximum total cross-section of about 850 mb: This relatively high cross-section allows high detection sensitivity and a low detection limit below 100 ppm. Differential cross sections for various reaction angles have been measured by a number of authors [135–137]. The maximum analysis depth in tungsten is about 7.4 μm for 4.5 MeV ^{3}He ions due to the high stopping power of tungsten. To be able to derive depth profiles with reasonable depth resolutions several incident ^{3}He energies have to be used. The depth resolutions obtained by this method vary from 100 nm for the near surface layers to 1-2 μm for large depths [134].

Nuclear reaction analysis (NRA) with D(^{3}He,p)α was performed to obtain the D depth profiles and the D amount in the damaged samples. Seven different energies of the ^{3}He beam between 500 keV and 4500 keV were used to get D depth profiles up to a depth of 7.4 μm. The measured proton and α spectra were utilized. The proton spectra were collected by two semiconductor detectors. The first proton detector has a depletion depth of 2000 μm and a solid angle of 30.26 $\pm$ 1.18 msr and is located at the reaction angle of 135°. The second proton detector has a larger solid angle and will be called large proton detector. It has a depletion depth of 3500 μm and a solid angle of 77.5$\pm$3.0 msr. It is located also at 135°. In front of the proton detectors, a foil is installed to prevent backscattered ^{3}He ions from reaching the detectors. In front of the first proton detector, a foil consisting of a 5 μm thick Ni layer and a

12 μm thick Mylar foil coated with 10 nm Au is positioned. The Ni foil faces the target. In front of the large proton detector, a foil consisting of a 50 nm Au layer and 50 μm Mylar is installed. The alpha spectra are collected by a semiconductor detector with a depletion depth of 700 μm installed at 102° and a solid angle of 7.65±0.26 msr. A 3.5 μm Mylar C foil is installed in front of the detector to block the backscattered ^{3}He ions.

The detected energy spectra are a convolution of the deuterium depth distribution, the energy dependent differential cross sections, the stopping powers in the elements and the experimental conditions such as solid angle of the detector and number of incident ^{3}He ions. The determination of the deuterium depth profiles requires a simultaneous fitting of the simulated spectra by SIMNRA [138] to the measured α and proton spectra and deconvoluting them by the program NRADC as described in [139] using SIMNRA 7.01 as simulation kernel [138]. Additionally, at each energy a deuterated carbon thin film (a-C:D) sample was measured for energy calibration. Cross section data from [136] were used. Given the energy spectra, NRADC applies Bayesian statistics to find the most probable deuterium depth profile with the least amount of free parameters. The program first finds an optimum numbers of layers and then conducts a Markov Chain to find the best depth sampling and concentration describing the data. The maximum likelihood approach is applied to the fitting of the experimental data and the determination of the confidence interval. This procedure gives then the most probable D depth profile. The user can define a minimum depth resolution within the Markov chain sampling in the program. If the program calculates a layer thickness below this depth resolution, this solution will be rejected. To calculate the minimum depth resolution at a given depth ResolNRA was used [140].

The resulting D concentration depth profiles are step profiles. The step widths are due to the limited depth resolution of the nuclear reaction analysis method [134]. The steps are showing the average D concentration in a given depth interval. In a recent upgrade of NRADC a new method for representing the statistical uncertainty accumulated during the final MCMC optimization was introduced. The detailed description can be found in [141, 142]. The D depth profiles are shown with their 3σ uncertainty determined by NRADC in Fig. 3.13.

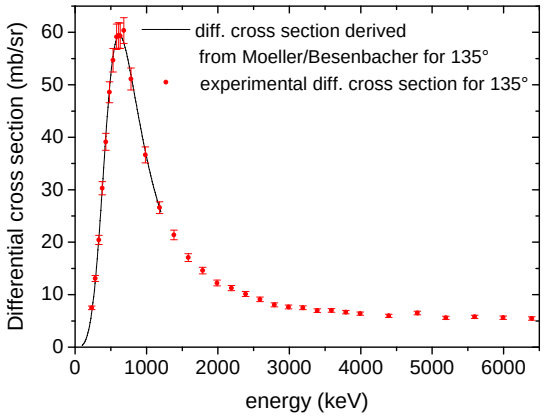

Fig. 3.12: Differential cross section of the D(^{3}He,p)α nuclear reaction for a laboratory angle of 135° experimentally determined by Wielunska et al. [136]. The solid line represents the Möller, Besenbacher differential cross section determined for 135° [143].

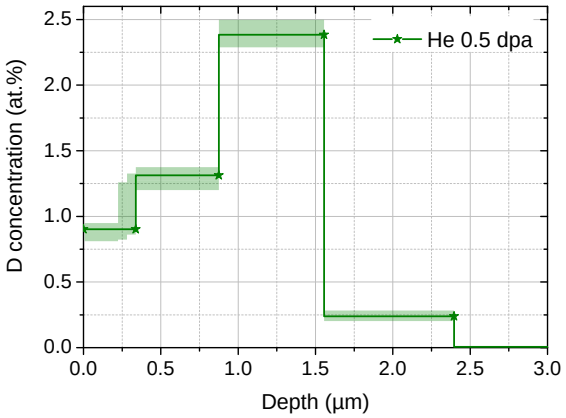

Fig. 3.13: Typical D concentration depth profile obtained by NRADC for tungsten irradiated by He up to 0.5 dpa. The steps in the depth profiles are due to the limited depth resolution of NRA. The steps show the average D concentration for a given depth interval with a 3σ uncertainty in light green.

3.9 Thermal desorption spectroscopy

Thermal desorption spectroscopy (TDS) is a method which allows to study the behavior of gaseous constituents in solids. One drawback of NRA in investigating the D inventory is its limited depth range. 4.5 MeV ^{3}He can reach a depth of only 7.0 μm in tungsten. TDS is able to provide information about the D inventory of the whole sample and gives information about the desorption mechanism and the binding energies. To perform TDS, a D containing sample has to be heated in ultrahigh vacuum. With increasing temperature, the probability increases that a D atom trapped in a defect receives enough energy to escape the trap. When being detrapped the D atom diffuses through the lattice reaching either the surface or being trapped again. When reaching the surface the D atom recombines and desorbs into the vacuum. The desorbed gases are detected by a mass spectrometer. The pressure in the vacuum chamber is defined by the flux of the desorbing particles, the pumping rate and the leak rate. The leak rate and the pumping rate is assumed to be constant in time ensuring a constant background signal. The TDS vacuum system and the heating rate of the sample are chosen such that the increase of the pressure is small. In this case, the desorption flux is proportional to the pressure rise. To quantify the desorbed amount of D, a calibration is conducted using a calibrated leak.

Fig. 3.14 shows schematically the TESS installation at IPP which was used to carry out the TDS measurements in this work. In the TESS setup, the main vacuum chamber is connected to a quartz tube in which the samples are inserted. The background pressure is about 10^{-6} Pa after pumping for a few days. The quartz tube has a side arm allowing the storage of several samples to avoid breaking the vacuum during sample change. Prior to the measurement, the section of the glass tube which is heated during the TDS measurement is annealed at 1300 K to reduce the background signal from particles adsorbed at the glass surface. For the TDS measurement, the sample is brought via a piece of nickel (in the tube) and a magnet (outside the tube) to the measurement position. The other samples are located in the side arm. To heat the sample an external tubular oven is moved over the measurement position. The side arm is far away from the heated area and is cooled via a compressed air flow to avoid temperature rise of the samples stored there. The samples were heated in the quartz tube of the TESS experiment [144] with a linear oven temperature ramp of 3 K/min from 300 K to 910 K. During the heating ramp the desorbed gases were analyzed by a quadrupole mass spectrometer [144].

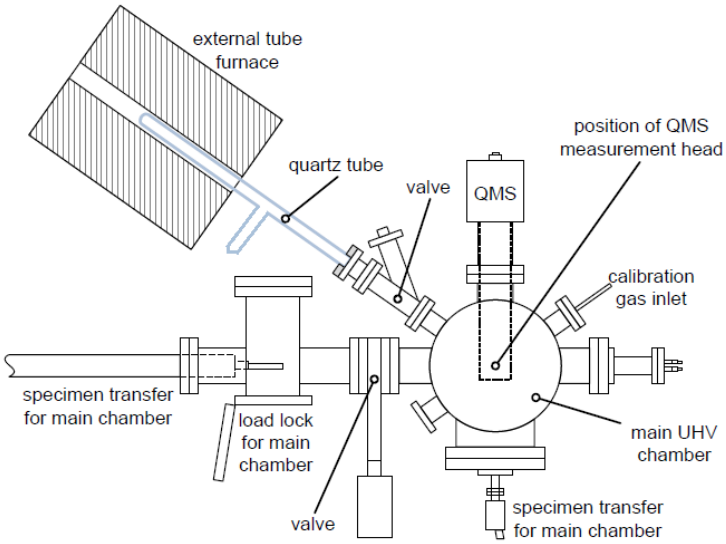

Fig. 3.14: Schematic overview of the TESS setup used for the TDS measurements. *Reprinted from "Redeposition of amorphous hydrogenated carbon films during thermal decomposition", Journal of Nuclear Materials 376, 160, E. Salancon et al., Elsevier (2008), with permission from Elsevier*[144]

The signals of mass channels 1, 2, 3, 4, 14, 16, 17, 18, 19, 20, 27, 28, 29, 32, 44 were recorded. As only the oven temperature is measured during the measurement and not the real sample temperature, a temperature calibration was executed after the measurement. For this, a thermocouple wire of type K was spot welded to a W sample of identical size and the sample temperature was recorded during the ramp. In this way, the measured oven temperature could be linked to the actual temperature of the sample.

Deuterium desorbs mainly as D_2 (mass 4) and HD (mass 3) with a small contribution of HDO (mass 19) and D_2O (mass 20). After each measurement a D_2 gas flow calibration was performed using a calibrated leak to link the measured intensity to the actual deuterium flow. The deuterium desorption flux was determined by summing up the D amount from mass channels 3 and 4, after background subtraction. The amount of D desorbed in form of HDO and D_2O was negligible for all investigated samples.

Chapter 4

Damage Calculation

In this work, the displacement damage and subsequent D retention in tungsten irradiated by different ions (H, D, He, Si, Fe, Cu, W) should be studied. To conduct a comparison of D retention in tungsten irradiated by different ions, a comparable thickness of the radiation damage zone, where the deuterium gets trapped, is favorable. Therefore, the incident ion energies were chosen such that they always produce a damage zone of about 2 μm with a damage peak at around 1.5 μm. The incident ion energies and irradiation fluences were chosen based on displacement damage calculations by SRIM 2008.04 [145]. SRIM is a program to calculate the energetic ion-solid interactions. SRIM uses the Monte Carlo approach in the binary collision approximation (BCA). In BCA the collisions between the incoming ion and the atoms in the material are treated as independent sequences of binary collisions with straight ion trajectories between the collisions. The ions are assumed to experience only electronic stopping. The material structure is assumed to be amorphous, therefore, crystallographic effects like for example ion channeling are not taken into account. BCA simulations are much faster than MD simulations due to the neglect of the many-body interaction. Therefore, they are only valid for ion energies above several tens of eV. The resulting different incident energies are listed in Tab. 4.1. The incident energies cover a wide energy interval from 0.35 MeV for H to 20 MeV for W irradiation. In order to characterize radiation damage, the displacement per atom (dpa) concept was used [29, 146] which was introduced in Sect. 2.1. For the dpa calculations SRIM was run for the different ion species at the given incident energies (Tab. 4.1), using the damage calculation mode "Ion Distribution and Quick Calculation of Damage", calculating 10^6 incident ions for each ion species. In this program mode, the recoil/damage calculation uses the Kinchin-Pease model. A tungsten displacement threshold energy of 90 eV was used

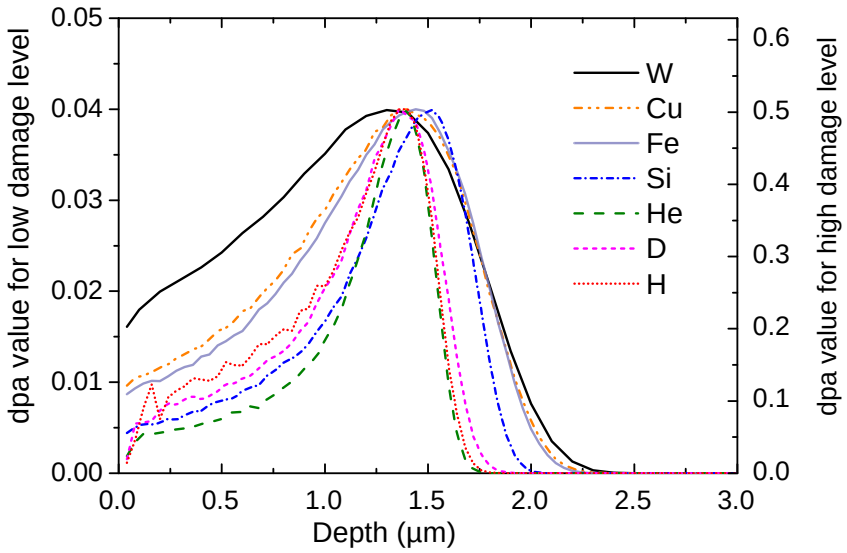

Fig. 4.1: Calculated damage depth profiles in tungsten damaged by W, Cu, Si, Fe, He, D, H ions. Left y-axis: dpa value for damaging up to 0.04 dpa in damage peak maximum; right y-axis: dpa value for damaging up to 0.5 dpa in damage peak maximum.

and the lattice binding energy was set to zero as recommended in [25]. The file vacancy.txt gives the calculated number of vacancies produced by the incident ions and the recoils [145].
Taking this, the dpa value for a given irradiation fluence and vice versa was calculated with Eq. 4.1.

$$dpa = \frac{sum\,of\,vacancies}{material\,density} \cdot fluence \tag{4.1}$$

This method of dpa calculation gives values comparable to the calculation method recommended by Stoller et al. [147]. All used dpa values, in this work, are calculated in this way. Other works such as [15] or [16] used SRIM in the program mode "Detailed Calculation with full Damage Cascades" with a threshold energy of 90 eV giving around twice as large dpa values compared to the here used dpa values [147]. The damage depth profiles as calculated by SRIM for the different irradiations are shown in Fig. 4.1. The damage profiles have a damage peak at around 1.5 μm, as only one incident energy was used. The irradiation fluences given in Tab 4.1 were calculated with Eq. 4.1 such that the values of 0.04 dpa and 0.5 dpa are reached at the damage peak maximum. The different damage levels were chosen based on experiences from other studies. The D retention as function of the damage level was studied in [15]: D retention in self-damaged tungsten shows a linear increase at

small dpa values and saturated above 0.2 dpa meaning that additional irradiation of the sample, i.e. higher dpa values do not increase the D retention further [106, 107]. Note please that in [106, 107] the damage level was calculated in SRIM with full cascade mode. The saturation level was found there at about 0.5 dpa corresponds to a damage level of 0.23 dpa calculated in the way as described above. Therefore, one part of the tungsten samples was damaged to the low dpa value of 0.04 dpa representing the linear regime, in which D retention is proportional to the amount of damage. The other part was damaged to the high dpa value of 0.5 dpa to represent the saturation regime. The damage level is accurate within 10%. In the 0.5 dpa damage level, this uncertainty should not make a large difference as the D retention is in any case in the saturation regime at 0.5 dpa. For the 0.04 dpa damage level this uncertainty could affect slightly the D retention behavior.

In the following work, the different tungsten samples will be named after the ion they were irradiated with and the damage level in the peak maximum. For example, the tungsten sample damaged by Cu up to 0.5 dpa is called Cu 0.5 dpa sample. For the ion species H, D, He, the expression light ions is used. Si is described as medium mass ion. The ion species Fe, Cu, W are called high mass or heavy ions. The expression "damage" is used to describe "displacement damage". After D loading in a low-temperature D plasma, the D retention in these samples was investigated using nuclear reaction analysis ($D(^3He, p)\alpha$) and thermal desorption spectroscopy as described in Ch. 3.7–3.9.

In Tab. 4.1, all ion species and their incident energies and fluences are listed. The amount of backscattered ions is in all irradiations <1% and hence negligible. That in turn means that all incident ions for damaging are implanted into the samples. Using different energies for obtaining a similar damage range unavoidably results in different recoil energy spectra because of the various incident ion energies and because of the different energy transfer due to the varying ion masses. The recoil spectra, shown in Fig. 4.2, were calculated by A. Sand from the University of Helsinki using MDRANGE [148]. It is a molecular dynamics (MD) based code to simulate energetic ions in crystalline material. In MDRANGE, the interaction of the ion with atoms in the target material is described by the universal ZBL repulsive potential [149]. The ion trajectory is calculated by integration of the equations of motion. Interactions between target atoms are neglected. This provides a high computational efficiency with the accuracy of full MD for calculations of energetic projectiles. Electronic stopping data of the projectile in the material is taken from SRIM and is added as a friction force. For the high mass ions Fe, Cu and W, 10 000 ion trajectories were calculated, while for the medium mass to light ions Si, He,

ion	incident energy (MeV)	max. energy of recoils (MeV)	fluence in ion/cm^2 corresponding to 0.04 dpa	fluence in ion/cm^2 corresponding to 0.5 dpa
W	20.3	20.3	$1.36\cdot 10^{13}$	$1.71\cdot 10^{14}$
Cu	9	6.9	$4.44\cdot 10^{13}$	$5.55\cdot 10^{14}$
Fe	9	6.4	$5.23\cdot 10^{13}$	$6.54\cdot 10^{14}$
Si	7.5	3.5	$1.34\cdot 10^{14}$	$1.68\cdot 10^{15}$
He	1	0.083	$5.00\cdot 10^{15}$	$6.25\cdot 10^{16}$
D	0.35	0.015	$2.72\cdot 10^{16}$	
H	0.35	0.0076	$7.96\cdot 10^{16}$	
n	14	0.3045		

Table 4.1: Irradiation parameters used in the presented experiments. Comparison with 14 MeV neutrons is shown in the last row.

D and H, which cause fewer energetic recoils and, hence, require more statistics, 100 000 trajectories were calculated. The obtained energy distributions of recoils were then scaled to the respective ion fluences used in this work for the 0.04 dpa samples (see column 3 in Tab. 4.1). The distribution is given for the total number of recoils per square cm through the whole implantation depth. Fig. 4.2 shows the calculated primary recoil energy spectra in tungsten irradiated by the here used ions. Additionally shown is the primary recoil spectrum in tungsten under DEMO first-wall neutron irradiation as calculated by Gilbert et al. [150]. The vertical lines mark the energy intervall between 42 eV and 90 eV. 42 eV is the experimentally determined lowest displacement energy in tungsten in the crystallographic direction $\langle 100 \rangle$ [24] and 90 eV is the displacement energy in tungsten recommended for use by ASTM [25]. Hence, for recoils with energies below this marked energy interval, no further damage production is expected. From Fig. 4.2, it can be seen that the primary recoil energy spectrum resulting from the irradiation with low mass ions (H, D, He) shows a strong decrease up to the highest possible recoil energy for the specific ion. A large fraction of these primary recoils has only a low energy and is, therefore, not able to produce further damage (energy range below the two vertical line in Fig. 4.2. The irradiation with medium to high mass ions (Si, Fe, Cu, W) leads to primary recoil distributions which decreases not as steeply as for the light ions and extends to much higher maximal recoil energies. The primary recoil distribution for neutron irradiation under DEMO first-wall conditions is relatively flat over a large energy interval. The maximal recoil energy for the here applied ion irradiation conditions

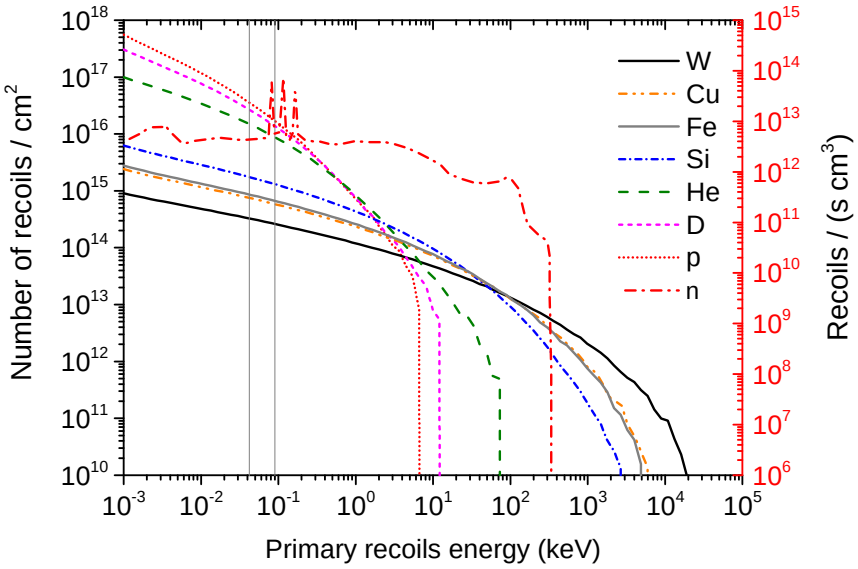

Fig. 4.2: Primary recoil energy spectra for the 0.04 dpa irradiation for the different ions calculated by MDRANGE as described in the text. Additionally the primary recoil spectrum in tungsten calculated by Gilbert et al. [150] under DEMO hcpb (helium-cooled pebble-bed) first wall neutron irradiation is shown. Note please the different units of it on the right y-axis. The vertical lines mark the displacement energy of 42 eV and 90 eV in tungsten.

is listed in Tab. 4.1. These maximal recoil energies span a very wide range. While a 0.35 MeV proton can at most transfer 7.2 keV to a W atom, a 7.5 MeV Si produces recoils up to 3.5 MeV and 20 MeV W up to 20 MeV. The maximal recoil energy for 14 MeV neutrons is about 300 keV and lies in the middle of the range covered here. Hence, the effect of the primary recoil energy on damage creation and deuterium uptake in tungsten can be studied.

A second quantity which varies when using different ions is the ion dependent damage efficieny and the resulting damage rate. Different ions have a different damage efficiency, i.e. produce a different amount of displacement. Tab. 4.2 shows the calculated number of vacancies per incident ion. It can be seen that for medium to high mass ions (Si, Fe, Cu, W) most of the radiation damage is produced by the recoils and not by the incident ion itself. This situation is different for light ions (H, D, He), there the radiation damage originating from the incident ions is of the same order or even higher than the radiation damage due to the recoils. Due to technical limitations, the ion current during the irradiations is also different depending on the ion species used. Due to the ion-dependent damage efficiency different irradiation fluences are needed to obtain the same dpa value in the damage peak. Therefore,

ion	vacancies produced by ions	vacancies produced by recoils	vacancies in total	damage rate in $\frac{dpa}{s}$
W	0.036	1.82	1.86	$4.4{\cdot}10^{-5}$
Cu	0.029	0.54	0.57	$2.2{\cdot}10^{-4}$
Fe	0.028	0.46	0.48	$1.3{\cdot}10^{-4}$
Si	0.023	0.17	0.19	$6.7{\cdot}10^{-5}$
He	0.0031	0.0020	0.0051	$2.8{\cdot}10^{-6}$
D	$7.12{\cdot}\ 10^{-4}$	$2.21{\cdot}\ 10^{-4}$	$9.33{\cdot}\ 10^{-4}$	$1.1{\cdot}10^{-6}$
H	$2.74{\cdot}\ 10^{-4}$	$4.4{\cdot}\ 10^{-5}$	$3.18{\cdot}\ 10^{-4}$	$6.7{\cdot}10^{-7}$

Table 4.2: Vacancies produced in tungsten per incident ion in the damage peak maximum. The last column shows the obtained damage rate ($\frac{dpa}{s}$) for the different ions in the damage peak maximum.

not only the recoil energy spectra differ but also the damage rates (dpa/sec.). The resulting damage rates in the damage peak maximum are also listed in Tab. 4.2. Schwarz-Selinger [113] showed for self-damaged tungsten, at comparable damaging parameters as used in this work, that different damage rates do not influence the D retention in tungsten. Hence, the assumption is justified that for the experiments reported here, the D retention is independent of damage rate.

In order to minimize chemical effects of the implanted ions their concentrations should be low. Fig. 4.3 shows the resulting maximum atomic percentages as a function of depth as calculated by SRIM [145]. The atomic percentage of the implanted ions ranges from 3 to 51 ppm in the damage peak maximum in the samples W 0.5 dpa, Cu 0.5 dpa, Fe 0.5 dpa and Si 0.5 dpa. In the samples irradiated with W, Si, Fe, Cu, Si up to 0.04 dpa, the implanted ion amount is more than ten times smaller. It is assumed that such small impurity concentrations do not significantly influence the displacement damage and the D retention behavior in tungsten, however, this can not be completely excluded. In contrast, the irradiations with H, D, He result in concentrations of the order of 0.5-4 at.% in the maximum. It was reported that He bubbles were observed at a fluence of $5.0{\cdot}10^{16}\ \frac{at}{cm^2}$ at room temperature [151]. Therefore, the formation of He bubbles has to be expected especially in the tungsten samples irradiated by helium up to 0.5 dpa since in that case the used fluence was $6.2{\cdot}10^{16}\ \frac{at}{cm^2}$. Also for hydrogen isotopes bubble formation has to be taken into account. A threshold for blistering of tungsten implanted by keV H or D was reported to be between 10^{18}-$10^{20}\ \frac{at}{cm^2}$. It can be assumed that the blistering mechanism is strongly correlated with a preceding H bubble formation

[152–154]. The here used energies in H and D irradiations were in the keV energy range. The fluences for H and D were 0.8 and $0.3{\cdot}10^{17}$ $\frac{at}{cm^2}$ were below the reported values. Although the H bubble formation cannot be completely ruled out for the H 0.04 dpa and D 0.04 dpa samples its possible influence on the here shown results is expected to be not significant.

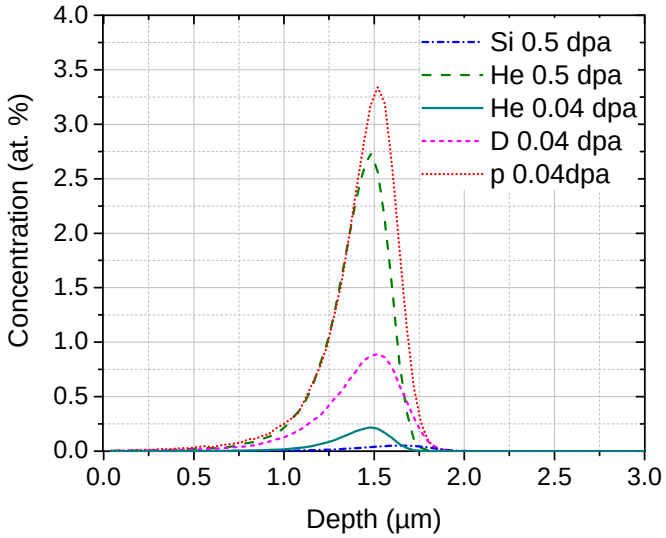

(a) Implanted ion depth distribution in linear scale.

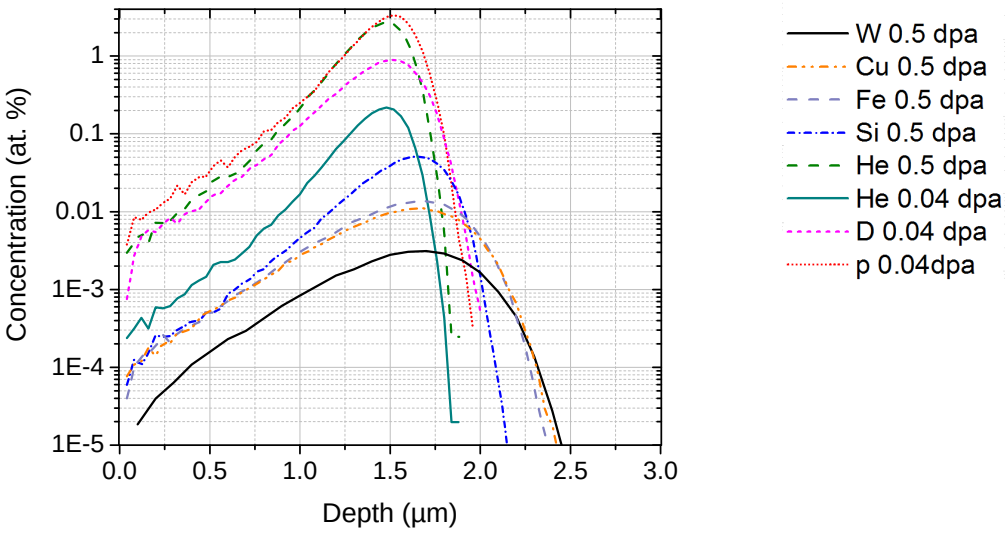

(b) Implanted ion depth distribution y axis in logarithmic scale.

Fig. 4.3: Implanted ion depth distributions for the samples Si 0.5 dpa, He 0.5 dpa, He 0.04 dpa, D 0.04 dpa and H 0.04 dpa as calculated by SRIM. The implanted ion concentration in the samples irradiated by W 0.5 dpa, Cu 0.5 dpa, Fe 0.5 dpa are of the order of 3-51 ppm and hence not visible in the upper image.

Chapter 5

Characterization of the microstructure

In this chapter, the results of the investigation of the microstructure of tungsten irradiated by different ions with transmission electron microscopy (TEM) and positron annihilation lifetime spectroscopy (PALS) are presented. For the TEM investigations, single crystalline tungsten samples were prepared as described in Sect. 3.1 and irradiated as described in Sect. 3.2. The irradiation parameters are given in Ch. 4. After the irradiations thin lamellas were cut from the samples perpendicular to the sample surface as described in Sect. 3.4. The microscopes and methods used in this study are described in Sect. 3.3 and 3.5.
The open volume defect structure was investigated by PALS. For this study polycrystalline tungsten samples were used. The samples were prepared and irradiated as described in Sect. 3.1 and 3.2. The method used is introduced in Sect. 3.6.

5.1 TEM of W irradiated by different ions

The dislocation structure of tungsten samples damaged by H, D, He, Si, W were investigated by transmission electron microscopy and partly by scanning transmission electron microscopy. Tungsten was damaged by He, Si, W to a damage level of 0.04 dpa and 0.5 dpa. H and D damaged samples were only prepared at 0.04 dpa. Preparatory TEM observations of tungsten irradiated by different ions were done on polycrystalline W samples. As described in Sect. 3.5 due to the invisibility criterion, it is important to observe the dislocation structure of the different samples under at least three different two-beam diffraction conditions to be able to compare it. The average diameter of the grains in the used recrystallized polycrystalline W samples is about 20 μm. Therefore, a TEM lamella contained only one or two grains. Sometimes the grains in a lamella were oriented in such a way that even tilting with the double tilt holder in $\pm 20°$ was not enough to obtain the same two-beam diffraction conditions in all observations. Additionally, the images of a lamella which is tilted in the TEM by more than 10° are of lower quality. A second problem is that the dislocation structure obtained by the irradiation may be dependent on the grain orientation during irradiation. Channeling effects may change the local defect density. To compare the dislocation structure one should investigate grains of the same crystallographic orientation during irradiation. This is very difficult to conduct in a polycrystalline material. Therefore, it was decided to use for the TEM analysis single crystalline W samples of the crystallographic direction (100).
In order to characterize damaged tungsten with different ions in a systematic way, a standard observation procedure was defined. Single crystals were always oriented identically during irradiation as described in Sect. 3.2, avoiding channeling in high symmetry axis.
The TEM lamella were prepared by FIB such that the lamella surface normal was directed in the $\langle 100 \rangle$ direction within $\pm 4°$, compare Sect. 3.4. Such a prepared lamella could be easily brought exactly in the [100] zone axis by slightly tilting with the Gatan TEM double tilt holder.
After obtaining the diffraction pattern of the zone axis [100] the specimen was tilted such to get the different two-beam conditions of the four diffraction vectors **g**:
(-200), (020), (-110), (110). The images were taken at these four two-beam diffraction conditions in the kinematical bright field (BF) mode to get the best possible contrast.
This way of observation is very systematic giving the possibility to see how the defect structure changes at different two-beam conditions. It provides the possibility to

determine whether there are Burgers vectors which are more frequent than others. Figs. 5.1a - 5.1d and 5.2a - 5.2d show typical TEM images of self-damaged tungsten up to 0.04 dpa and, respectively, up to 0.5 dpa at the four different two-beam conditions. In all images, the surface of the samples is not shown to avoid overexposure of the camera during recording and to have a good contrast. The surface is parallel to the upper end of the image. To measure the damage range summarized in table 5.1, additional images at lower beam intensity containing the surface were taken.
The damage zone is clearly visible in the upper half of the image as a darker region, exemplary marked in Fig.5.1. The incident ions create radiation damage in form of interstitials, interstitial cluster, vacancies, vacancies cluster and dislocation loops or lines. Interstitials are mobile at room temperature in tungsten and, hence, not present in the damage zone. Dislocation loops and lines can be observed in a TEM image. They appear black in the BF image. Hence, an highly damaged region will appear darker. In the lower half of the image undamaged tungsten is visible. Although tungsten was only irradiated up to a depth of 2 - 2.6 μm it shows a significant amount of small dislocation lines, loops and very small loops appearing as small dots. Fig. 5.3 shows an image of an undamaged tungsten sample for comparison. The same dislocation structure is visible as in the lower part of the images of irradiated tungsten. These visible dislocations are due to residual damage introduced during FIB cutting. The FIB damage is already reduced as far as possible by thinning the lamella with low energy Ar ion milling, see section 3.4. Therefore, this residual FIB damage has to be handled as background. The damaged zone shows a significantly higher dislocation density and is still clearly distinguishable. The shadows in the images Fig. 5.1a - 5.1d are bend contours. A thin lamella is always slightly bent and in these bent regions the two-beam condition is not fully satisfied, resulting in shadows in the image. For analysis of the dislocation microstructure, only the unbent part of the lamella can be taken into account. This area is marked exemplarily in Fig. 5.1c. To investigate the damage region, images at different magnifications were taken, using the transmission electron microscope Jeol Jem 1200 and partly the scanning transmission electron microscope Hitachi HD 2700. The images shown in this chapter were taken with TEM Jeol Jem 1200 unless otherwise noted.

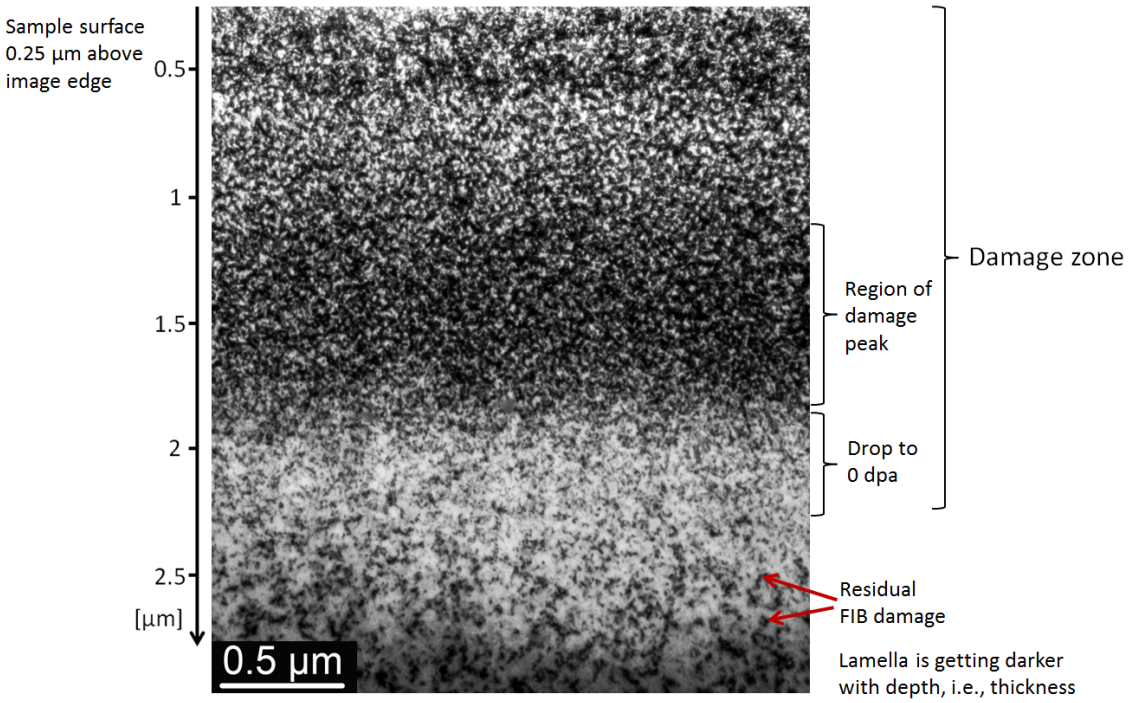

(a) W 0.04 dpa sample, image taken under the two-beam condition **g**=(-200)

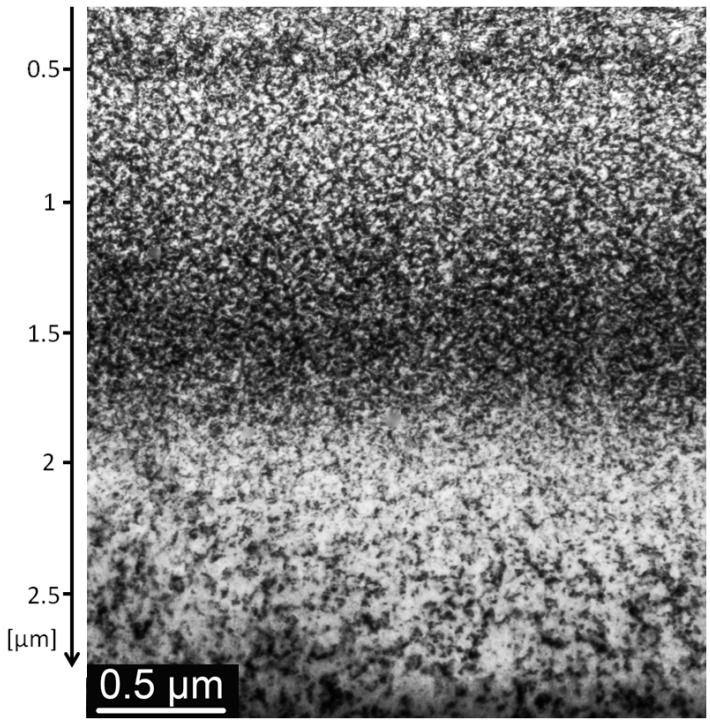

(b) W 0.04 dpa sample, image taken under the two-beam condition **g**=(020)

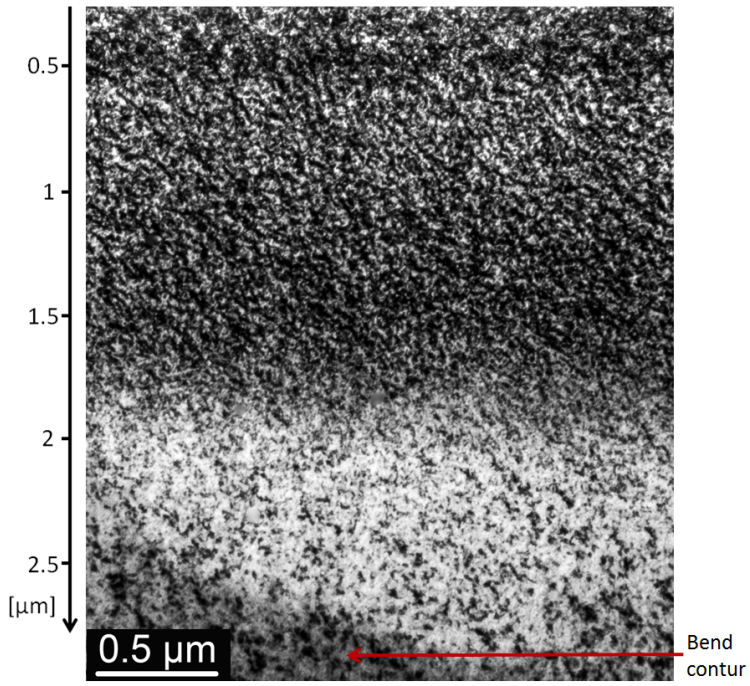

(c) W 0.04 dpa sample, image taken under the two-beam condition **g**=(-110)

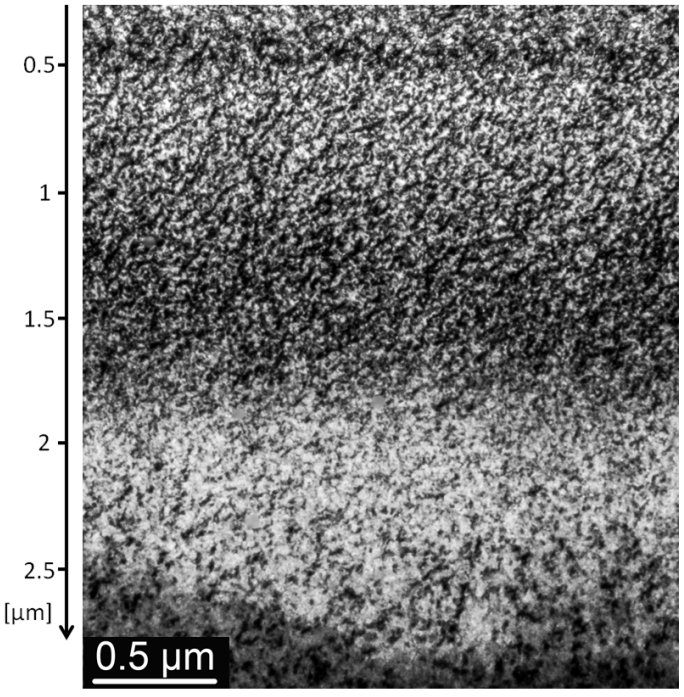

(d) W 0.04 dpa sample, image taken under the two-beam condition **g**=(110)

Fig. 5.1: Tungsten damaged by 20 MeV tungsten ions to a damage level of 0.04 dpa in the damage peak maximum. The images were taken under the four different two-beam diffraction conditions **g**: (-200), (020), (-110), (110)

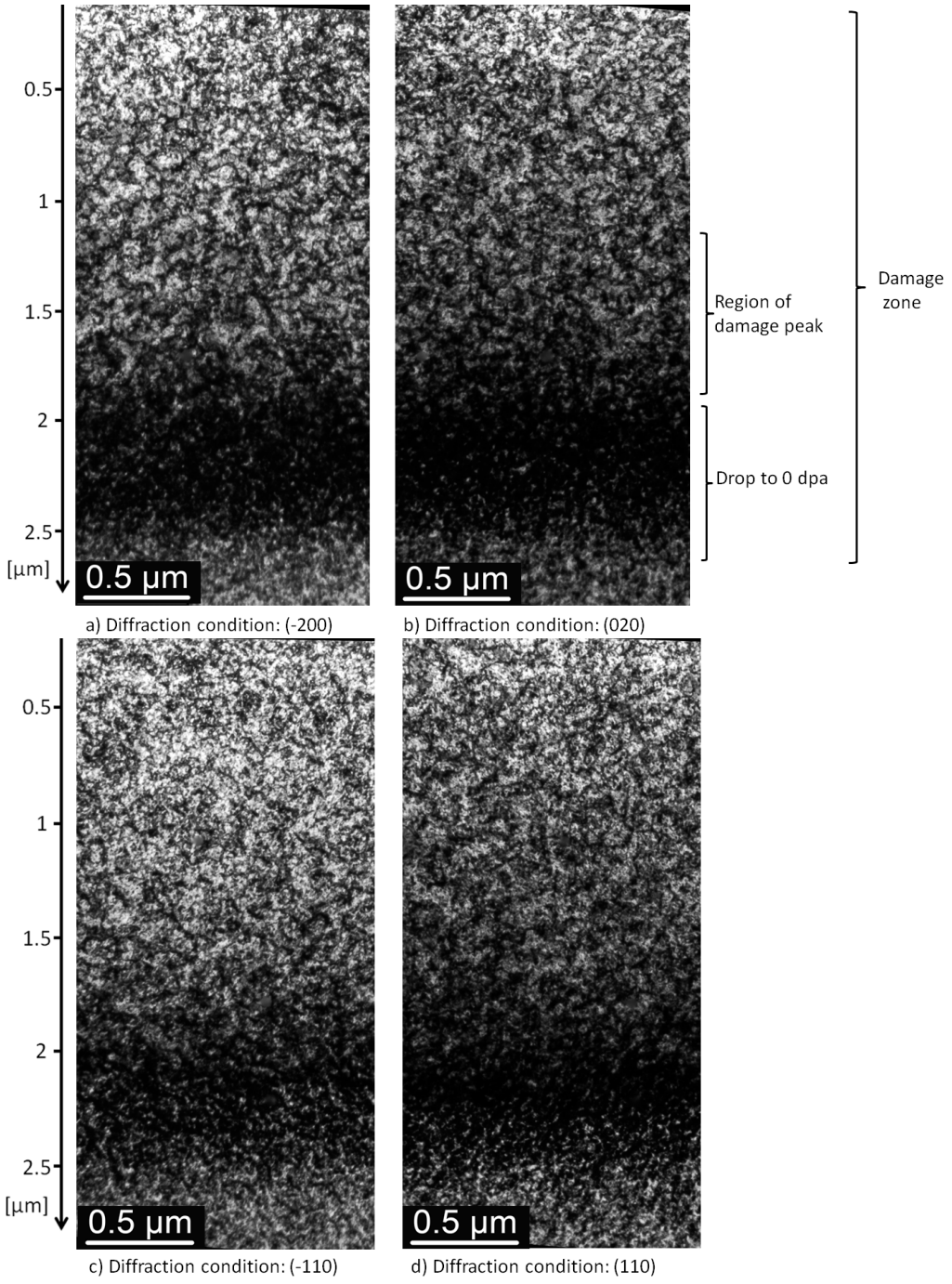

Fig. 5.2: Tungsten damaged by 20 MeV tungsten ions to a damage level of 0.5 dpa in the damage peak maximum. The images were taken under the four different two-beam diffraction conditions **g**: (-200), (020), (-110), (110). The images were rotated such that the sample surface is parallel to the upper image edge.

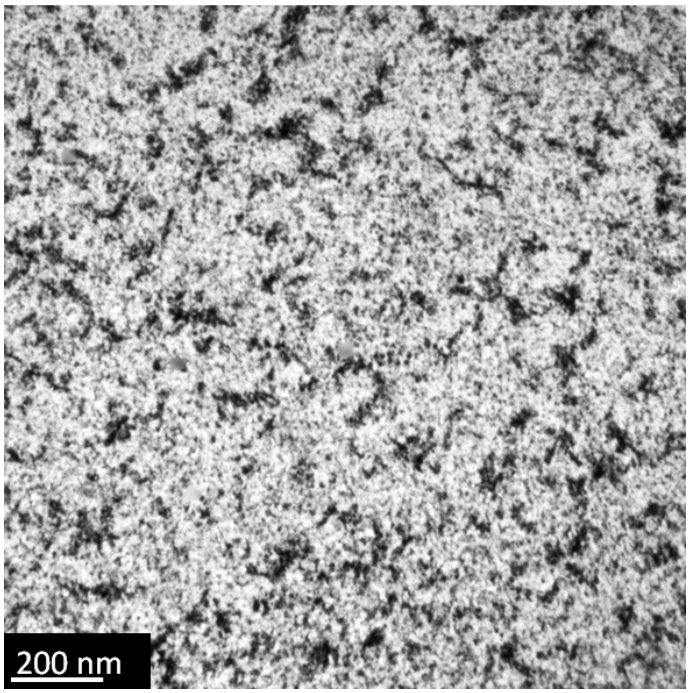

Fig. 5.3: Undamaged tungsten lamella. Image taken at a depth of 0.7-1.7 μm at two-beam condition **g**=(-200). Only residual FIB damage is visible.

5.1.1 Dislocation structure of self-damaged tungsten

Figs. 5.1a-5.1d show an overview of the W 0.04 dpa sample at different two-beam diffraction conditions. From these images the overall appearance of the damage zone under the different diffraction conditions can be studied. In the upper half of the image up to a depth of 1.9 μm, a clearly visible damage zone is observed. At depths larger than 2.3 μm, the typical undamaged tungsten structure with the residual FIB damage is observed. Between the depth 1.9 μm and 2.3 μm, a part of the damage zone is observed which is less clearly visible, this is the drop to 0 dpa. The whole damage zone extends up to 2.3 μm. In comparison, SRIM predicts a deeper damage zone up to 2.5 μm for tungsten irradiated by 20.3 MeV tungsten ions, compare Tab. 5.1. To study the radiation damage in detail, additional images at higher magnifications were taken. Fig. 5.4 shows a magnified image of the damage zone in the depth range of 1.2-1.9 μm taken under the two-beam condition (-110). It can be seen that the radiation damage zone in the W 0.04 dpa sample consists of dislocation loops and not further defined black regions. Dislocation lines are not found throughout the whole damage zone. The black regions diffract the electrons more strongly which means that in these regions the crystal lattice deviates from (100). Further observations at higher magnifications showed that at the edges of those black regions the dislocation loop density is higher than anywhere else in the damage zone. Therefore, it can be concluded that these black regions are agglomerations of dislocation loops also called dislocation loop clusters. Each dislocation creates its own strain field and if the dislocation density in a region is very high, the strain fields sum up and the crystal lattice can get a slightly different crystallographic direction, i.e. the crystal lattice is distorted. This area is then observed as a black region in the BF image. The dislocation density in the sample W 0.04 dpa is apparently so high that in the whole damage zone clusters of dislocation loops, observed as black regions, are formed. Figs. 5.1a-5.1d show that the damage zone is getting darker in the depth of 1.0-1.8 μm, i.e. the damage zone is there dominated by the black regions. Apparently, the dislocation density in this depth is even higher than in smaller depths. This is in good agreement with the calculated damage depth profiles (compare Fig. 4.1). The damage peak for self-damaged tungsten is located in a depth of about 1.3 μm, which corresponds to the depth where many of the black regions are observed. This means that with higher damage level a higher dislocation density in form of the amount of black regions is observed.

Throughout the whole damage zone and in all four two-beam conditions, dislocation loops are observed. At first glance, it seems that the dislocation loop size is always of the same magnitude. To check whether this is indeed the case, the size of around 1000 dislocation loops was measured. First of all, it should be checked whether the average loop size varies with the set two-beam condition at which the image was taken. Therefore, the loop size was measured from four images taken at the different two-beam conditions. The images used for analysis were all taken at a high magnification in a depth of 1.2 - 1.9 μm. In this depth the damage level is well defined as this is the depth at which the damage maximum of 0.04 dpa is reached. Only clearly visible dislocation loops were counted. To measure the dislocation loop size, 200 dislocation loops were marked in each image, i.e. the area enclosed by the dislocation loop was marked. Then the images were binarized and the marked area enclosed by the dislocation loop was evaluated by the graphical software Bruker-CT-Analyser (compare Fig. 5.5). Most of the dislocation loops are not perfectly circular, therefore, a quantity is needed to compare the size of the dislocation loops. For this, the program calculates the equivalent circle diameter given the object area. Fig. 5.6 shows the histograms for the different two-beam diffraction conditions and Tab. 5.2 summarizes the average loop diameters calculated from the 200 loops. To estimate the uncertainty of the average loop diameter, the average diameter was evaluated in this way from the same image three times and from a different image, taken at the same depth in the sample, two times. An uncertainty of ± 0.7 nm of the average dislocation loop diameter was found. From the histograms and the average loop diameters, no significant dependence of the loop size and the set two-beam diffraction condition is found. The average loop diameter is very similar at all four two-beam diffraction condition, see Tab. 5.2. The differences are in the uncertainty margin. Therefore, the dislocation loop size can be averaged over all four two-beam diffraction conditions giving an average loop size of 7.8 ± 0.7 nm. Fig. 5.7 shows the sum histogram of the four histograms.

Incident ion	observed damage depth for 0.04 dpa	observed damage depth for 0.5 dpa	SRIM calculated damage range
W	2.3 μm	2.6 μm	2.5 μm
Si	2.0 μm	2.3 μm	2.2 μm
He	1.9 μm	1.9 μm	1.9 μm
D	2.0 μm	X	2.0 μm
p	1.4 μm	X	1.8 μm

Table 5.1: Observed damage range and calculated damage range for the different samples.

U. von Touissant fitted a log normal distribution (Eq. 5.1) [155] to the sum histogram by minimizing chi^2, compare Fig. 5.7. With Eq. 5.2 [155], the expectation value E(x) and standard deviation $\sqrt{Var(X)}$ of the distribution were calculated and are summarized in Tab. 5.3. The expectation value was found to be 7.32 nm. It is smaller than the arithmetic average as more loops with smaller diameter were found, giving an asymmetric distribution.

$$f(x) = \frac{1}{\sqrt{2\pi}\sigma x} exp\left(-\frac{(ln(x)-\mu)^2}{2\sigma^2}\right) \tag{5.1}$$

$$\begin{aligned} E(x) &= exp(\mu + \frac{\sigma^2}{2}) \\ \sqrt{Var(x)} &= E(x) \cdot \sqrt{exp(\sigma^2 - 1)} \end{aligned} \tag{5.2}$$

It was also checked whether the average loop diameter is similar in different damage depths. For this, dislocation loops were marked on images taken at a damage depth between 0.5 - 1.2 μm. The obtained dislocation loop sizes are in very good agreement with the ones listed in the table. For example, the average loop diameter from 200 loops in a depth between 0.5 - 1.2 μm under the two-beam diffraction condition (-110) is 7.8 nm and under (-200) it is 7.7 nm. This means that in the W 0.04 dpa sample throughout the whole damage zone the dislocation loop size is about identical. Note please that the damage level is not constant with depth as shown in Fig. 4.1. At 0.5 μm depth the damage level is about 0.02 dpa and then reaches 0.04 dpa at a depth of 1.4 μm. Obviously, irradiation of tungsten with tungsten ions to damage levels between 0.02 and 0.04 dpa will lead to identically sized dislocation loops. The dislocation loop density will be different with different dpa but not the size.

Dislocation loop diameter in nm			
Diffraction condition	W 0.04 dpa sample	Si 0.04 dpa sample	D 0.04 dpa
(-200)	7.4 ± 0.7	5.9 ± 1	21.1 ± 0.7
(020)	8.3 ± 0.7	6.9 ± 1	22.1 ± 0.7
(-110)	7.8 ± 0.7	5.5 ± 1	15.8 ± 0.7
(110)	7.5 ± 0.7	7.2 ± 1	15.6 ± 0.7
average diameter	7.8 ± 0.7	6.4 ± 1	15.6 - 22.1

Table 5.2: Average dislocation loop diameter in nm under the different two-beam diffraction condition.

	W 0.04 dpa sample	Si 0.04 dpa sample
expectation value (nm)	7.32	5.82
standard deviation (nm)	2.48	2.10

Table 5.3: Expectation value and standard deviation of the log-normal distribution fitted to data of the W 0.04 dpa sample, compare Fig. 5.7.

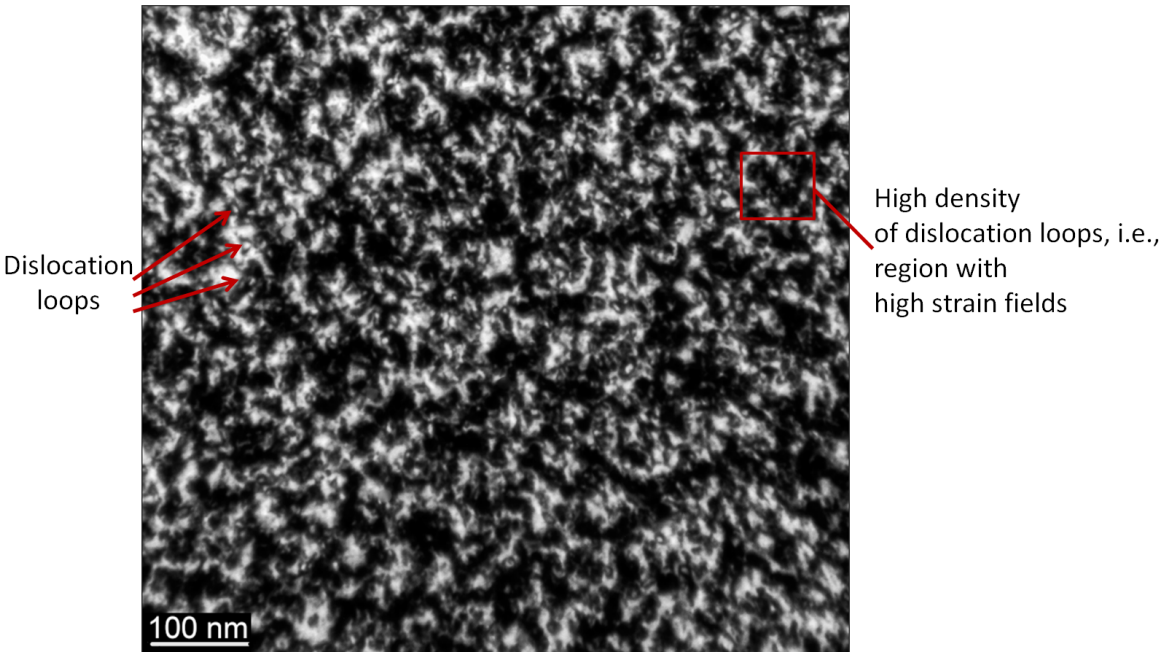

Fig. 5.4: Magified damage zone of sample W 0.04 dpa in a depth of 1.2-1.9 μm under two-beam diffraction condition (-200)

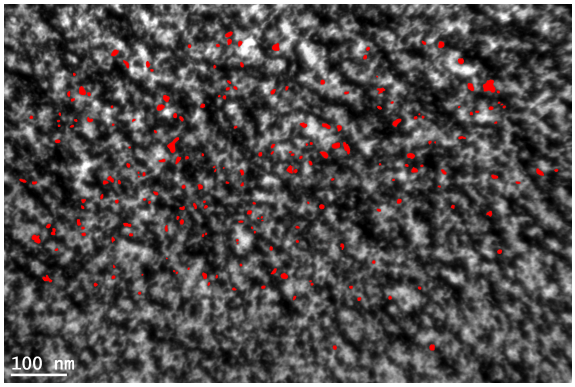

(a) 200 marked dislocation loops in the damage zone of the W 0.04 dpa sample at a depth of 0.5-1.2 μm at the two-beam condition (-110). This depth corresponds to the depth in which the damage peak maximum of 0.04 dpa is reached.

(b) Binarized image of the marked dislocation loops. From this image the image analysis program Bruker CTAn determined the equivalent circle diameter to the area of the dislocation loops.

Fig. 5.5: Procedure for the determination of the dislocation loop size as described in the text.

Let us now turn to the self-damaged tungsten with a damage level of 0.5 dpa. Based on the knowledge gained from the W 0.04 dpa sample, one could naively think that the damage zone in W 0.5 dpa sample will be fully dominated by black regions, as the damage level of this sample is even higher. This is not the case. Figs. 5.2a - 5.2d show an overview for the W 0.5 dpa sample. The damage zone of W 0.5 dpa has a width of 2.6 μm. The damage zone found in W 0.04 dpa has a width of only 2.3 μm. Obviously, the damage level in the W 0.04 dpa sample is already that low at depths larger than 2.3 μm that the radiation damage is not observable any more. Whereas, in the W 0.5 dpa sample, the damage level is over 10 times higher in this depth and, hence, the radiation damage is still observable, which explains the larger observed width of the damage zone in W 0.5 dpa. SRIM calculated a damage zone up to 2.5 μm which is in good agreement with the observed 2.6 μm deep damage zone in W 0.5 dpa, Tab. 5.1. Fig. 5.8 shows the damaged region of W 0.5 dpa sample at a similar depth as does Fig. 5.4 for the W 0.04 dpa sample. The damage zone appears brighter than the damage zone of W 0.04 dpa sample. It consists mainly of dislocation lines and dislocation loops sorted in chains forming a dislocation line network up to a depth of 1.9 - 2.0 μm. Beside the dislocation lines and dislocation loop chains, few isolated dislocation loops are visible which are of comparable size as found in W 0.04 dpa. Between the dislocation line structures, the typical residual FIB damaged tungsten is visible. Hardly any black regions are found up to a depth of 1.9 - 2.0 μm. As no

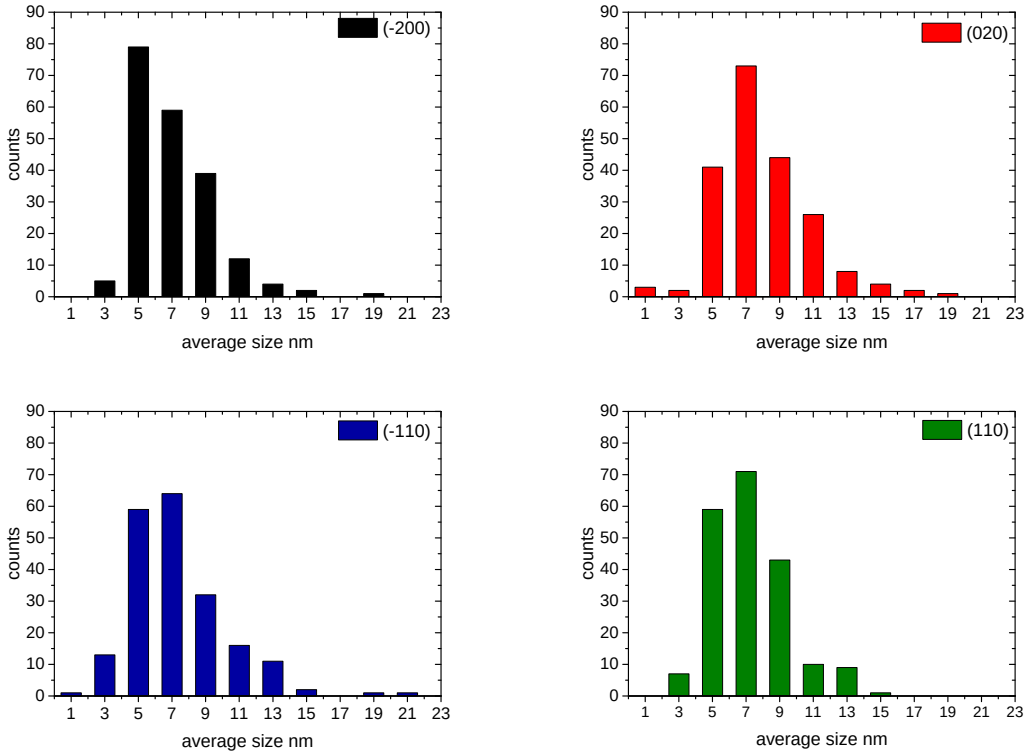

Fig. 5.6: Dislocation loop size distribution in W 0.04 dpa in a depth of 0.5 - 1.2 μm under the different two-beam diffraction conditions: (-200), (020), (-110), (110). Plotted is the equivalent circle diameter obtained from the average object area.

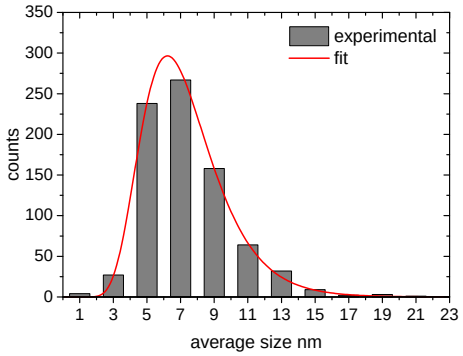

Fig. 5.7: Sum histogram obtained by summing up the histograms at defined two-beam conditions. In total 800 loops in the W 0.04 dpa sample in a depth of 1.2 - 1.9 μm were counted to obtain this histogram.

black regions are observed in this depth the dislocation line density can be estimated with the line intersection method [124, 125]. For this, nine arbitrary lines were drawn in the image at a depth between 1.0 μm and 1.7 μm and the number of dislocation intersections with the lines were counted. With this procedure, the dislocation line density was calculated with Eq.3.5. Tab. 5.4 lists the obtained dislocation line densities under the different two-beam diffraction conditions. It was assumed that the lamella thickness is around 80 nm $\pm$ 10 nm. This value is taken from previous electron energy loss spectroscopy (EELS) measurements of tungsten lamellas. This value is also in good agreement with the thickness estimation done in the FIB microscope when the lamella was positioned edge-on to the viewing direction. The error in the dislocation line density is mainly due to the uncertainty of the lamella thickness and due to the finite number of lines. When comparing the dislocation line densities with the $\mathbf{g}\circ\mathbf{b}$ invisibility criterion in Tab. 5.4 no connection is found within the experimental uncertainty. Therefore, an average dislocation line density can be calculated based on the four two-beam diffraction conditions. The average dislocation line density is $6.5{\cdot}10^{14}\ \frac{m}{m^3}$. This observation shows that with increasing damage level most of the dislocation loops which started to agglomerate (observed at W 0.04 dpa) sort themselves into dislocation loop chains or turned into dislocation lines (observed at W 0.5 dpa). The observed dislocation lines can be either large dislocation loops with a diameter larger than the lamella thickness or are dislocation lines which start and end at vacancy clusters. Between the dislocation lines, no black regions are observed: this means that the strain fields are low. The dislocation line network seems, therefore, energetically more favorable. Hence, a development from dislocation loops with high strain fields at 0.04 dpa to a network of dislocation lines with low strain fields at 0.5 dpa happened. As visible in Figs. 5.2a - 5.2d, starting at a depth of 1.9 - 2.0 μm, again dislocation loops and black regions like in the W 0.04 dpa sample are observed. This region is 0.55 $\pm$ 0.03 μm wide and appears darker due to the presence of black regions. At first glance, one might think that this is the damage maximum like in the W 0.04 dpa sample. This is not the case because, as described above, the dislocation loops develop to dislocation lines at high dpa. From Fig. 4.1, it gets clear that at a depth of 1.9 - 2.0 μm the damage level is already only 0.1 dpa as the dpa levels drops sharply from 0.5 dpa at 1.3 μm to 0 dpa at 2.6 μm. Therefore, at the end of the damage zone in the W 0.5 dpa sample the initial stage of dislocation loops and black regions can be observed as in the 0.04 dpa case.

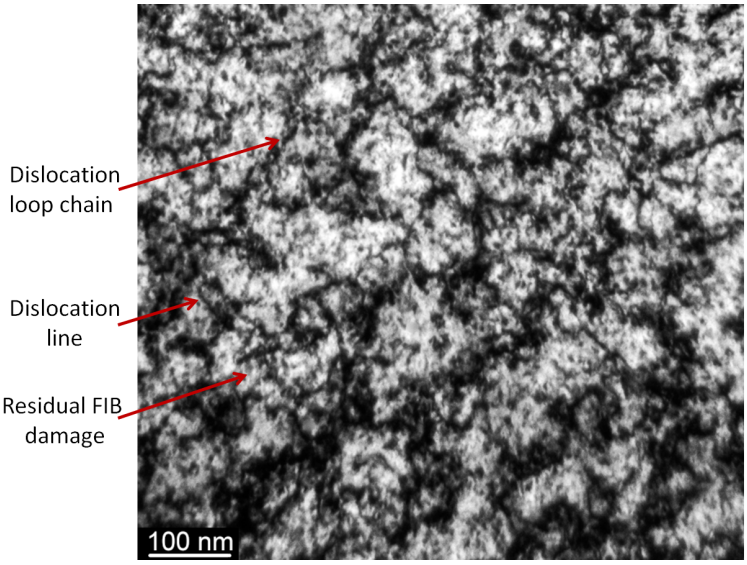

Fig. 5.8: Magified damage zone of sample W 0.5 dpa in a depth of 1.1-1.8 μm under two-beam condition (-200)

5.1.2 Dislocation structure of tungsten damaged by silicon

Tungsten was irradiated to 0.04 dpa and 0.5 dpa with 7.5 MeV Si-ions.
As the Si ions are much lighter than tungsten ions and have a different incident irradiation energy the primary recoil energy spectrum is different. According to Tab. 4.1 the maximum energy of a tungsten recoil atom which had collided in a head on collision with a 7.5 MeV Silicon ion is only 3.5 MeV . Therefore, a difference in the dislocation microstructure can be expected.
First, the Si 0.04 dpa sample will be discussed. In the images of the Si 0.04 dpa sample a damage zone up to a depth of 2 μm is visible, Fig. 5.9. In the first 0.6 μm, only sparse small dislocation loops and dislocation dots are observed. In this work very small dislocation loops of a size of 1-2 nm are called dislocation dots as it is nearly impossible to identify them as loops. From a depth of about 0.6 μm on, larger dislocation loops are found, which are similar in size to the loops found in sample W 0.04 dpa and are starting to dominate the dislocation structure. At a depth of 0.08 –0.1 μm black regions are starting to be visible. As in the W 0.04 dpa samples these black regions are dislocation loop clusters with high strain fields. Apparently, up to this depth the dislocation density is too low and the dislocation loops do not agglomerate, i.e. black regions are not observed. From a depth of 0.8 μm on black regions are observed, meaning that the dislocation loop density is high enough and some dislocation loops agglomerate/cluster and in these agglomerations/clusters the strain fields are high causing a distortion in the crystal lattice. In contrast to the

W 0.04 dpa sample the damage zone of Si 0.04 dpa sample shows only from a certain depth dislocation loop clustering observed as black regions. In the W 0.04 dpa damage zone all over the zone dislocation loops and black regions were observed.
To understand this difference, one has to compare the SRIM calculated damage profiles for tungsten damaged by silicon and self-damaged tungsten from Fig. 4.1. The damage depth profile for tungsten damaged by silicon has a narrower damage peak maximum and the damage level at the surface is smaller compared with self-damaged tungsten. The damage level in 250 nm depth in the Si 0.04 dpa sample is 0.006 dpa and increases to 0.04 dpa at a depth of 1.5 μm. Whereas in a depth of 250 nm the damage level in W 0.04 dpa sample is already 0.02 dpa. In the Si 0.04 dpa damage zone black regions between the dislocations start to be visible at a depth of 0.8 μm. At this depth the Si 0.04 dpa samples is damaged to a damage level of 0.01 dpa whereas the W 0.04 dpa exhibits a dpa level of already 0.03 dpa at this depth. From this comparison with the calculated damage depth profile it is found that up to 0.01 dpa dislocation loops are formed, which are not dense enough to cluster. With increasing depth and, hence, damage level the density of the dislocations increases and at a damage level of about 0.01 dpa it is so high that the dislocation loops cluster and black regions are observed. As the SRIM depth profiles are that different for Si and W a meaningful comparison of the damage zone is only possible in the region of the damage peak maximum. In this region the damage level in both samples is around 0.04 dpa and, hence, comparable. The damage zone of Si 0.04 dpa seems to be very similar to W 0.04 dpa. Nevertheless it seems that the dislocation loops found in the region of the damage peak maximum are somewhat smaller than the loops found in W 0.04 dpa.
To quantify this statement around 800 dislocation loops in a depth of 1.1–1.8 μm were counted, which is the region of the damage peak. As in the case of the W 0.04 dpa sample the loop sizes under the two-beam diffraction conditions:
(-200), (020), (-110), (110) were determined. The results are summarized in Tab. 5.2. No dependence between the set two-beam diffraction condition and loop size was found. The average dislocation loop diameter in the Si 0.04 dpa is 6.4 nm. As for W 0.04 dpa a log normal distribution was fitted to the sum histogram Fig. 5.11. The results are summarized in Tab. 5.3. The expectation value was found to be 5.82 nm. It seems that the dislocation loops found between 0.6 μm and 1.1 μm are all of a similar size as in the damage peak region of 1.1–1.8 μm. To check this statement additional 200 dislocation loop were counted in the depth between 0.8 μm and 1.2 μm. Indeed the average dislocation loop diameter found in these depth is nearly identical.

To estimate the uncertainty of the determined average dislocation loop diameter each image was analyzed several times. An uncertainty of ±1 nm was determined. This uncertainty is slightly higher than in the W 0.04 dpa sample. The reason for it is the high number of small dislocation loops in the Si 0.04 dpa sample which make the procedure more difficult giving an uncertainty of ±1 nm.
Summarizing, between 0.8 - 2 μm also no dependence was found between the damage depth and dislocation loop size. From 0.8 μm up to the end of the damage zone and in all four two-beam diffraction conditions the size of the dislocation loops is the same. Tab. 5.2 summarizes the observed average diameter under the different two-beam diffraction conditions.
The average dislocation loop diameter in the Si 0.04 dpa is 6.4±1 nm. It is indeed smaller than the average loop diameter found in self-damaged tungsten W 0.04 dpa of 7.8±0.7 nm. Taking the uncertainties into account the difference does not seem to be large. The expectation value obtained from the fit to the histogram, is for Si 0.04 dpa 5.82 nm and for W 0.04 dpa it is higher namely 7.32 nm. When comparing this difference with the differences in the recoil energy spectra Fig. 4.2 and Tab. 4.1 during the irradiation with 7.5 MeV Si ions and 20 MeV tungsten ions, the difference in the dislocation loop diameter can be considered to be small. Fig. 5.11 shows the sum histogram obtained by summing up the histograms for the four two-beam diffraction conditions. Comparing the sum histograms from sample Si 0.04 dpa and sample W 0.04 dpa shows that more small sized loops are found in the Si 0.04 dpa sample.

Dislocation line density in $10^{14}\frac{m}{m^3}$		
Diffraction condition	W 0.5 dpa sample	Si 0.5 dpa sample
(-200)	6.0±1.0	6.0±1.0
(020)	6.2±1.0	5.0±1.0
(-110)	6.7±1.0	5.7±1.0
(110)	7.2±1.0	6.2±1.0
average dislocation line density	6.5±1.0	5.7±1.0

Table 5.4: Dislocation line density in W 0.5 dpa Si 0.5 dpa obtained by the line intersection method.

Fig. 5.10 shows the Si 0.5 dpa sample. The damage zone is 2.3 μm wide, which is again in good agreement with the calculated damage depth of 2.2 μm by SRIM, Fig. 4.1. In the Si 0.5 dpa sample dislocation lines and chains of dislocation loops and few isolated dislocation loops and hardly no black regions up to a depth of 1.9 μm are found. That means that also in the case of tungsten damaged by silicon ions with further irradiation most of the dislocation loops with high strain fields in between (observed in the Si 0.04 dpa sample) turn into dislocation lines or sort themselves in chains with low strain fields (observed in Si 0.5 dpa). This dislocation line network is very similar to the W 0.5 dpa sample. The dislocation line density in a depth of 1.0 - 1.7μm was again determined by the line intersection method. The dislocation densities under the four two-beam diffraction conditions are listed in table 5.2. The average dislocation line density in Si 0.5 dpa is $5.7 \cdot 10^{14}\frac{m}{m^3}$. It is slightly lower than the dislocation line density in W 0.5 dpa. From the calculated damage depth profile for the Si 0.5 dpa, it can be deduced that at the depth of 0.25 μm the damage level is about 0.08 dpa. At this depth a dislocation line network is already observed in the image. From this we can conclude that between 0.08 dpa -0.1 dpa most of the dislocation loops sort themselves into chains or turn into dislocation lines. At the end of the damage zone starting at a depth of about 1.9 μm a zone with dislocation loops and black regions of a width of 0.35 $\pm$0.03 μm is found. At this depth the damage level is about 0.1 dpa. This is again very similar to the W 0.5 dpa sample with the difference that the dislocation loop zone in W 0.5 dpa is wider, namely 0.55$\pm$0.03 μm. This can be also well understood when comparing the calculated damage depth profiles. The Si damage depth profile decreases more steeply than the W damage depth profile and this is observed as a narrower dislocation loop zone at the end of the damage zone in the Si 0.5 dpa sample than in the W 0.5 dpa sample.

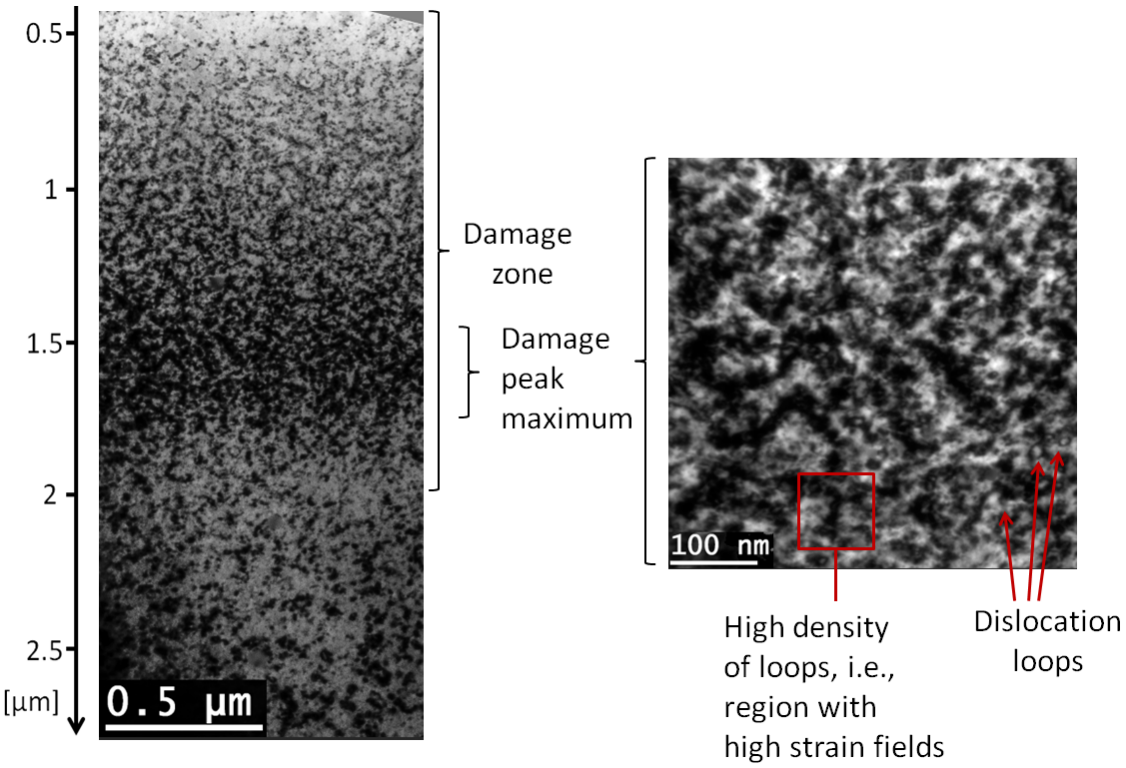

Fig. 5.9: Tungsten damaged by silicon to a damage level of 0.04 dpa in the damage peak maximum under the two-beam diffraction condition (020). The left image is showing an overview over the whole damage zone. The image was rotated such that the sample surface is parallel to the upper image edge. The right image is an image taken at higher magnification in the damage peak maximum depth.

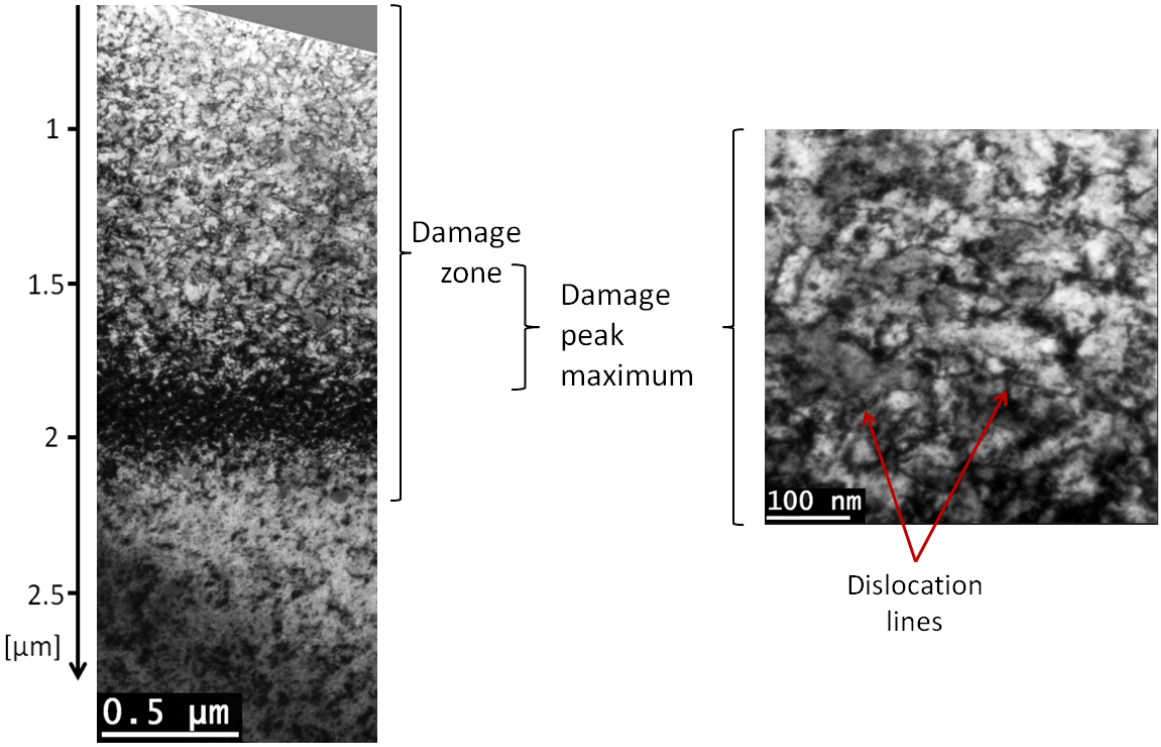

Fig. 5.10: Tungsten damaged by silicon to a damage level of 0.5 dpa in the damage peak maximum under the two-beam diffraction condition (020). The left image is showing an overview over the whole damage zone. It image was rotated such that the sample surface is parallel to the upper image edge. The right image is an image taken at higher magnification in the damage peak maximum depth.

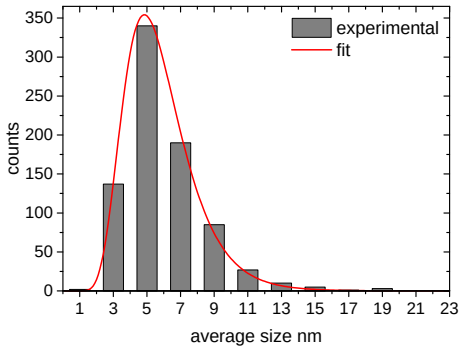

Fig. 5.11: Sum histogram obtained by summing up the histograms at defined two-beam diffraction conditions. In sum 800 loops in Si 0.04 dpa sample in a depth of 0.5-1.2 μm were counted to obtain this histogram.

5.1.3 Dislocation structure of tungsten damaged by helium

Tungsten was also irradiated with the low mass ion He to a damage level of 0.04 dpa and 0.5 dpa. The maximum energy of a recoil after a head on collision with a 1 MeV He ion is 80 keV. Therefore, the recoil energy spectrum strongly differs to the medium to high mass ions, Fig. 4.2. This results in less damage produced by the tungsten recoils. 40% of the radiation damage is done by the incident He ions itself. This is not the case in the W or Si irradiation where most of the damage originates from the recoil atoms: During W irradiation only 2% of the radiation damage are caused by the incident ions. In the Si irradiation it is already 12%, compare Tab. 4.2.
Figs.5.12 and 5.14 show the images of the irradiated tungsten with He: He 0.04 dpa sample and He 0.5 dpa sample, respectively.
First, the He 0.04 dpa sample is discussed. The damage zone extends up to 1.9 μm depth and four different subzones can be distinguished. Fig. 5.13 shows the STEM image of the He 0.04 dpa sample in which the whole damage zone with the surface is visible. In the first 120-150 nm, a zone of dense dislocations and few black regions is observed (zone 1). Such a zone up to 0.2 μm was also observed at some not irradiated tungsten samples. Therefore, zone 1 can be an artifact introduced during the preparation of the lamella. Up to a depth of 1.1-1.2 μm, only sparse small dislocation loops and dots are found (zone 2). Between 1.2 μm and 1.6 μm, an almost fully black zone is found (zone 3). In this zone, the dislocation density is very high and, therefore, the zone is dominated by dislocation loop clusters with high strain fields, observed as black regions. This zone corresponds to the damage peak maximum. From Fig. 4.1, it is known that the 0.04 dpa level is reached at 1.4 μm depth. Zone 3 is 0.4 μm wide which is in perfect agreement with the calculated damage depth profile shown in Fig. 4.1 which gives a damage peak FWHM of 0.4 μm. It is almost impossible to identify single dislocation loops in this zone. Below the damage peak follows a zone of only small dislocation loops and dots up to 1.9 μm (zone 4), which is assigned to the drop from the half maximum to 0 dpa until the typical undamaged tungsten dislocation structure is visible. From the analysis of the Si 0.04 dpa sample, it was concluded that at >0.01 dpa the dislocation loop density is so high that they start to agglomerate and form black regions. Exactly this is also observed in Fig. 5.12. At 1.1 μm, the damage level of around 0.01 dpa is reached as shown in Fig. 4.1.
On the other hand, the damage zone of He 0.04 dpa is different in comparison to Si 0.04 dpa or W 0.04 dpa. In the W 0.04 dpa only one zone dominated by black regions could be distinguished. In the Si 0.04 dpa damage region, a smooth transition

from a zone of isolated dislocation loops to a zone dominated by dislocation clusters and black regions is observed. In contrast, in the He 0.04 dpa sample four distinct subzones in the damage zone are observed. This shows that He as a light ion produce a totally different damage zone as Si or W. As in the damage peak, the single dislocation loops are not visible due to the high strain fields, the size of the dislocation loops was determined in a depth between 0.7-1.0 μm. In this zone mainly dislocation loops visible as dislocation dots of a size from 1 nm - 3 nm are present, which is close to the maximum possible image resolution. Hence, a specification of the average size of the dislocation loops is not possible. The average size of 100 dislocations, which were clearly visible as dislocation loops, was determined under $\mathbf{g}$=(200) to be 5±1 nm.

Tungsten was also irradiated with He to a 0.5 dpa level. This lamella had to be more thinned than the other lamellas otherwise the damage zone was only one black zone. No single dislocation lines or loops could be observed. It seemed that the crystal has a totally different crystallographic direction. By analyzing the diffraction pattern of the damaged zone and the undamaged tungsten, it was found that the crystallographic direction is identical. Therefore, it can be concluded that the damage zone is dominated by high strain fields causing locally a high crystal distortion. This results in many dense black regions observed as one black zone. After further thinning, the dislocation structure started to be visible, see Fig. 5.14. One could expect from Si 0.5 dpa and W 0.5 dpa sample that in the He 0.5 dpa sample a network of dislocation lines will be found. This is, however, not the case. Many small loops with high strain fields in between them (visible as black regions) are found. These small loops have formed a sort of lines but they did not turned into dislocation lines as in W 0.5 dpa or Si 0.5 dpa sample. The whole damage zone has a very high strain field, therefore, it is clear that this situation is energetically not favorable. Obviously, something is preventing the loops to join to larger dislocation loops or lines and to form an energetically favorable dislocation line network. He bubbles in tungsten irradiated by He to similar dpa values were observed in many other studies [151, 156, 157], and could be the underlying reason. Therefore, it was decided to look for He bubbles in a He 0.5 dpa sample at high magnification with the Hitachi HD STEM 2700. Polycrystalline tungsten irradiated with He to 0.5 dpa was taken for this study. To be able to see small bubbles the sample had to be even thinner (20–50 nm) than for the dislocation microstructure studies. In a nearly two-beam BF image, the dominant contrast is the diffraction contrast. However, the mass contrast is also observable. In a high angle angular dark field (HAADF) image the dominant contrast is the mass contrast. Fig. 5.15a shows the BF image of the

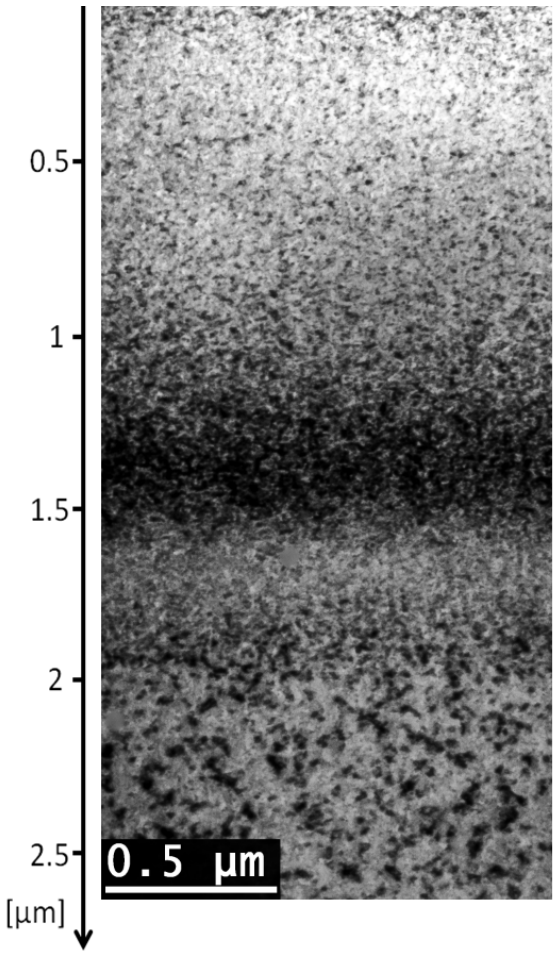

Fig. 5.12: Tungsten damaged by helium to a damage level of 0.04 dpa in the damage peak maximum under the two-beam diffraction condition (020).

He 0.5 dpa sample and Fig. 5.15b shows the HAADF image of the He 0.5 dpa sample at the same sample position. In the BF image small white dots are visible. These dots are not small dislocation loops as they would appear black, in the BF image. In a BF image thicker regions appear dark due to mass contrast, therefore, these bright dots might be missing material, i.e. voids or bubbles. If these bright dots are voids or bubbles they will appear as dark dots in the HAADF image. Fig. 5.15b shows the HAADF image of the same sample position. Indeed most of the bright dots appear as dark dots in the HAADF image. This result is a hint that He bubbles of a size of about 1 nm are present. The He bubbles can be preventing the small dislocation loops to join together to form large dislocation loops, i.e. a dislocation line network similar to the W 0.5 dpa or Si 0.5 dpa sample.

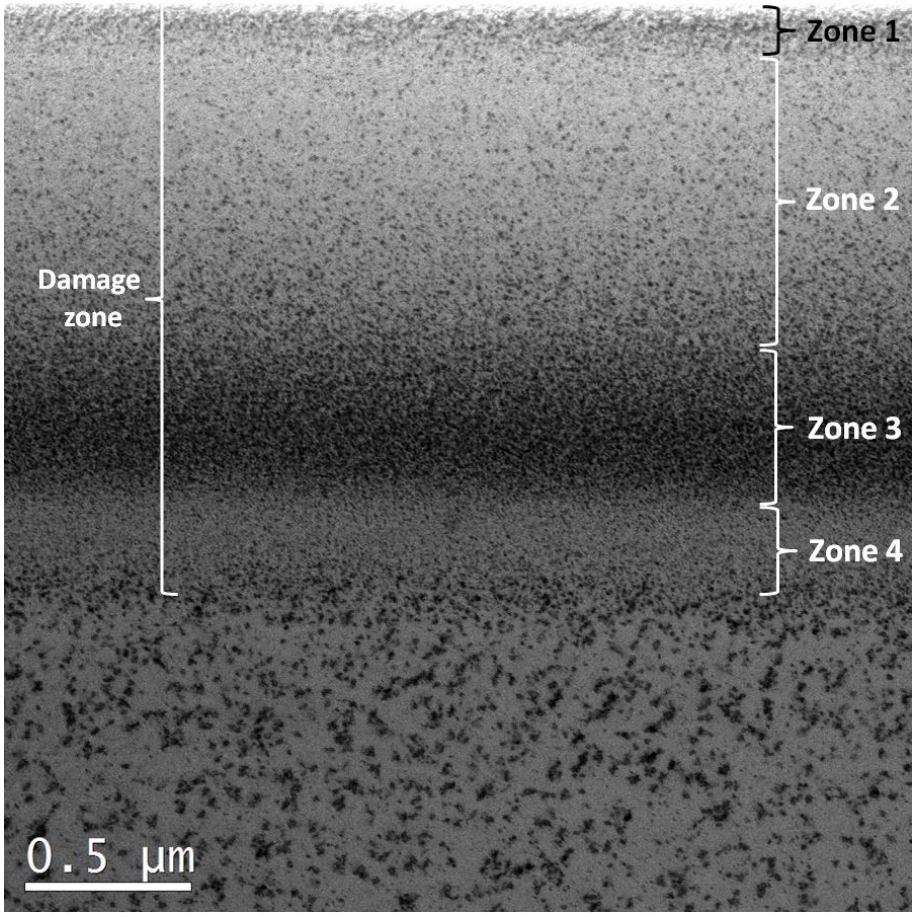

Fig. 5.13: STEM image of tungsten damaged by helium up to a damage level of 0.04 dpa in the damage peak maximum. In this image, the four zones of the damage zone are especially well visible. Zone 1: small dislocation loops and black region
Zone 2: sparse dislocation dots and small dislocation loops.
Zone 3: dislocation loops with high strain fields in between (damage peak).
Zone 4: sparse dislocation dots and loops (drop to 0 dpa).

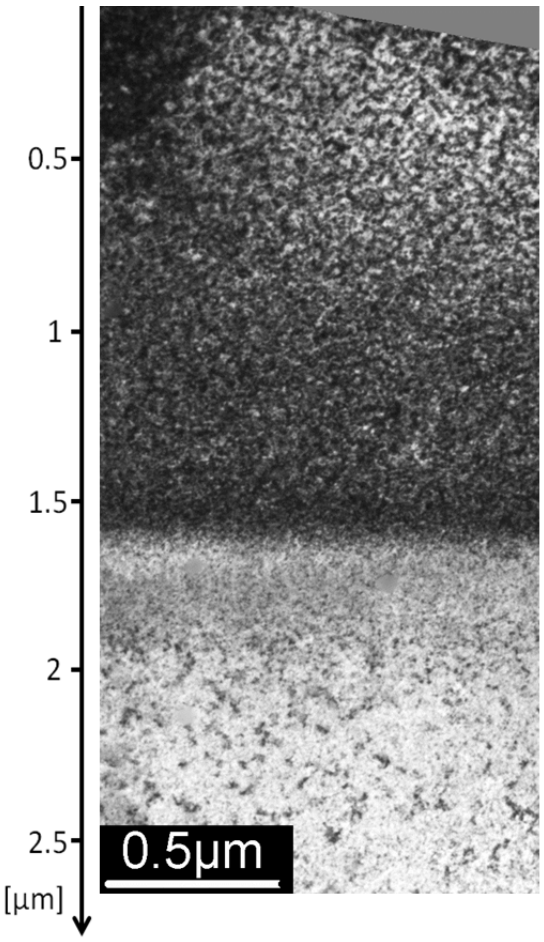

Fig. 5.14: Tungsten damaged by helium to a damage level of 0.5 dpa in the damage peak maximum under the two-beam diffraction condition (020). The image was rotated such that the sample surface is parallel to the upper image edge.

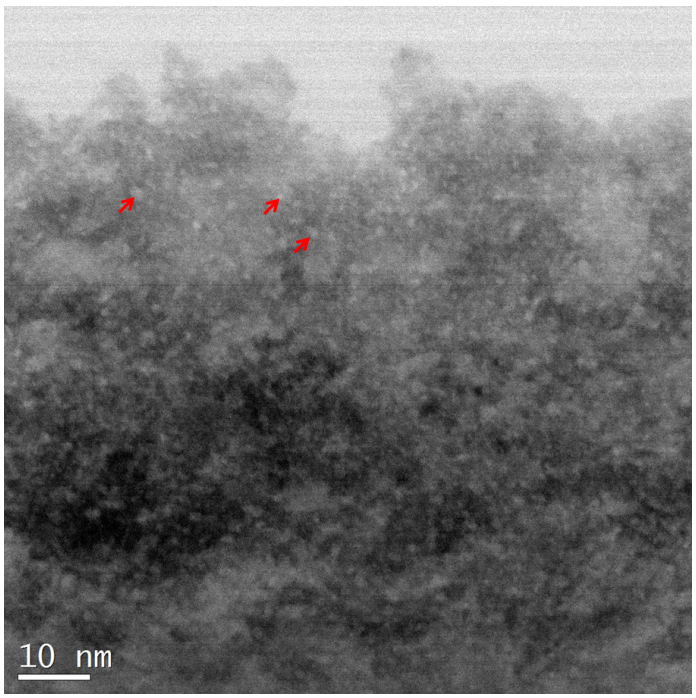

(a)

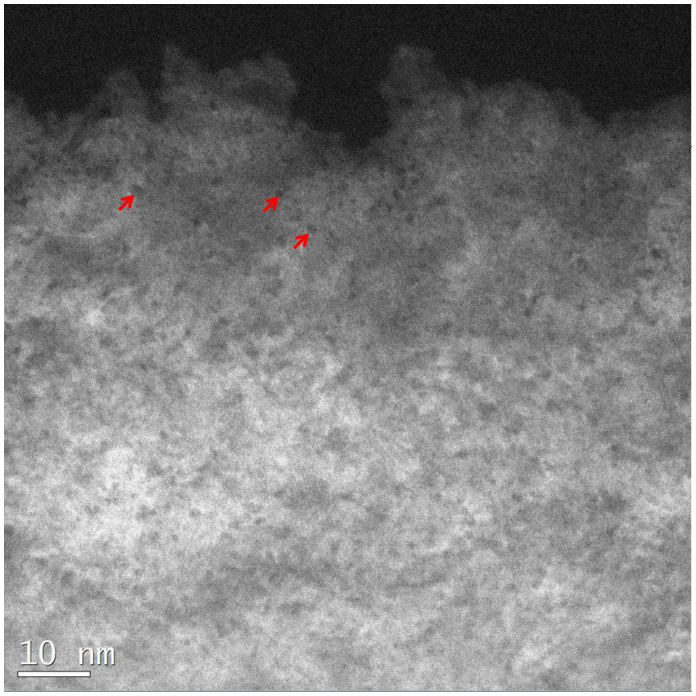

(b)

Fig. 5.15: STEM images of He 0.5 dpa taken at high magnification with Hitachi HD 2700. The upper image (a) is a BF image. The lower image (b) is a HAADF image of the same sample position. The white dots in the BF image which appear as black in the HAADF image are probably He bubbles. The red arrows show exemplarily few He bubbles.

5.1.4 Dislocation structure of tungsten damaged by deuterium

Tungsten was also damaged by deuterium to a damage level of 0.04 dpa. Deuterium is a low mass ion, hence, some similarity to the He damage zone can be expected. However, hydrogen bubbles are not expected. They were observed at higher fluences in literature [152–154], therefore, there may be significant differences to He. Fig. 5.16 shows the damage zone of tungsten damaged by deuterium at the two-beam diffraction condition (020). The damage zone is 2 μm thick.
Similar to the He 0.04 dpa sample, four distinct damage zones can be observed. The first 0.3 μm (zone 1) is characterize by dense dislocations and black regions. Up to a depth of 1 μm only sparse, small dislocation loops and dots are found (zone 2). Between 1 and 1.6 μm, a zone with large dislocation loops is found (zone 3). This depth corresponds to the damage peak depth where 0.04 dpa is reached. Below this a zone of only small dislocation loops and dots follows down to 2 μm (zone 4) which is similar to zone 2. This zone 4 is assigned to the tail of the damage depth profile. The dislocation loops in zone 3 observed under two-beam diffraction conditions(020) and (-200) seems larger than these observed under (-110) and (110). To check whether the dislocation size in the damage peak maximum region depends on the two-beam diffraction condition again 200 dislocation loops at each two-beam condition were counted. Fig. 5.17 shows the histograms at the different two-beam diffraction conditions. The average diameter under (-200) is 21.1 nm, and under (020) it is 22.1 nm, whereas under (-110) it is only 15.8 nm, and under (110) it is 15.6 nm. The uncertainty is estimated to be 0.7 nm. The histograms also show that large sized loops are found mostly for **g**= (020) and (-200). It has to be noted that in no other sample such large dislocation loops were found. When comparing this to the invisibility criterion **g**$\circ$**b** from Tab. 3.1, the large loops can be of type $\langle 111 \rangle$ as all four types of $\langle 111 \rangle$ are visible under (-200) and (020), and only 1/2 of this type of loops are visible under (-110) or (110), compare Tab. 3.1. This is not the case for the $\langle 100 \rangle$ type or $\langle 110 \rangle$ type dislocations. A part of those dislocations also vanish under **g**= (-200) and (020). As under (-110) and (110) not all $\langle 111 \rangle$ type dislocation disappear this is also an explanation why some large sized loops are found under these two-beam diffraction condition.

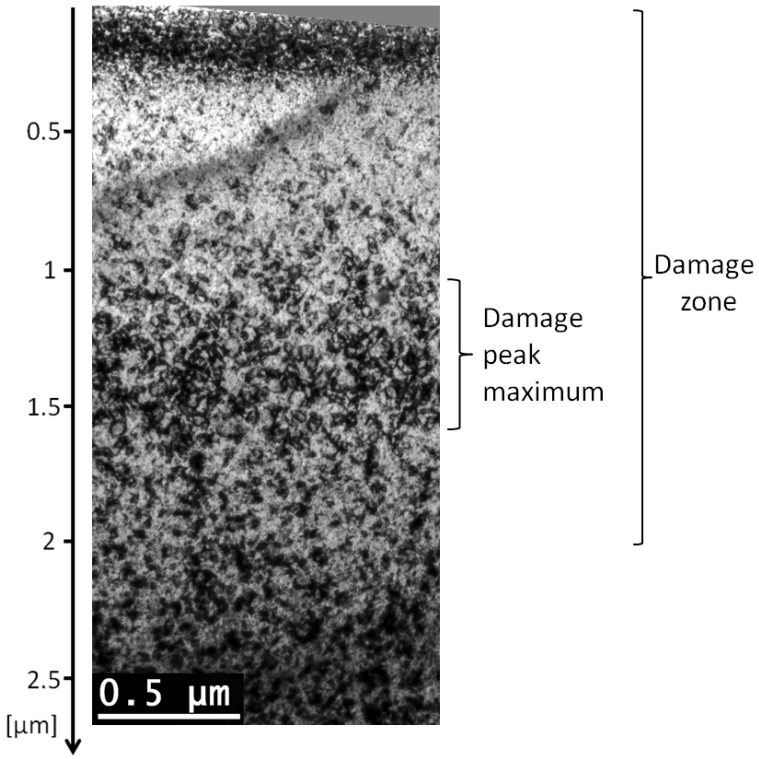

Fig. 5.16: Tungsten damaged by deuterium to a damage level of 0.04 dpa in the damage peak maximum under the two-beam condition (020). The same four zones as in He 0.04 dpa sample (compare Fig. 5.13) are observed. The image was rotated such that the sample surface is parallel to the upper image edge.

Summarizing, tungsten irradiated with D shows indeed similarity to tungsten irradiated with He as the same four distinct damage zones are observed. One significant difference is that large dislocation loops with an average diameter of 15-22 nm are observed in the depth of the damage peak maximum (zone 3). It seems there is no process which hinders the dislocation loops to grow to such large diameters.

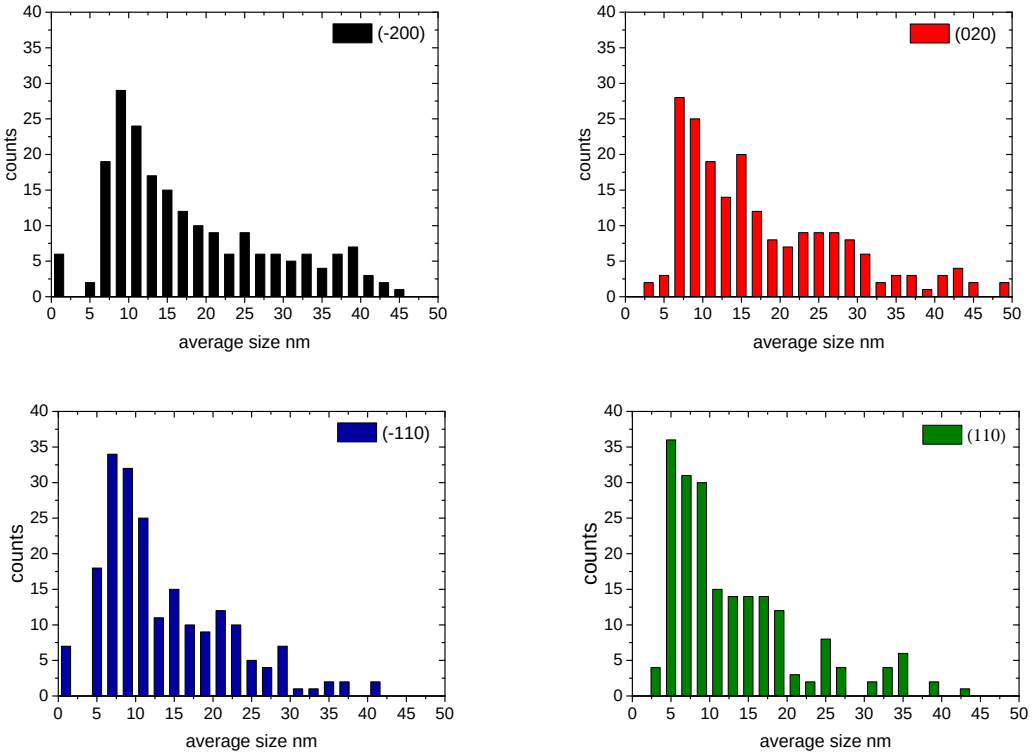

Fig. 5.17: Dislocation loop size distribution in D 0.04 dpa in a depth of 1.0-1.7 μm under the different two-beam conditions: (-200), (020), (-110), (110). Plotted is the equivalent circle diameter obtained from the average object area.

5.1.5 Dislocation structure of tungsten damaged by protons

Tungsten was also damaged by protons to 0.04 dpa. Fig. 5.18 shows an overview of the damage zone of H 0.04 dpa sample. Unfortunately, the lamella was of bad quality which can be seen in the large amount of FIB damage in the lower part of the image. As the diffraction contrast in the STEM images obtained from Hitachi STEM HD 2700 is not that strong as in images from Jeol Jem 1200, it was decided to show the STEM images of this sample for a better visibility of the damage zone. The analysis under the four two-beam diffraction conditions was done with images taken with Jeol Jem 1200 and will be discussed. Fig. 5.18 shows the BF image and the dark field (DF) image of the damage zone. In a dark field image dislocations appear bright which make them better visible. As in the D 0.04 dpa and He 0.04 dpa we see below the surface, a zone of small dislocation loops up to a depth of 0.3 μm (zone 1). Below this, a zone of small dislocation loops and dots is observed. From a depth of 0.6 to 1.4 μm a zone with dislocation loops and long dislocation lines is observed. The depth of this zone corresponds to the depth of the damage peak maximum (see damage depth profile in Fig. 4.1). A zone 4 as in the samples He 0.04 dpa and D 0.04 dpa was not observed, but this is probably due to the bad quality of the lamella. The sample was investigated with the TEM Jeol at the four two-beam diffraction conditions. In (-200) and (020) the dislocation lines are clearly visible in zone 3. In (-110) and (110) the long dislocation lines are not visible and, therefore, the whole damage zone is weaker visible. Most of the dislocation lines is vanishing under the two-beam diffraction conditions (-110) and (110) and are well visible under (-200) and (020). This is a hint that these long dislocation lines have a Burgers vector of type $\langle 111 \rangle$ as the large dislocation loops in the D 0.04 dpa sample.

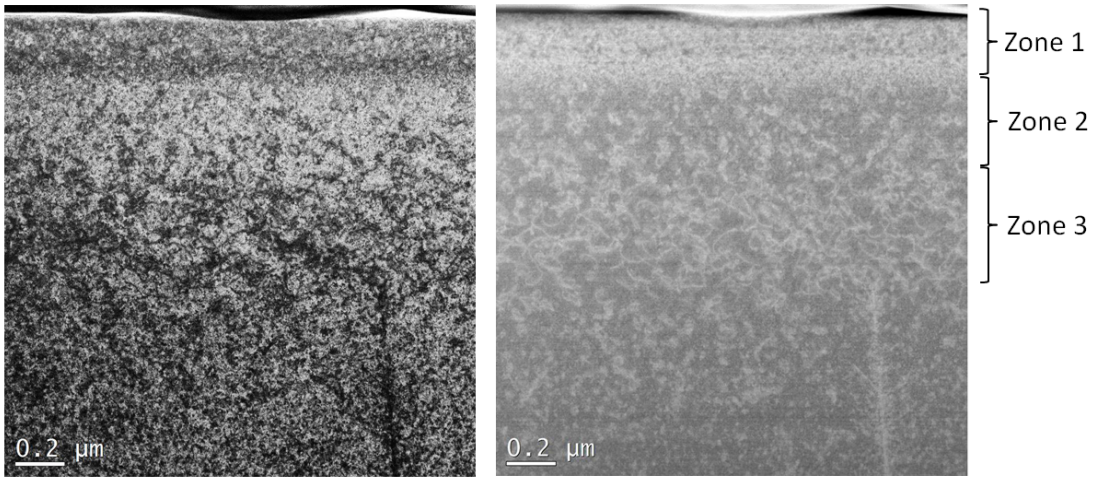

Fig. 5.18: Images of the damage zone of tungsten damaged by protons (p 0.04 dpa sample) taken by the STEM HD 2700. For better visibility of the damage zone, a bright field image (right side) and a dark field image (left side) are shown. In a BF image the dislocation lines or loops appear black. In a DF image the contrast is inverted, i.e. the dislocation loops and lines appear white. The same first three distinct zones in the damage zone as in He 0.04 dpa and D 0.04 dpa samples are observed (compare Fig 5.13, Fig. 5.16). Zone 4 is not visible, probably, due to the bad quality of the lamella.

5.1.6 Advanced quantitative analysis of the TEM images

To observe all dislocations and to investigate the existence of dominant Burgers vectors, each sample was observed under at least four diffraction conditions. Because of the $\mathbf{g} \circ \mathbf{b}$ invisibility criterion, dislocations with a Burgers vector perpendicular to the diffraction vector are not visible. The samples were, therefore, brought into the zone axis [100] and then tilted to the four diffraction conditions (-200), (020), (-110) and (110). Figs. 5.1a-5.1d show the W 0.04 dpa sample under these four diffraction conditions. Looking at the recorded images, it seems that the amount of damage is always comparable in the four different diffraction conditions. Of course, this impression has to be verified by a more quantitative method than just the visible appearance. For the samples W 0.5 dpa and Si 0.5 dpa, the dislocation line density was determined by the line intersection method (Tab. 5.4) and indeed the dislocation line density was the same within the error bars under all four diffraction conditions. For the He 0.04 dpa, He 0.5 dpa, Si 0.04 dpa and W 0.04 dpa this method could not be applied because of the large amount of black regions in the damage zone. It is very difficult to quantify the number of dislocations in these black regions as single dislocation loops are only weakly visible at the edge or are not visible at all in these regions. In this case, the line intersection method as well as manual counting of

dislocations is impossible. Therefore, a method is needed which gives the amount of damage in the samples without the need to count single dislocations. A method was developed to quantify the amount of radiation damage observed in the images. The TEM images for each diffraction condition were binarized using the programme Bruker-CT-Analyser. Before the binarization was conducted the region in the image which should be analysed was chosen. Usually, bend contours are visible which would complicate the setting of the binarization threshold due to a different grey scale histogram. Therefore, only regions of the image free from such artifacts were used, shown exemplarily by the red frame in Fig. 5.1c. This part of the image was used in the binarization and is shown in Fig. 5.19a. The binarization was performed in two steps. In the first step, a global binarization was performed in which the program sets all grey values below a threshold value to black and the grey values above the threshold are set to white, compare Fig. 5.19b. The image after this global binarization reproduces the microstructure only very roughly. To reproduce also smaller structures in the TEM image, in the following step, adaptive binarization is performed at the TEM image parts not excluded by the global binarization. For the adaptive binarization, two parameters are needed: a radius given as the number of pixels and a constant given in the difference in grey values. The program then analyses the image in the specified radius step by step. If in this radius the difference between the grey values is higher than the value set in the constant, these pixels will be set to black otherwise to white. With this procedure, smaller structures can be also analyzed and artifacts because of changing lamella thickness are minimized. The threshold for the global binarization, the radius and the constant for the adaptive binarization were chosen manually for each image such that the final binarized image reproduces the dislocation structure seen in the image best, compare Fig. 5.19c.
From the binarized images the fraction of black pixels was counted for each line of pixels with the program Micrometer, developed at WUT [158, 159], giving the fraction of black pixels with respect to the depth, compare Fig. 5.20. It should be noted that with this method not the dislocation density is counted but the appearance of the radiation damage. The information whether loops, lines or black regions were observed is lost. The result is a dimensionless number: the fraction of black pixels. As shown in the previous Sect. 5.1.1, 5.1.2 in the dpa range between 0 and 0.08 dpa for Si and W irradiation a higher irradiation dose causes a higher density of dislocation loops with more black regions, i.e. a higher fraction of black pixels in the binarized image with damage level. This situation changes at a damage level between 0.08 - 0.1 dpa with the loop-to-line transition. At damage levels higher than 0.1 dpa, a dislocation line network with hardly any black regions is found.

(a) TEM image of W 0.04 dpa before binarization

(b) Binarized image after global binarization

(c) Final binarized image after adaptive binarization

Fig. 5.19: Binarization of the image of the W 0.04 dpa sample.

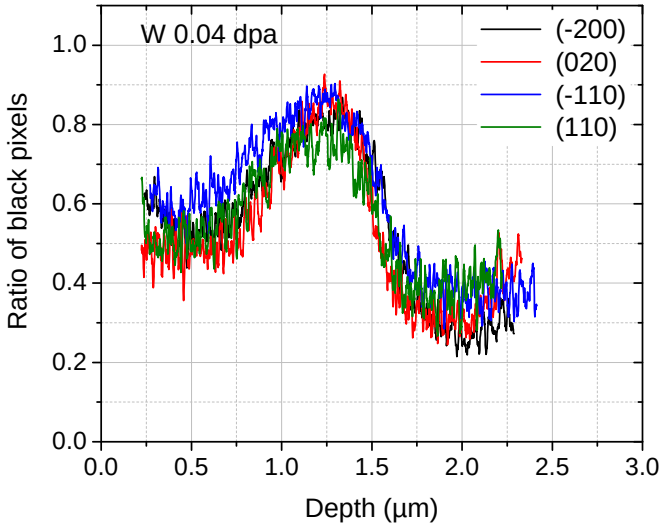

Fig. 5.20: Fraction of black pixels versus depth found in the W 0.04 dpa sample from the binarized image for the four different diffraction conditions.

Therefore, tungsten irradiated by Si and W with damage levels not higher than 0.1 dpa can be investigated with this method. In tungsten damaged by He, no loop-to-line transition was observed (Sect. 5.1.3). In this case, a higher damage level up to 0.5 dpa means a higher dislocation loop density with more black regions, i.e. a higher fraction of black pixels in the binarized images with damage level. Hence, for the samples W 0.04 dpa, Si 0.04 dpa, He 0.04 dpa and He 0.5 dpa, the binarization method can be used to investigate the amount of radiation damage under the four diffraction conditions. For these samples, the fraction of black pixels with respect to depth was determined from the binarized images. Fig. 5.20 shows exemplarily the depth profiles of the fraction of black pixels for the sample W 0.04 dpa under the four different diffraction conditions. It can be seen that the black to white profile is increasing from the surface with depth reaching its maximum at around 1.3 μm depth, which is in good agreement with the SRIM damage depth profile, Fig. 4.1. After the maximum it is decreasing. No dependence of the determined amount of damage with the set diffraction condition is found within the accuracy.

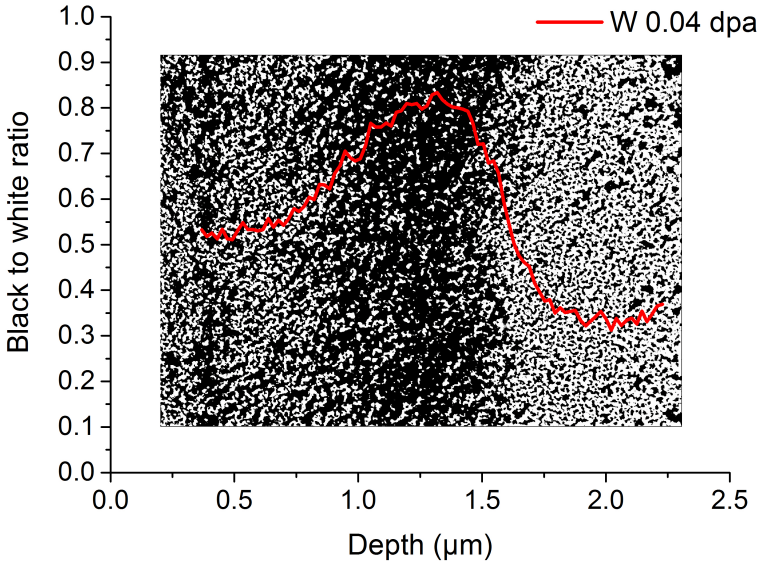

Fig. 5.21: Averaged depth profile of fraction of black pixels from the four depth profiles of the four diffraction conditions. The depth profile was smoothed by averaging over 20 pixel lines. The image in the background shows the binarized image from which the depth profile was determined.

For all samples (W 0.04 dpa, Si 0.04 dpa, He 0.04 dpa and He 0.5 dpa) investigated with this method, no difference in the amount of damage and the range of the damage zone were observed within the set diffraction conditions. Therefore, it can be stated that within the experimental accuracy the dislocation density is comparable for the investigated samples under the different diffraction conditions. As the depth profiles registered under the different diffraction conditions are nearly identical an average depth profile was determined from them. To smooth the depth profile curve 20 pixel lines were summarized giving for each sample depth profile curves, compare Fig. 5.21.

5.1.7 Discussion of the observations

The dislocation structures in the damage zones of self-damaged and silicone ion damaged tungsten were very similar in both damage levels of 0.04 dpa and 0.5 dpa. In the W 0.04 dpa and Si 0.04 dpa samples, small dislocation loops and dislocation loop clusters with high strain fields in between (black regions) were observed. No significant difference in the loop size was found with the set diffraction condition. The damage zones in the two samples were found to be comparable in the region of the damage peak maximum, as there the damage level is in both samples is comparable. The average loop size in the region of the damage peak maxima in W 0.04 dpa and Si 0.04 pda was 7.8±0.7 nm and 6.4±1.0 nm, respectively. Therefore, only a difference up to 20% was found for the loop size in Si 0.04 dpa with respect to W 0.04 dpa. However, when taking the uncertainty ranges into account the differences seem to be rather small. In the W 0.5 dpa and Si 0.5 dpa samples, a dislocation line network consisting of dislocation lines and dislocation loop chains was found. The dislocation line density was found to be independent from the set diffraction condition and was $(6.5\pm1)\cdot10^{14}\ \frac{m}{m^3}$ in the W 0.04 dpa sample and $(5.7\pm1)\cdot10^{14}\ \frac{m}{m^3}$ in the Si 0.5 dpa sample. The difference in the dislocation line density found in Si 0.5 dpa with respect to W 0.5 dpa is up to 12%. Therefore, only small differences were found in the damage zone of tungsten damaged by W and tungsten damaged by Si. The loop-to-line transition was found to take place in both samples at about 0.08 - 0.1 dpa. Due to different incident ion energies in the Si and W irradiations and different ion masses, significant differences are found in the primary recoil energy spectra, compare Tab. 4.1 and Fig. 4.2. The damage efficiency of incident Si ions compared to incident W ions is also different (about one third smaller), compare Tab. 4.2. In [160] the dependence of average damage rate and dislocation structure was studied. A difference in the average damage rates about a factor of 20 (ion beam scanned with 1kHz over the sample) resulted in only small differences in the dislocation structure, which were all within the uncertainty ranges. In our study, the beam was also scanned over the sample surface with 1 kHz, the average damage rates are listed in Tab. 4.2. The ion current during Si irradiations was higher than during W irradiations. The average damage rate obtained during Si irradiations is of a factor 1.5 higher as during W irradiation, compare Tab. 4.2. Hence, no differences in the dislocation structure due to different average damage rates are expected. Therefore only the differences in the recoil energy spectra of Si and W ions could influence the dislocation structure in this study. In spite of the large differences in the recoil energy spectra only small

differences were observed in the dislocation structure between tungsten irradiated by Si and self-damaged tungsten. From this it can be concluded that tungsten irradiated by other high mass ions will show a very similar dislocation structure, at least when using similar average damage rates. What can be expected from these results for the D retention? As the damage zone in terms of dislocations is very similar for tungsten irradiated by medium to high mass ions it can be expected that the D retention should be similar as well. By studying the D retention of such samples it can be estimated to what extent the dislocation structure may govern the D retention. The following calculations are only rough estimations. The damage zone of W 0.5 dpa visible in Fig. 5.2 consists mainly of dislocation lines up to 2 μm depth. The dislocation line density (Tab. 5.4) was determined by the line intersection method to be $(6.5\pm1)\cdot10^{14}\,\frac{m}{m^3}$. With this the possible D amount retained in the dislocation lines can be roughly estimated. Let assume that a D trap site can be found at every interatomic distance. The damage depth was found to be 2.6 μm from which up to 2 μm the dislocation line network is found. The volume of the damage zone governed by dislocation lines of a 1 cm^2 sample is hence $2.0\cdot10^8$ μm^3 (W 0.5 dpa). From this the total dislocation length is calculated. The total dislocation length is found to be $1.3\cdot10^{11}$ μm. Dividing the total length with the lattice constant of 0.316 nm of tungsten gives the total number of $5.4\cdot10^{14}$ possible trap sites/cm^2. As one vacancy site can trap up to 6 hydrogen atoms at room temperature [73] the number of trapped D in W 0.5 dpa can vary between $5.4\cdot10^{14}$ and $32.4\cdot10^{14}$ D atoms/cm^2 trapped in the dislocation lines up to 2 μm depth. Note please that this is only the lower limit as only good visible dislocation lines were counted to obtain the dislocation line density. The small dislocation loops and dots were not counted. They can also contribute to the D retention significantly.

The estimation of trapped D in W 0.04 dpa sample at dislocation loops is more difficult as the dislocation loop density could not be evaluated due to the high numbers of loops and black regions. To estimate the possible amount of D atoms retained in the dislocation structure in the W 0.04 dpa sample the following Gedankenexperiment is done: From TEM images of W 0.04 dpa it is known that dislocation loops of an average diameter of 7.8 nm are found all over the damage zone. To calculate the possible amount of D atoms/cm^2 trapped in the dislocation structure let us imagine a lamella of a thickness of 100 nm with a width of 1 cm and a depth of 2.3 μm equal to the depth of the damage zone. Say every 10 nm a dislocation loop of 7.8 nm diameter is found. This results in $2.3\cdot10^8$ loops in the lamella. 1 cm contains 10^5 layers of 100 nm thickness. Therefore, $2.3\cdot10^{13}$ dislocation loops per cm^2 are expected. One loop has a diameter of 7.8 nm. The dislocation loop circumference is then 24.5 nm.

At every interatomic distance a possible D trap site is located, which can eventually trap 1-6 D atoms [73], which results in about 78-468 D atoms trapped around such a dislocation loop. Having $2.3{\cdot}10^{13}$ dislocation loops per cm^2 results in about 1.80-$10.8{\cdot}10^{15}$ D atoms/cm^2. The above presented calculations should be seen as very rough estimation of the amount of D trapped by dislocations. The values are only a lower limit of the possible D amount trapped in dislocations and will be compared to the D retention found in self-damaged tungsten in Chap. 6.

The damage zone of tungsten damaged by light ions (H, D, He) up to 0.04 dpa is significantly different in comparison to that created by medium to high mass ion irradiation. In H 0.04 dpa, D 0.04 dpa and He 0.04 dpa samples three to four subzones in the damage zone are observed, while in the W 0.04 dpa and Si 0.04 dpa cases no subzones could be distinguished. Zone 1 might be an artifact introduced during preparation as such a zone up to 0.2 μm was observed at some not irradiated tungsten sample, when the protective deposited tungsten layer was sputtered away during lamella preparation. Zone 2 is nearly identical in all light ion irradiations. Zone 3 depends on the used ion species. In He 0.04 dpa small dislocation loops with high strain field are observed, whereas in D 0.04 dpa large dislocation loops and in H 0.04 dpa long disloaction lines are found. Zone 4 is assigned to the tail of the damage depth profile. There are several differences in the light ion irradiation compared to high mass ion irradiation. Firstly, light ion irradiation results in not dense collison cascades in contrast to high mass ion irradiations, where dense collision cascades are present [12]. Secondly, the recoil energy spectra resulting from the irradiation with light ions differs, see Fig. 4.2. This results in dramatically lower damage efficiencies than for medium to high mass ions , compare Tab. 4.2. Thirdly, due to technical reasons, a different ion current during the irradiations is obtained. Hence, the average damage rate (dpa/s) found in light ion irradiation is 1 - 2 orders of magnitude smaller. In [160] a difference in the dislocation structure of self-damaged tungsten was observed depending whether the beam was scanned over the sample or not. Therefore it can be concluded that large differences in the average damage rate can result in differences in the dislocation structure. On the other hand in the Si 0.04 dpa sample in the first 0.6 μm small dislocation loops and dislocation dots were found similar to the zone 2 found in the light ion irradiations. It was concluded that this is because of the significant differences in the damage depth profile. The damage level in Si 0.04 dpa in small depths is about 3 times lower than in W 0.04 dpa, Fig. 4.1. SRIM calculates similar damage depth profiles for H 0.04 dpa, D 0.04 dpa, He 0.04 dpa and Si 0.04 dpa. Despite this fact the dislocation structure

is significantly different, with distinct zones. It can be that SRIM calculates a too high damage level for H 0.04 dpa, D 0.04 dpa, He 0.04 dpa, which would explain the extended zone 2. Hence, it is not clear whether the subzones observed are due to differences in the primary recoil energy distribution or due to the significant lower damage rate or simply due to differences in the damage depth profile. To solve this problem further investigation are needed.

5.2 Open volume defects - Positron annihilation spectroscopy of tungsten samples

The polycrystalline W samples irradiated by H, D, He, Si, Fe, Cu, W were analyzed by positron annihilation lifetime spectroscopy with positrons of an incident energy of 16–18 keV. In Fig. 5.22, the lifetime spectra are shown. A significant difference in the slope is observed for the undamaged sample compared to the damaged samples. Between the damaged samples smaller differences in the lifetime spectra are observed. The largest differences among them are seen between light ions and medium to high mass ions. In the 0.5 dpa and 0.04 dpa case (Figs. 5.22a and 5.22b), it can be recognized that the lifetime spectra of tungsten damaged by high mass ions (Fe, Cu, W) are almost identical. The lifetime spectrum for tungsten damaged by Si lies in between. In the 0.04 dpa case (Fig. 5.22a), it can be recognized that the lifetime spectra of tungsten damaged by H, D, He are also almost identical.
The mean implantation depth for 18 keV positrons is about 0.2 μm and extends up to 0.6 μm, compare Fig. 3.8. Therefore, only a small part of the damaged zone is probed by the positrons. Additionally, the samples do not exhibit the same damage level in a depth of 0.2 μm. The W 0.5 dpa samples reaches a damage level of 0.25 dpa in 0.2 μm depth. The Si 0.5 dpa sample reaches a damage level of only 0.07 dpa in this depth, compare Fig. 4.1. Therefore, the question arises whether the small differences observed in the lifetime spectra are coming from differences in the defect structures or are due to the different damage levels in the sample. To answer this question, it was decided to irradiate tungsten with Si and Cu such that the same damage level of 0.01 dpa, 0.1 dpa and 0.5 dpa is reached in 0.2 μm depth and that the damage level is flat in the depth interval of 0.1-0.4μm. Cu and Si were chosen as in the lifetime spectra (Fig. 5.22) of tungsten damaged by Cu and Si small differences were observed. Tungsten was irradiated with 7.5 MeV Si ions and 9 MeV Cu ions which gives a relatively flat damage depth profile at the depth interval of 0.1-0.4 μm. Fig. 5.23 shows the obtained damage depth profiles for the 0.01 dpa and 0.1 dpa case. Fig. 5.24 shows the lifetime spectra obtained for the six different samples. In Fig. 5.24b, the undamaged tungsten sample is shown as reference as well. It can be observed how the slope changes with increasing damage level. This is observed for tungsten damaged by Si as well as for tungsten damaged by Cu. The observed change can be due to two different reasons. It can be that with a higher damage level the defect types produced are different or that due to different defect concentrations (higher defect concentration with higher damage level) the

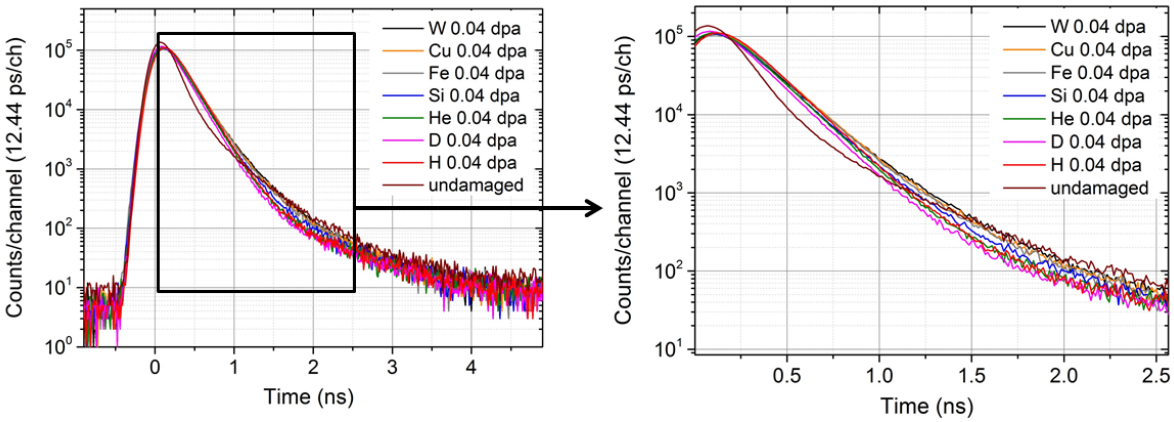

(a) Positron lifetime spectra for damaged tungsten up to 0.04 dpa in the damage peak maximum.

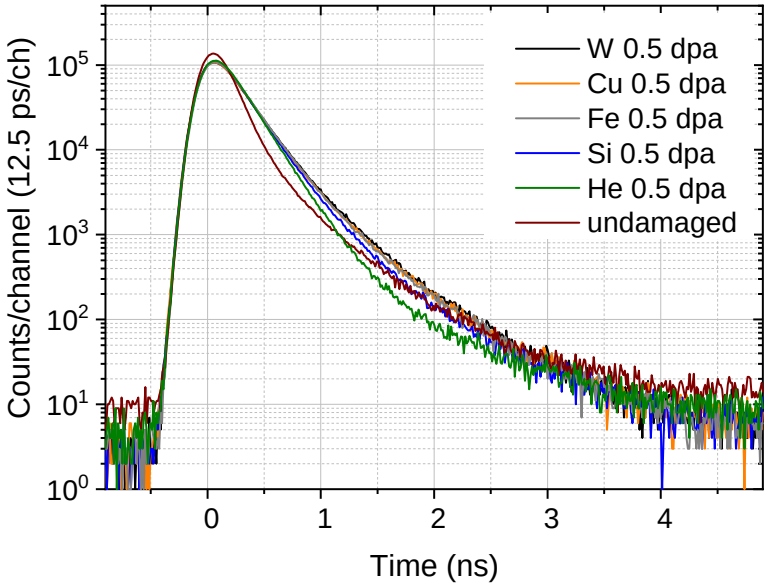

(b) Positron lifetime spectra for damaged tungsten up to 0.5 dpa in the damage peak maximum.

Fig. 5.22: Positron lifetime spectra at 18 keV positron incident energy for polycrystalline tungsten damaged by H, D, He, Si, Fe, Cu, W with energies specified in Tab. 4.1 up to 0.04 dpa (a) and 0.5 dpa (b) in the damage peak maximum.

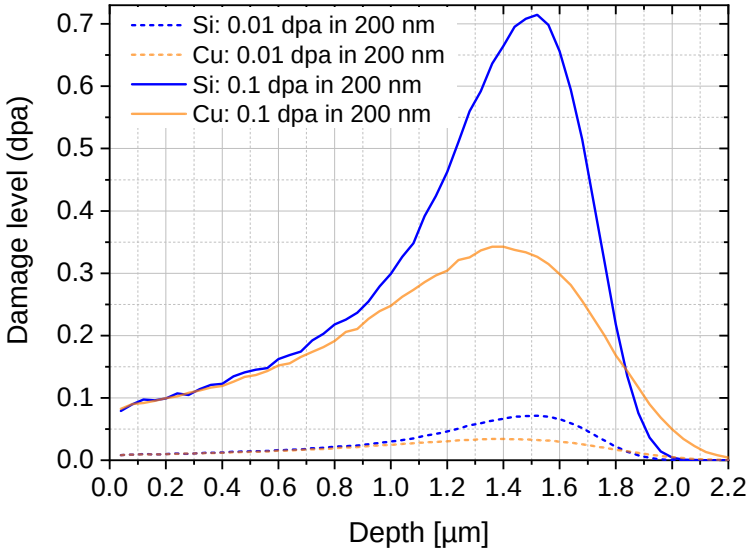

Fig. 5.23: SRIM damage depth profiles for tungsten irradiated by Si and Cu such to reach the damage level of 0.01 dpa or 0.1 dpa at 0.2μm depth.

distributions of the trapping of the positrons differ which leads to this observed differences in the spectra. Fig. 5.25 shows the lifetime spectra of tungsten damaged by Si and Cu up to different damage levels in 0.2μm depth in one figure. It can be seen that the lifetime spectra are identical at all three damage level. Therefore, it can be concluded that the difference observed in Fig. 5.22 between tungsten damaged by Cu and Si are due to the different damage levels in the positron probing depth and not due to the different defect structure. The measured PALS spectra were evaluated by PALSfit. They were fitted with three to four exponential functions corresponding to three to four lifetime components. The decomposition is sometimes difficult to interpret as it can be ambiguous due to the high sensitivity of the exponential fits to the noise in the data. The average lifetime is a more stable quantity to analyze. Tab. 5.5 shows the average lifetimes for the measured samples. It can be seen that the average lifetime is very similar for tungsten irradiated by Cu and tungsten irradiated by Si to the same damage level in 200 nm. This was expected as the lifetime spectra are also identical. It can be observed that the average lifetime is increasing with the damage level. That means that positrons live longer in more damaged tungsten. With higher damage level, the defect density is higher and this leads to less positrons annihilating from the defect free bulk and more positrons annihilating from the trapped state. The decomposition in four lifetimes is similar for all six samples but the intensities of the lifetimes vary. The decomposition of the

dpa in 0.2 μm	Si	Cu
0.01	201.8 ps	202.4 ps
0.1	225.8 ps	221.9 ps
0.5	234.1 ps	241.3 ps

Table 5.5: Average lifetimes determined by fitting four exponential functions to the liftime spectra.

lifetime spectra in four components show that most of the positron 69-88 % have a lifetime of 190 ps-220 ps which corresponds to trapping in mono-vacancies and di-vacancies in tungsten [129]. This shows that the differences observed in Fig. 5.24a and 5.24b between the different damage levels are not due to other defect types in the different damage levels but due to the different defect density and distribution in the different damage levels. In Fig. 5.22a and 5.22b the life time spectra of the samples irradiated by high mass ions show not much difference which is, therefore, a sign of a similar defect structure.
From this, it can be deduced that for tungsten irradiated by medium to high mass ions the open volume defect structure is similar.

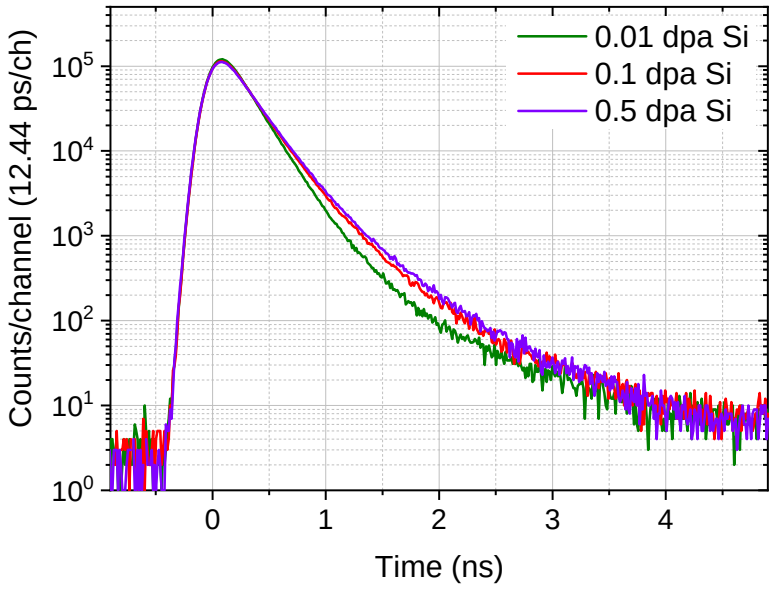

(a) Positron lifetime spectra for tungsten damaged by Si up to 0.01, 0.1, 0.5 dpa in 0.2 μm depth.

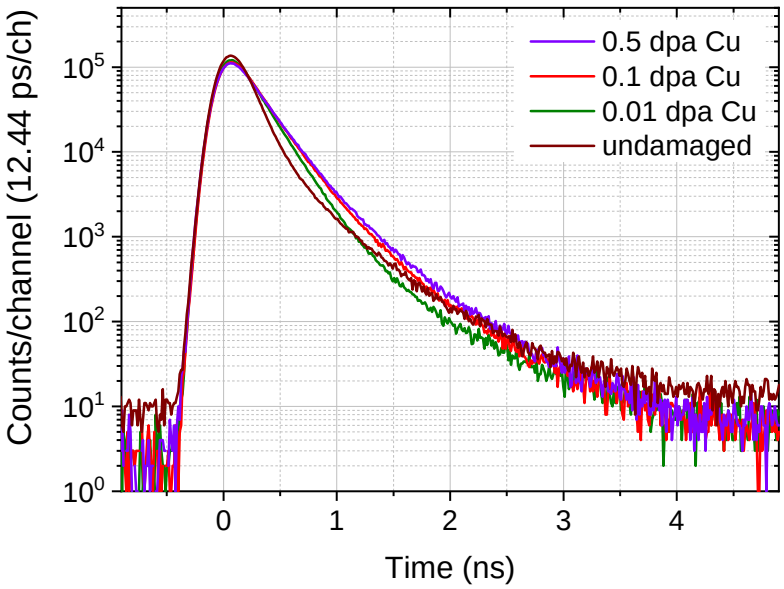

(b) Positron lifetime spectra for tungsten damaged by Cu up to 0.01, 0.1, 0.5 dpa in 0.2 μm depth. For comparison the lifetime spectrum of undamged tungsten is shown as well.

Fig. 5.24: Positron lifetime spectra for tunsten damaged by Cu and Si at different damage levels in 0.2 μm depth.

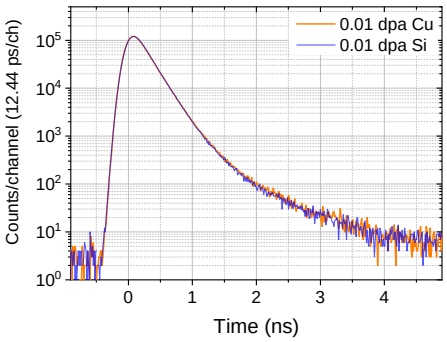

(a) Positron lifetime spectra for tungsten damaged by Si and Cu up to 0.01 dpa in 0.2 μm depth.

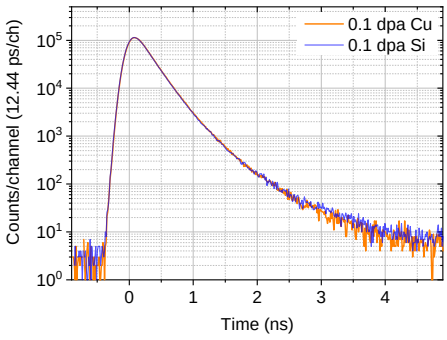

(b) Positron lifetime spectra for tungsten damaged by Si and Cu up to 0.1 dpa in 0.2 μm depth.

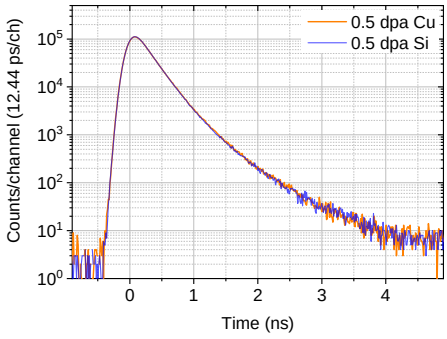

(c) Positron lifetime spectra for tungsten damaged by Si and Cu up to 0.5 dpa in 0.2 μm depth.

Fig. 5.25: Positron lifetime spectra for tunsten damaged by Cu and Si at different damage levels in 0.2 μm depth.

5.3 Chapter Summary

Tungsten was damaged by He, Si, W to a damage level of 0.04 dpa and 0.5 dpa and by H and D to 0.04 dpa. The damage zone of each sample was investigated with the TEM Jeol and partly with the STEM HD 2700. The damage zone was observed under four different diffraction conditions, namely: (- 200), (020), (- 110), (110). For obtaining the diffraction conditions, the samples were tilted to the zone axis [100] and then brought to the four two beam conditions at which the kinematical BF images were recorded. For all irradiations it was found that the depth of the damage zone is in good agreement with the SRIM calculated depth profiles, compare table 5.1. The observed damage peak maxima in the TEM images were also found at the depth predicted by SRIM.
The damage zone of tungsten irradiated by tungsten or silicon was investigated. As the damage depth profile of Si 0.04 dpa sample and W 0.04 dpa sample is different, the damage zone of these samples was compared in the depth of the damage peak maximum, as there the damage level is the same in both samples. It was found that the damage zone is very similar for Si 0.04 dpa and W 0.04 dpa at the same damage level. It consists of dislocation loops and black regions. It could be shown that the black regions are agglomerations of dislocation loops, i.e. dislocation loops clusters. The dislocation loop density and hence the black region density is directly related to the damage level. This is especially visible in the fraction of black pixels depth profiles obtained from the binarized images. They follow closely the SRIM damage depth profile. It was found that the dislocation loops are of the same size under the four diffraction conditions and in the whole damage zone. The average loop size in W 0.04 dpa was found to be 7.8±0.7 nm, while for Si 0.04 dpa it was found to be 6.4±1 nm.
The damage zones of the samples W 0.5 dpa and Si 0.5 dpa were also similar. In both samples a dislocation line network with only few dislocation loops and no black regions was found. The dislocation density was found to be independent from the set diffraction condition. For W 0.5 dpa, an average dislocation density of $(6.5\pm1)\cdot10^{14}\ \frac{1}{m^2}$ was found. For the Si 0.5 dpa sample a somewhat smaller dislocation density of $(5.7\pm1)\cdot10^{14}\ \frac{1}{m^2}$ was determined. At the end of the damage zone, a zone of dislocation loops and black regions was found in both samples which corresponds to the drop from 0.1 dpa to 0 dpa. Comparing the W 0.04 dpa, Si 0.04 dpa, and W 0.5 dpa, Si 0.5 dpa, it becomes clear that a rearrangement from small dislocation loops with high strain fields which started to agglomerate (0.04 dpa) to a dislocation line network with low strain fields took place. Comparing the images with the SRIM

damage depth profile, it was found that this rearrangement takes place at 0.08 dpa - 0.1 dpa. This shows that the irradiation of tungsten with 20 MeV tungsten ions or with 7.5 MeV silicon ions results in a very similar damage zone. Despite this large differences in ion mass and energies, only small differences in dislocation loop size and density were found. Therefore it is expected that irradiation with other different high mass ions like Cu or Fe would result in a very similar damage zone, even when using different energies.

The irradiation of tungsten with light ions (H, D, He) up to 0.04 dpa results in a very different damage zone. In the damage zone three to four distinct subzones are observed. The thicknesses of these four zones are ion dependent. Zone 1 is a zone of small dense dislocation loops with high strain fields, which possibly was introduced during preparation. Zone 2 follows with sparse small dislocation loops and dots. Zone 3 is found in the depth of the damage peak maximum. The appearance of this zone depends on the damaging ion species. In H 0.04 dpa, zone 3 consists of long dislocation lines. In D 0.04 dpa large dislocation loops of an average diameter of 15-22 nm are found. The long dislocation lines in H 0.04 dpa and the large dislocation loops in D 0.04 dpa were predominantly observed under the diffraction conditions (- 200), (020). This may indicate that their Burgers vector is of type $\langle 111 \rangle$. In He 0.04 dpa, zone 3 consists of small dislocation loops with very high strain fields. Because of this single loops are hardly visible in zone 3 of the He 0.04 dpa sample. After zone 3, a zone 4 similar to zone 2 is observed. This zone consists of sparse small dislocation loops and dots and corresponds to the drop to 0 dpa. Zone 4 was observed in D 0.04 dpa and He 0.04 dpa. It was not observed in H 0.04 dpa, probably due to the bad quality of this specific TEM lamella.

Tungsten was also irradiated with He up to 0.5 dpa. The whole damage zone in this sample consists of small dislocation loops which are hardly visible due to the high strain fields in between. The zone appears like a single, large black zone. It can be observed that the loops are arranging themselves in sort of lines but are not forming dislocation lines despite the high damage level. The observation with STEM HD 2700 showed that in this sample most probably He bubbles are present which might prevent the joining of the dislocation loops.

In TEM images, vacancies and small vacancy clusters were not observable due to limited image resolution. Therefore, the open volume defect structure of the damage zone was studied with Positron Annihilation Lifetime Spectroscopy (PALS) using 16 - 18 keV energetic positrons. In order to allow meaningful comparison, the damage level should be comparable in the positron implantation depth which is for an energy of 18 keV about 0.2 μm. Therefore, polycrystalline tungsten samples were irradiated

by Si and Cu to the same damage level of 0.01 dpa, 0.1 dpa and 0.5 dpa in this depth. No differences in the lifetimes between tungsten damaged by Cu or Si were found. Small differences were found in the average lifetime with the damage levels. It was concluded that these differences are not due to different defect types but due to varying defect densities and distributions in the damage zone. PALS was also performed on samples irradiated with different ions up to 0.04 dpa and 0.5 dpa in the damage peak maximum. Between the medium to high mass ions only small differences in the raw data were found, probably due to different damage levels in the positron implantation depth. Therefore, it can be concluded that for tungsten irradiated by medium to high mass ions, the open volume defect structure is very similar.

Chapter 6

D retention in tungsten irradiated by different ions

In this chapter, the results on the investigation on D retention in tungsten irradiated by different ions (H, D, He, Si, Fe, Cu, W) will be presented.
Polycrystalline tungsten samples were prepared and irradiated as described in Sect.3.1 and 3.2. The irradiation parameter are given in Chap. 4. After the irradiation, the samples were exposed to a low-temperature D plasma at PlaQ (Sect. 3.7).
Nuclear reaction analysis (NRA) and thermal desorption spectroscopy (TDS) were performed to study the D retention. The methods are described in Sect. 3.8 an 3.9, First, results on long-term D outgassing of self-damaged tungsten after D loading will be presented. In the next section, results on the D retention in tungsten irradiated by different ions will be presented.

6.1 Study of long-term D outgassing

As D retention in irradiated tungsten was studied, the effect of long-term D outgassing after D loading in such a sample was also investigated. For this, a specially prepared self-damaged tungsten sample with a damage level of 0.23 dpa in the damage peak maximum was D loaded in PlaQ at 370 K. Nuclear reaction analysis was conducted after the D loading after 1 day, 3 days, 7 days, 23 days, 80 days, 296 days, 536 days. Measurements with seven different ^{3}He energies ranging from 500 keV to 4.5 MeV were conducted in each case. Fig. 6.1 shows the integrated proton peak counts for all measured ^{3}He energies versus the days passed since the D loading. A clear drop of the number of counts is observed during the first week. The reduction of counts continues up to about 80 days after D loading. After this time, the outgassing effect continues only slowly and is within the determined error margin of 4%. After 1.5 years from the D loading the counts in the proton peak decreased by 6 % to 12 % depending on the incident energy. A measurement error of up to 4 % was determined for every measurement point. This error is due to three reasons: 1. the uncertainty of the homogeneity of the sample (determined in [113] to be up to 2%) 2. the uncertainties in the current measurement (estimated to be up to 3%) and 3. the counting statistics (the square root of the counts).
Having this effect in mind, it is important to perform the nuclear reaction analysis for D depth profiling always in a comparable time interval after D loading. Therefore, nuclear reaction analysis with D(^{3}He,p)α and thermal desorption spectroscopy were always conducted in the fourth week after the D loading.

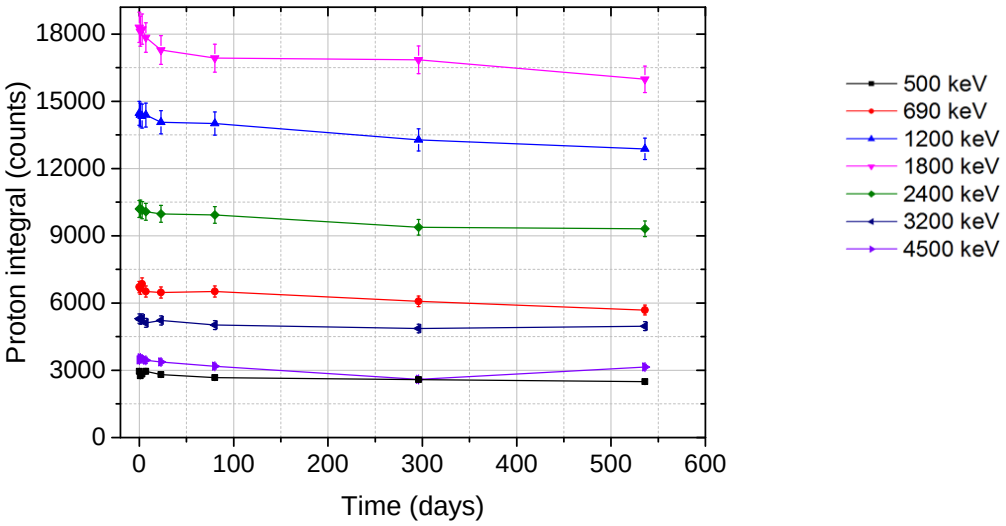

Fig. 6.1: Integral counts in the proton peak for different incident ^{3}He energies.

6.2 Results on D retention

As described in Ch. 4, D retention in self-damaged tungsten saturates at a damage level above 0.2 dpa [15]. Hence, samples in which the damage level exceeds locally the 0.2 dpa level will show local D saturation. Fig. 4.1 shows the damage depth profiles obtained from SRIM. Looking at the damage depth profile from W 0.5 dpa, one can recognize that throughout the whole damage zone the damage level is higher than 0.2 dpa. That means that the D retention will reach the maximum possible amount of D for certain D loading conditions, i.e. it will be saturated. For the samples Fe 0.5 dpa and Cu 0.5 dpa, the 0.2 dpa level is exceeded only in a depth of about 0.5 μm. Hence, local D saturation is only expected in the depth range from 0.5 μm to 1.9 μm. In Si 0.5 dpa and He 0.5 dpa sample, the 0.2 dpa level is exceeded between the depths of 1 μm and 1.8 μm. Hence, in this damage range, a local D retention saturation is expected. In the samples irradiated up to 0.04 dpa, no D retention saturation effect is expected as throughout the damage zone the damage level is smaller than 0.2 dpa. The local D retention in the 0.04 dpa samples should follow the damage depth profile.

Fig. 6.2 shows the total amounts of retained D for all damaged samples as measured by NRA and TDS. To obtain the total amount, the D depth profiles and the D desorption spectra were integrated. A good agreement within 10 % between the two measurements is found for all samples. The 0.5 dpa samples were irradiated such to reach the 0.5 dpa level in the damage peak maximum. Although the damage level

of 0.5 dpa to 0.04 dpa is more than ten times higher, the D retention is only up to three to four times higher as the 0.5 dpa samples are at least locally D saturated.
As the samples W 0.5 dpa, Cu 0.5 dpa and Fe 0.5 dpa are close to full D saturation they should retain a similar amount of D. This is indeed the case. It can be seen in Fig. 6.2 that the total amount of D retained in W 0.5 dpa, Cu 0.5 dpa and Fe 0.5 dpa is similar. The Si 0.5 dpa sample was expected to be only locally D saturated. Nevertheless, the total amount of retained D in Si 0.5 dpa sample is very similar to the samples W 0.5 dpa, Cu 0.5 dpa and Fe 0.5 dpa, therefore, it seems that the Si 0.5 dpa sample is also close to full D saturation. The total amount from He 0.5 dpa is significantly lower meaning that this sample is not fully saturated with D. This is in agreement with with anticipation, because in a large fraction of the damage zone the dpa value is significantly lower than 0.2 dpa.
All 0.04 dpa samples show a lower D retention. When looking at the total amount of D retained in the 0.04 dpa samples in Fig. 6.2, it seems that there can be a correlation between the D amount retained in the sample and the damaging ion species. The 0.04 dpa damage level is in the linear regime of D retention. That means that a higher local damage level leads to a higher local D retention. The local damage level in the damage peak was for all samples 0.04 dpa. The integrated damage over the full damage depth is different for the different samples, compare Figs. 6.3 and 4.1. Therefore, the raw data of the 0.04 dpa samples need to be normalized to the same integral damage to allow a meaningful comparison of the D retention.

Fig. 6.4 shows the measured D depth profiles determined by NRA together with the calculated SRIM damage profiles for all samples. The present version of NRADC allows to use only two different detectors. It was decided to use for the 0.5 dpa samples, the signals from the small proton detector at 135° and the α detector to have a very good depth resolution at the first 500 nm depth. In the 0.04 dpa samples, the D concentration was expected to be lower and because of that it was important to have a good count statistics. Therefore, the two available proton detectors at 135° were used. The D depth profiles are shown with their 3σ uncertainty determined by NRADC in the final Markov Chain Monte Carlo (MCMC) optimization. The D depth profiles of the 0.5 dpa samples show a higher D retention than the D depth profiles from the 0.04 dpa samples, as more trapping sites are available for D. For all measured samples, the SRIM damage range is comparable to the D retention depth. Hence, all present defects were decorated with D indicating that the D loading time in PlaQ was chosen long enough.

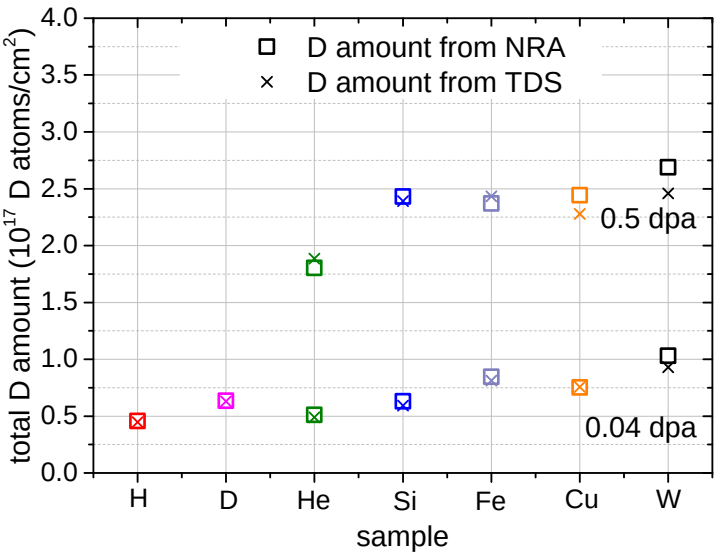

Fig. 6.2: Total amounts of D retained in tungsten measured by NRA and TDS for different damaging ions.

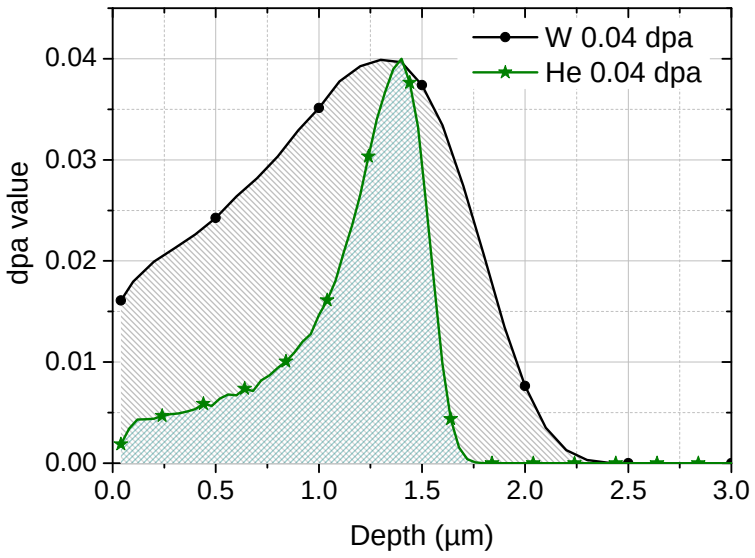

Fig. 6.3: Damage depth profiles calculated by SRIM for samples W 0.04 dpa and He 0.04 dpa. Both damage depth profiles reach the 0.04 dpa level in the damage peak maximum. Nevertheless, the damage depth profiles' integrals are significantly different. The integrated damage depth profile of W 0.04 dpa is twice as large as the damage integral of He 0.04 dpa.

total D amount in 10^{17} at./cm^2				
	0.5 dpa		0.04 dpa	
ion	NRA	TDS	NRA	TDS
W	2.69	2.46	1.03	0.93
Cu	2.44	2.28	0.75	0.76
Fe	2.37	2.43	0.85	0.81
Si	2.43	2.39	0.63	0.59
He	1.80	1.89	0.51	0.49
D			0.64	0.63
H			0.46	0.45 (1.01)

Table 6.1: Total D amount in 10^{17} at./cm^2 obtained by NRA and TDS for the 0.5 dpa and 0.04 dpa samples. The total D amount is equal to the total hydrogen amount retained in the samples except H 0.04 dpa sample. For H 0.04 dpa a significant amount of hydrogen as protium is retained. The total hydrogen amount is given in brackets and is derived from H_2, HD, D_2 signals.

First, the results of the irradiations up to 0.5 dpa will be discussed. The 0.2 dpa level above which D saturation is expected [15] is shown as a red line in Fig. 6.4. In Fig. 6.4a, it is visible that for self-damaged tungsten damaged up to 0.5 dpa (W 0.5 dpa sample) the damage level is higher than 0.2 dpa up to a depth of 1.8 μm. Therefore, the D depth profile of the W 0.5 dpa sample should be flat up to this depth, i.e. the maximum possible D amount is retained. The NRA D depth profile of W 0.5 dpa shows a D concentration of 1.8 at.% up to 1.4 μm and drops slightly to 1.6 at.% up to a depth of 2.2 μm. Taking into account the statistical uncertainties indicated by the uncertainty bands in the D depth profiles and the limited depth resolution of the used NRA method, it can be concluded that the W 0.5 dpa sample is saturated with D up to a depth of about 1.9 μm, as expected. Hence, full D saturation is reached. The Cu 0.5 dpa depth profile shown in Fig. 6.4b) is also almost flat. In the near surface layer up to a depth of 0.08 μm, the D concentration is only 1.3 at.%. Then it rises to 1.8 at.% in the maximum up to a depth of 2 μm. The Fe 0.5 dpa sample depth profile (Fig. 6.4 c) shows from the surface to 0.22 μm a D concentration of 1.6 at.%. A maximal D concentration of 1.8 at.% is reached between 0.22 μm and 2 μm. As for W 0.5 dpa, the D depth profiles of the Cu 0.5 dpa and Fe 0.5 dpa samples are almost flat and practically fully saturated with a maximum D concentration of 1.8 at.%. Comparing the D depth profiles with the calculated SRIM damage depth profiles in Fig. 6.4, it can be concluded that the maximum D retention value is reached already at around 0.13-0.15 dpa and not only above 0.2 dpa. From

Fig. 4.1, it is seen that the Si damage depth profile reaches 0.13-0.15 dpa at a depth of about 0.7 μm. Hence, it can be expected that Si 0.5 dpa sample will be locally D saturated in the depth range between 0.7 μm and 1.8 μm, i.e. it will be close to full D saturation. The measured D concentration profile for Si 0.5 dpa increases from 1.2 at.% at the surface through 1.7 at.% up to a concentration of 2.0 at.% (Fig. 6.4 d). Taking into account the uncertainties and remembering that the steps in the depth profiles are showing an average D concentration in a certain depth interval, it can be concluded that indeed saturation is reached locally between 0.6 μm and 2 μm.
The D depth profile of the He 0.5 dpa sample is shown in Fig. 6.4 e. This D depth profile is significantly different than those presented so far. The D concentration increases steeply from 0.9 at.% through 1.3 at.% up to 2.4 at.% at a depth of 0.8 μm and drops to 0.22 at.% at a depth of 1.5 μm up to a depth of 2.4μm. For all D depth profiles for 0.5 dpa, the D-filled range is in good agreement with the damage depth range predicted by SRIM. Damaging up to 0.5 dpa was not conducted with H and D ions due to the excessive required damaging fluences, see Tab. 4.1. Fig. 6.5 shows the D depth profiles for the samples damaged up to 0.5 dpa in one figure. When comparing the D depth profiles of W 0.5 dpa, Cu 0.5 dpa and Fe 0.5 dpa and taking into account their statistical uncertainties 3σ, it is obvious that they can be considered as being identical. D saturation is reached in the whole damage zone (beside the first 200 nm in Cu 0.5 dpa and Fe 0.5 dpa). Comparing with these, the Si 0.5 dpa D depth profile is only locally saturated with a somewhat higher D concentration in the D peak maximum.
The D depth profile of the He 0.5 dpa sample is significantly different. The D concentration in the damage peak in He 0.5 dpa sample is up to 30 % higher compared to the W 0.5 dpa sample. The accumulation of D in the He implantation region in tungsten was already reported by Markelj et al. [161]. It was shown that He attracts D and that the D retained increases in the presence of He. This can be explained by He clustering or He bubble presence in the sample. MD simulations show that a large amount of Hydrogen can be trapped around the He bubbles [162].

Figure 6.6 shows the D desorption spectra for the same set of samples shown in Fig. 6.5. All D desorption spectra consist of at least three peaks and start and end at identical temperatures. The first peak is located at about 490-500 K, the second one at about 590-600 K and the third one at about 770-780 K. In the samples W 0.5 dpa, Cu 0.5 dpa, Fe 0.5 dpa and Si 0.5 dpa, the two first peaks are difficult to distinguish as they both merged into one broad peak structure. The third peak is clearly separated. From NRA, it is known that W 0.5 dpa, Fe 0.5 dpa and Cu 0.5 dpa are fully D saturated. The D desorption spectra of these three samples

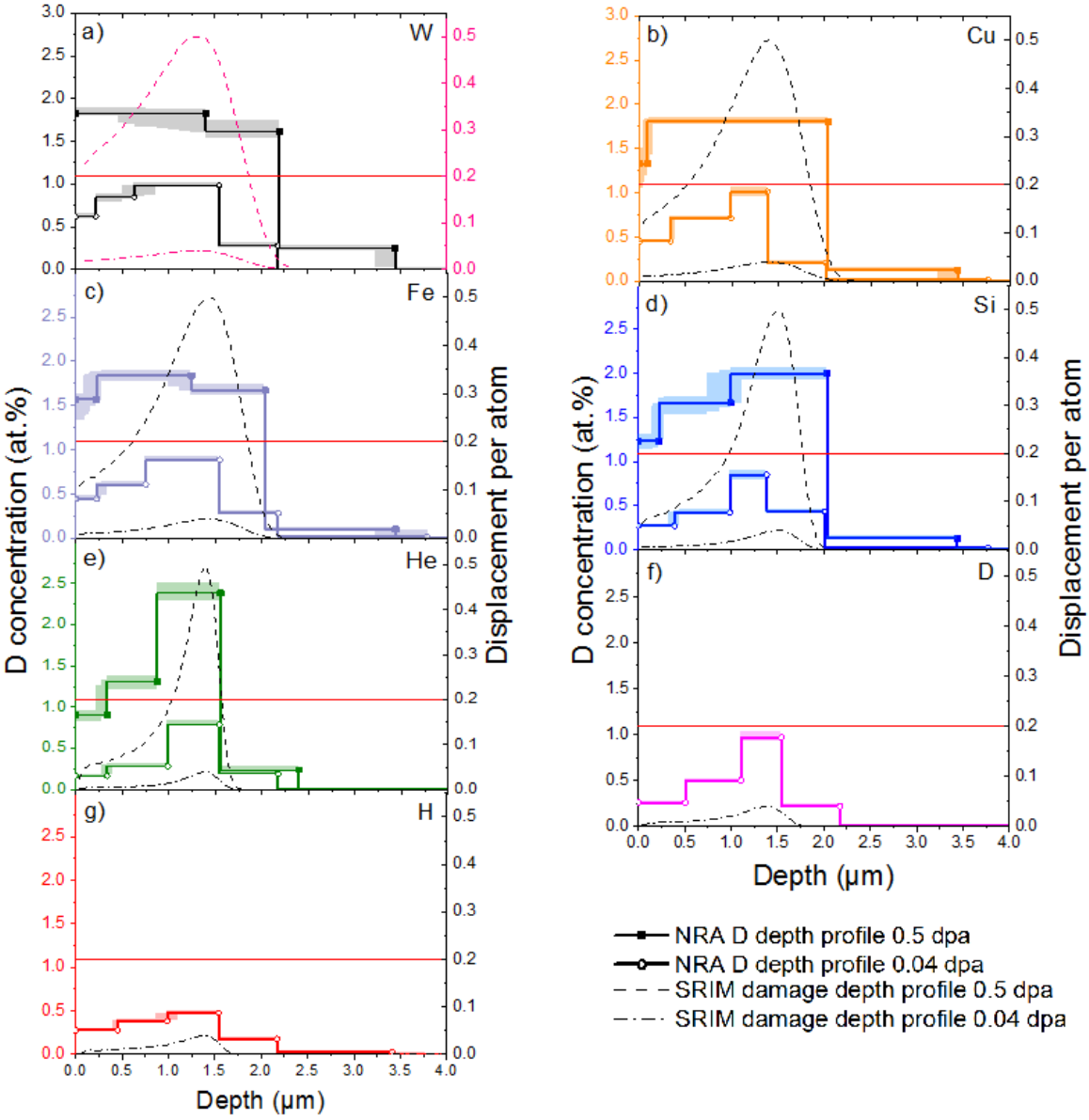

Fig. 6.4: D depth profiles measured by NRA (step profiles) and SRIM calculated damage depth profiles (dashed lines) shown for all samples damaged with different ions (W, Cu, Fe, Si, He, D, H) at 0.04 dpa and 0.5 dpa. The damaging ion is denoted in the figure. The red lines indicates the 0.2 dpa level at which D retention saturation is reached.

are identical. Only some small, not significant differences are discernible in the first broad peak structure. The third peak is identical. Si 0.5 dpa was found to be only locally D saturated in the depth range of 0.6 μm and 1.9 μm. Nevertheless, the D desorption spectrum of Si 0.5 dpa is very similar to the spectra of W 0.5 dpa, Cu 0.5 dpa, Fe 0.5 dpa. Therefore, it can be stated that Si 0.5 dpa is close to full D saturation. This allows the conclusion that the D retention is the same for medium to high mass ions in the 0.5 dpa case. In references [15, 16, 19, 85, 90], the peaks are assigned to represent D desorption from different defect types. The D desorption spectra of medium to high mass ions are nearly identical, i.e. the detrapping energies and intensities are nearly identical. With this, it can be assumed that the defect structure is similar as well.

The D desorption spectrum obtained from the He 0.5 dpa sample is significantly different. The D desorption spectrum shows three well distinguishable peaks. The first peak is found at about 470 K, the second peak is seen at around 610 K and the third at about 730 K. All three peaks in the D desorption spectrum of He 0.5 dpa are found at slightly different temperatures than for medium to high mass ion samples. The second peak in the He 0.5 dpa D desorption spectrum is highest. This significantly different D desorption spectrum suggests that also a different defect structure can be expected in tungsten damaged by He ions. The helium fluence during 1 MeV He irradiation of tungsten up to 0.5 dpa was $6.25{\cdot}10^{16}\,\frac{at}{cm^2}$. Using transmission electron microscopy, Miyamoto et al. [151] observed nm sized He bubbles in tungsten after an exposure to 50 eV Helium ions starting to be visible from a fluence of $5.0{\cdot}10^{16}\frac{at}{cm^2}$. Hashimoto et al. observed nanometric He bubbles in tungsten irradiated with 1.3 MeV He ions at 850°C at a fluence of $10^{15}\frac{at}{cm^2}$ and annealed at 2000°C [163]. Gilliam et al. [164] and Debelle et al. [165] found strong evidence from NRA studies for the existence of He bubbles in 1.3 MeV He implanted tungsten at fluences in the range of $10^{15} - 10^{18}\,\frac{at}{cm^2}$. Therefore, He bubbles can be expected in the He 0.5 dpa and He 0.04 dpa samples. These nm size bubbles which are supposed to act as additional trapping sites for D are probably the explanation for the significant change in the D retention behavior of tungsten [161, 162].

Let us now discuss the D retention in the 0.04 dpa samples. Fig. 6.4 shows also the D depth profiles for the samples damaged up to 0.04 dpa. The D depth profiles are not as flat as the D depth profiles from 0.5 dpa samples. This is well understandable as the maximum local damage level throughout the whole damage zone stays well below the damage saturation level of 0.13 - 0.15 dpa (see discussion above). For all samples, the D retention range and the position of the maximum of the D retention are in reasonable agreement with the SRIM predictions, compare Figs. 6.4a-6.4b.

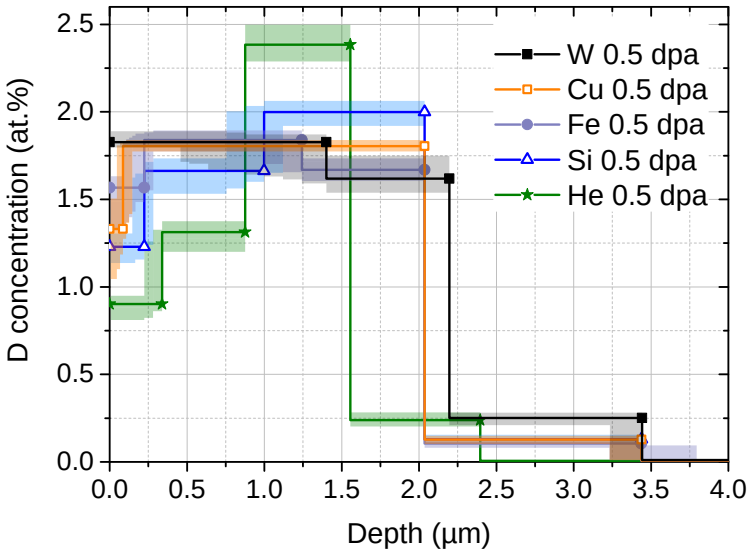

Fig. 6.5: D depth profiles in tungsten irradiated by low to high mass ions (He, Si, Fe, Cu, W) for 0.5 dpa. The uncertainty bands indicate the 3σ uncertainty.

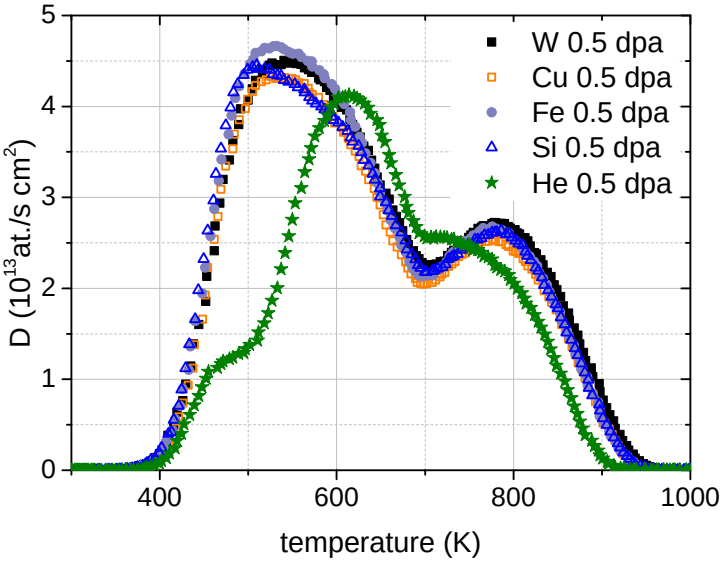

Fig. 6.6: D desorption spectra of tungsten irradiated by low to high mass ions (He, Si, Fe, Cu, W) up to 0.5 dpa.

However, for Si 0.04 dpa, Fe 0.04 dpa and Cu 0.04 dpa, the maximum in the NRA depth profiles is located at slightly smaller depths than predicted by SRIM, Fig. 6.4 b, c, d. As expected from the SRIM damage depth profile the D depth profile of W 0.04 dpa shows the broadest maximum compared with the other D depth profiles (Fig. 6.4a)). Fig. 6.7 and 6.8 show the D depth profiles for tungsten damaged by high mass and medium to low mass ions respectively. Fig. 6.8 shows also the measured D depth profile of the D 0.04 dpa before D loading in PlaQ. For an easier comparison between the two figures, the D depth profile of Si 0.04 dpa is plotted in both. Clear differences in the D depth profiles are observed. Nevertheless, all samples, except H 0.04 dpa, reach a D concentration in the peak of about 0.8 - 1 at.%. Within the 3σ uncertainty, shown as uncertainty band in Fig. 6.7 and 6.8, the D concentration in the peak can be seen as similar. From SRIM, a similar D concentration in the damage peak maximum is expected. The H 0.04 dpa shows a significantly lower D retention and will be discussed later. The differences observed in the D depth profiles seem to be a little arbitrary. Especially, the peak position in the NRA profiles of Fe 0.04 dpa, Cu 0.04 dpa and Si 0.04 dpa seems to be shifted to smaller depths. Therefore, a consideration of the uncertainties of the NRADC calculation is needed. One reason for the observed differences are the inherent uncertainties of the depth profiles themselves. The uncertainty of the atomic fraction of D in a certain layer system is determined by NRADC [139] in the final MCMC optimization and is shown as 3σ uncertainty band in the depth profiles. But in addition, uncertainty arises due to the selection of the step widths in the D depth profiles in the NRADC evaluation process. Each step represents the average D concentration within this depth intervall. When calculating the most probable layer system, describing the measured raw data, NRADC takes into account the depth resolution. The achievable depth resolution from the two proton detectors at 135 ° is in a depth of 1.5 to 2 μm only of about 0.4 μm to 0.6 μm, as calculated by ResolNRA [140]. In the depth of 1.5 - 2 μm, the damage peak and the sharp drop from the damage peak to zero is found, compare Fig. 4.1 and possibly the depth resolution is not enough to resolve the D depth profile correctly. To check this, the depth profile of Si 0.04 dpa was recalculated using a slightly different depth resolution. The difference was of about $\pm$ 50 nm. Fig. 6.9 shows the obtained D depth profile and to compare the D depth profile as shown in Fig. 6.7. It can be seen that the binning in the depth profile changed significantly. The depth resolution is, hence, not sufficient to correctly resolve the damage peak and the tail of the damage depth profile. This can be the reason for the differences observed in the evaluated D depth profiles. Hence, for the 0.04 dpa case the detailed form of the D depth profiles is rather uncertain. To

D-atoms per displacement

ion	NRA	TDS
W	0.296	0.267
Cu	0.253	0.254
Fe	0.296	0.284
Si	0.303	0.286
He	0.343	0.329
D	0.333	0.330
H	0.239	0.233 (0.527)

Table 6.2: Total D amount per displacement obtained by NRA and TDS for the 0.04 dpa samples. For H 0.04 dpa a significant amount of hydrogen is retained as protium. The complete H amount per displacement is given in brackets and is derived from TDS from H_2, HD, D_2 signals. For the other samples the total hydrogen amount is equal the D amount.

get a better depth resolution, a detector at higher scattering angle should be used as described in [166], [167]. Unfortunately, the detector at 175° was unavailable at the time of the measurements. The most robust quantity obtained from the depth profiles is the total D amount retained in the sample. This value can be calculated by integrating the evaluated depth profiles.

The 0.04 dpa damage level represents the linear regime in the D retention behavior, i.e. a higher damage level results in a higher D retention [15]. The integral damage level between the different ions is not equal, see Figs. 4.1 and 6.3. For comparing the D amount in samples with different integral damage levels, the most robust parameter is the number of trapped D atoms per displacement. The NRA D depth profiles and TDS spectra were integrated yielding the total trapped D amount, the integral damage was obtained by integrating the SRIM damage profile. The obtained total D amount was divided with the damage integral giving the number of D atoms per displacement as described in Eq. 6.1.

$$\frac{D\ integral\ obtained\ from\ NRA\ or\ TDS}{integrated\ SRIM\ damage\ depth\ profile} = \frac{Number\ of\ D\ atoms}{Number\ of\ displacements} \tag{6.1}$$

The number of D atoms per displacement found in the different samples is listed in Tab. 6.2. For medium to heavy ion irradiation, the variation in the total D amount retained per displacement is below 20%. The D 0.04 dpa and He 0.04 dpa sample retained most of D per displacement.

Figs. 6.10 and 6.11 show the normalized D desorption spectra from the 0.04 dpa samples. As the 0.04 dpa level is in the linear regime, the TDS spectra were

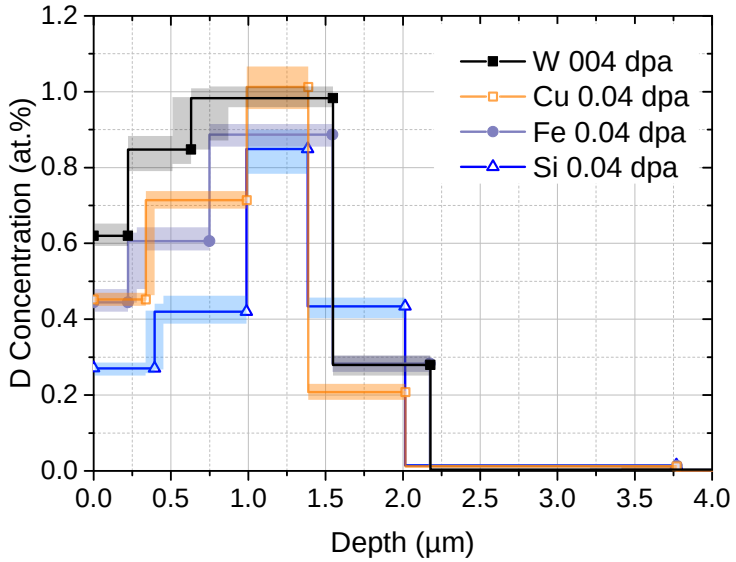

Fig. 6.7: D depth profiles in tungsten irradiated by medium to high mass ions (Si, Fe, Cu, W) for 0.04 dpa. The uncertainty bands indicate the 3σ uncertainty.

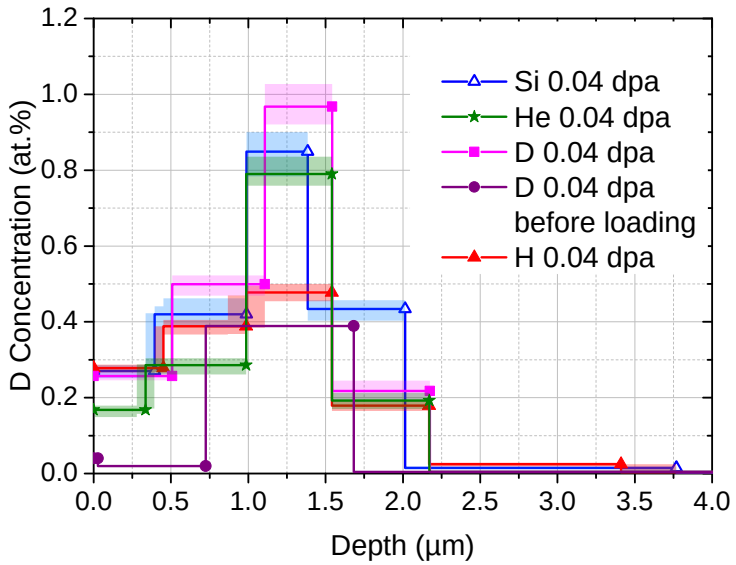

Fig. 6.8: D depth profiles in tungsten irradiated by low to medium mass ions (H, D, He, Si) for 0.04 dpa. The uncertainty bands indicate the 3σ uncertainty.

normalized by dividing with the damage integral obtained from SRIM damage depth profiles, (compare Fig. 6.3, Eq. 6.1). As in the 0.5 dpa case, all 0.04 dpa desorption spectra start and end at the same temperature and show three desorption peaks. The first two peaks are not clearly distinguishable giving a broad peak structure. The three peaks are located at temperatures of about 480-500 K, 580-600 K and 760-770 K, respectively. The first two peaks appear at comparable temperatures as for the 0.5 dpa samples. The third peak apears at somewhat lower temperatures. Fig. 6.10 shows the normalized TDS spectra from tungsten damaged by the medium mass to high mass ions. The D desorption spectra are very similar for all four ion irradiations. Hence, the D retention in tungsten damaged by medium mass to high mass ions is similar for the 0.04 dpa case. Small differences are observed in the first broad peak structure. The heights of the broad peak structure are different within 20 % which indicates different peak intensities of the first and second peak.
Fig. 6.11 shows the normalized D desorption spectra obtained from the irradiation with light ions up to 0.04 dpa. For better comparison with Fig. 6.10, the Si 0.04 dpa spectrum is also plotted. It becomes clear that the D retention in tungsten damaged by light ions is significantly different than for the medium to high mass ions. Especially, in the broad peak structure of the overlapping peaks 1 and 2 significant differences are observed. On the countrary, the third peak in the desorption spectra is for all 0.04 dpa samples, beside H 0.04 dpa very similar. The sample H 0.04 dpa shows a peak at the same position but with significantly lower intensity. He 0.04 dpa and D 0.04 dpa show a higher first peak. The number of D atoms per displacement found in He 0.04 dpa sample and D 0.04 dpa sample compared with W 0.04 dpa sample is 24 % higher, compare Tab. 6.2. The higher D retention in the He 0.04 dpa sample can be explained with enhanced hydrogen isotope retention in the helium implantation zone as for the He 0.5 dpa sample.
The D desorption spectrum from sample D 0.04 dpa is higher as more D was in the sample due to the preceding D implantation (during damaging with D, as can be seen in the depth profile of Fig. 6.8). The H 0.04 dpa sample shows a lower D desorption spectrum than all other spectra in Fig. 6.8. This is in good agreement with the NRA depth profile of H 0.04 dpa which also shows lower D retention compared with D 0.04 dpa.

However, Fig. 6.11 shows only the D desorption spectra derived from HD and D_2. As tungsten was in this case damaged with protons the full hydrogen isotope desorption spectrum including protium must be considered. Fig. 6.12 shows the complete hydrogen isotope desorption spectrum of H and D, derived from H_2, HD, D_2, for H 0.04 dpa sample. In addition to the total number of released H isotopes, the

individual contributions of H_2, HD, D_2 are also shown. For this sample the H_2 signal and HD signal are clearly not negligible. In the complete hydrogen isotope desorption spectrum, the second peak is dominant. In total, the contribution of protium to the total hydrogen release is about 56 % in this sample. In Fig. 6.13, the hydrogen isotope desorption spectrum for D 0.04 dpa sample is shown in the same way. The magenta curve shows the full hydrogen isotope desorption spectrum of D 0.04 dpa which is identical to the D desorption spectrum already shown in Fig. 6.11. For this sample the protium signal can be neglected. The H_2 signal is practically invisible and the HD signal is very low. Also for all other investigated samples in this study, the contribution of protium from H_2 and HD to the total hydrogen isotope release was negligible. The fact that the H_2 and HD signals are so strong in H 0.04 dpa indicates that the implanted protium got trapped in the created defects. Apparently the D fluence during loading was not enough for isotope exchange. The significant higher H amount per displacement found in H 0.04 dpa (compare Tab. 6.2 can be explained by defect stabilization observed by Markelj et al. [168]. The effect is not observed in the D 0.04 dpa. Note please that the fluence during irradiation almost three times lower, compare Tab. 4.1. Summarizing the tungsten samples irradiated by medium (Si) to high mass ions (Fe, Cu, W) to 0.04 dpa show a comparable D retention. Tungsten irradiated by light ions (H, D, He) up to 0.04 dpa shows a significant different D retention behavior.

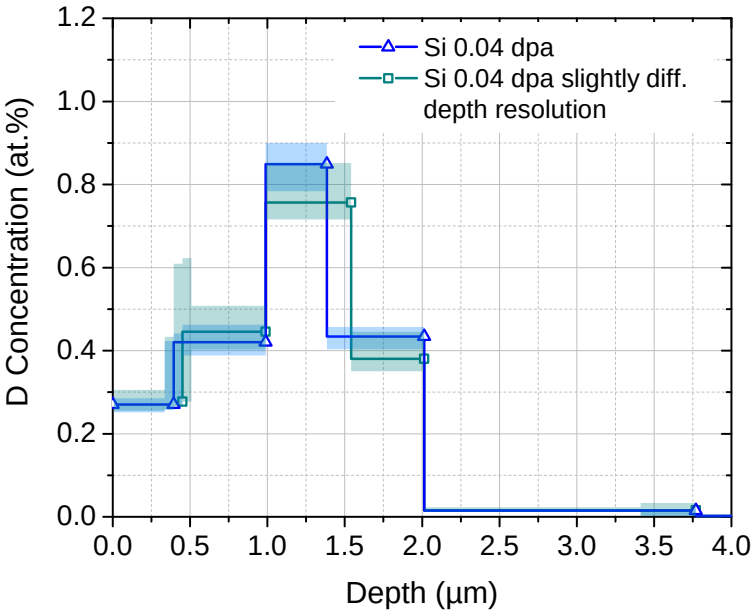

Fig. 6.9: D depth profiles of Si 0.04 dpa samples calculated with slightly different depth resolutions. The uncertainty bands indicate the 3σ uncertainty.

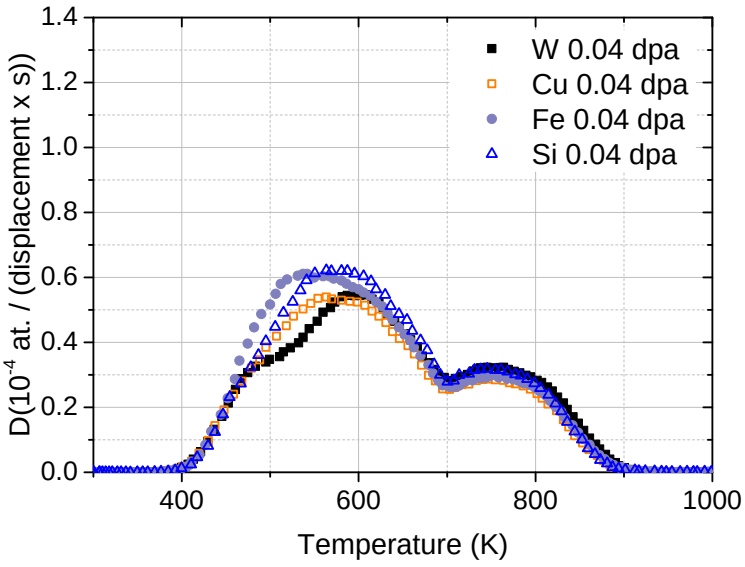

Fig. 6.10: Normalized D desorption spectra from tungsten irradiated by medium to high mass ions (Si, Fe, Cu, W) for 0.04 dpa, normalized by the integral damage.

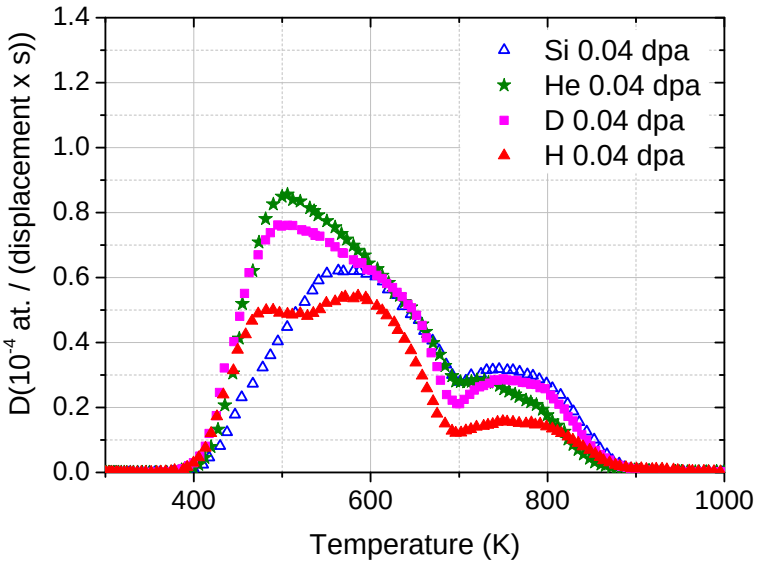

Fig. 6.11: Normalized D desorption spectra of tungsten irradiated by low to medium mass ions (H, D, He, Si) for 0.04 dpa, normalized by the integral damage.

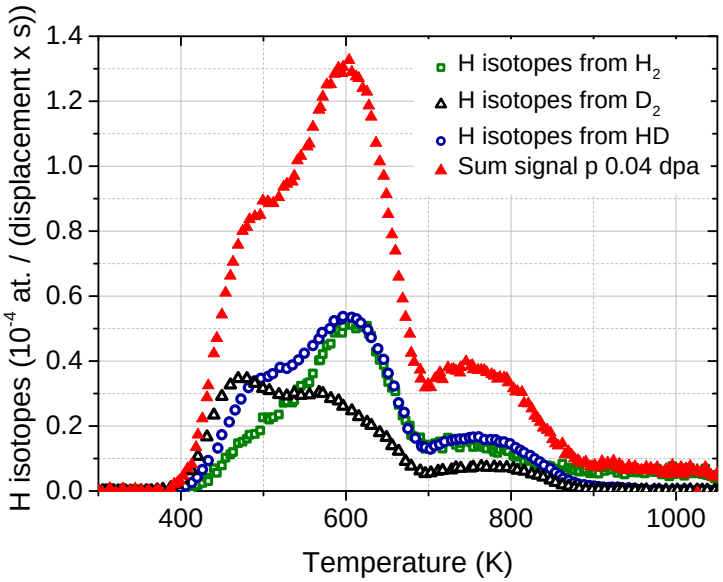

Fig. 6.12: Normalized complete hydrogen isotope desorption spectra (red) for sample H 0.04 dpa obtained from H and D signal from H_2, HD, D_2. Additionally the components of this signal: the signals from H_2, HD, D_2 are shown.

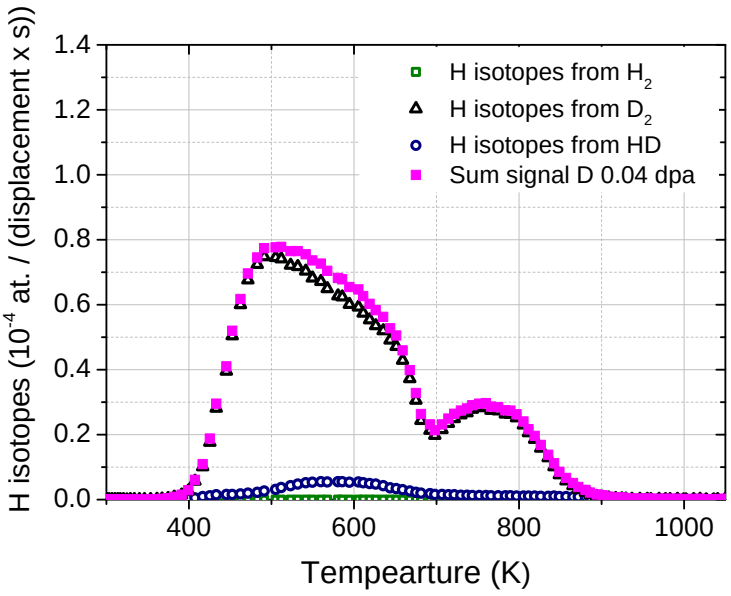

Fig. 6.13: Normalized complete hydrogen isotope desorption spectra (magenta) for sample D 0.04 dpa obtained from H and D signal from H_2, HD, D_2. Additionally the components of this signal: the signals from H_2, HD, D_2 are shown.

6.3 D retention and dislocation structure

The D retention is found to be nearly identical for tungsten damaged by medium to high mass ion up to 0.5 dpa and similar for tungsten damaged by medium to high mass ions up to 0.04 dpa. The dislocation structure was found to be very similar for tungsten damaged by medium to high mass ions as well. On the other hand, clear differences are seen in the D retention of tungsten damaged by light ions, especially the first peak in the D desorption spectrum of He 0.04 dpa and D 0.04 dpa shows a higher intensity. This first peak was assigned by Ogorodnikova et al. [16] to be D desorption from D trapped at dislocations and grain boundaries. Indeed the dislocation structure in these samples is also different. Four distinct zones with different dislocation densities are observed in the TEM images. According to the assignment of Ogorodnikova et al. [16], an higher intensity of the first peak would indicate a higher dislocation density in these samples. This was not observed in the TEM analysis. The author distances herself from assigning distinct desorption peaks to different defect types. It is difficult to relate the D retention peaks directly to the dislocation structure. For the W 0.5 dpa sample, the D amount retained at the visible dislocation line structure up to 2 μm was roughly estimated to be between (5.4 - 32.4)$\cdot 10^{14}$ D atoms/cm^2. From the NRA depth profile in Fig. 6.5 it is seen that 84% of the trapped D amount is trapped in the first 2 μm. 84% of the total amount are 2.26$\cdot 10^{17}$ D atoms/cm^2 obtained from the NRA depth profile or 2.07$\cdot 10^{17}$ D atoms/cm^2 derived from the TDS desorption spectra. The D retention at the observed dislocation lines would explain only 1.5% of the total D retention in the W 0.5 dpa sample. Note please that this is only a lower limit as small dislocation loops were not counted. The number of D retained at dislocation loops obtained for the W 0.04 dpa sample in the Gedankenexperiment was 1.8 - 10.8$\cdot 10^{15}$ D atoms/cm^2. The total D amount in W 0.04 dpa sample was between 0.93 - 1.03$\cdot 10^{17}$ D atoms/cm^2. Therefore the value obtained from the rough estimation could explain up to 12% of the total D amount retained in the sample. On the other hand, density functional theory (DFT) calculations in [92] predict that hydrogen retained at dislocations have low binding energies of 0.57 eV at screw dislocations and 0.89 eV at edge dislocations. From this, Bakaev et al. [92] estimates the H detrapping temperature to be between 320 K - 350 K for screw dislocations and 440 - 470 K for edge dislocation. Therefore, at least the fraction of D trapped by screw dislocations is already detrapped at 370 K. On the other hand, calculations in [169] show that the H retained at dislocations depends on the H concentration in the bulk and can be also significant at temperatures higher than room temperature. Hence, quantitative

conclusions about the D retention from dislocations by analysing the TEM images and the D retention data are not possible. The TEM images show the overall appearance of the damage zone and its dislocation structure. Vacancies, interstitials, vacancy and interstitial clusters, which influence the D retention, are not observed in the TEM images due to limited resolution. These objects together with the dislocations form the damage zone microstructure which governs the observed D retention. At present it is not clear to what extend the dislocations directly influence the D retention, but the observations suggests that some aspects of the dislocation structure seem to relate to the D retention. The dislocation structure of the damage zone of tungsten irradiated by Si and W is very similar. The D retention found in the samples damaged by Si and W is also comparable. The damage zone observed in tungsten after light ion irradiation is significantly different and so is the D retention. The loop-to-line transition is observed at 0.08 dpa - 0.1 dpa and it seems to correlate to the onset of the D saturation damaged tungsten.

6.4 Chapter summary

In this chapter the D retention in tungsten irradiated by different ions, (H, D, He, Si, Fe, Cu, W) with energies between 0.3 and 20 MeV up to damage levels of 0.04 dpa and 0.5 dpa in the damage peak maximum, was compared systematically. To study D retention in the created radiation defects, the samples were exposed to a low-temperature D plasma at 370 K, in order to decorate the produced trap sites. The D retention was studied by nuclear reaction analysis (NRA) using the D(^{3}He, p)α reaction and by thermal desorption spectroscopy (TDS).
Tungsten damaged by medium to high mass ions (Si, Cu, Fe, W) shows very similar D depth profiles and nearly identical deuterium desorption spectra in the 0.5 dpa case. Hence, the D retention in tungsten can be considered identical between medium mass to high mass ions in the 0.5 dpa case, which represents the saturation regime. Tungsten irradiated by helium up to 0.5 dpa shows a significantly different D retention: The D depth profile obtained by NRA is more peaked and a higher D concentration is reached in the damage peak maximum. The D desorption spectrum of tungsten irradiated by He up to 0.5 dpa shows three, well distinguishable peaks. The peaks have different intensities with slightly different temperatures as tungsten irradiated by medium to high mass ions. No D saturation effect in this sample was observed. This different D retention behavior is probably due to He bubble formation, which serves as additional trapping sites for D.

In the 0.04 dpa case more differences were observed. The 0.04 dpa damage level represents the linear regime in the D retention behavior of tungsten. In this regime more damage results in a higher D retention. The samples were irradiated with one energy for each ion species to have 0.04 dpa in the damage peak at around 1.5 μm depth. Therefore, the integral damage over the whole damage depth was different for the different ions. As a consequence, the D retention had to be normalized by the integral damage to allow a meaningful comparison. The differences in the normalized total amounts of retained D obtained from the D depth profiles and desorption spectra are below 18% for medium mass to heavy ion irradiations (Si, Cu, Fe, W). The normalized D desorption spectra are similar for Si, Cu, Fe, W irradiations, beside small differences in the broad desorption peak structure. The heights of the broad peak structure consisting of the first two desorption peaks differ by less than 20%. The third desorption peak is nearly identical. Therefore, it can be stated that the D retention in tungsten irradiated by medium to high mass ions at 0.04 dpa is similar. For tungsten irradiated by low mass ions (H, D, He) larger differences in the D retention were found. The broad peak structure consisting of the first two peaks is significantly higher. The third peak was very similar in all irradiations. The D desorption spectra are showing significantly different shapes. This suggests a defect structure different from that of the medium to high mass ions.

Chapter 7

Conclusions and Outlook

7.1 Conclusions

In this work, the radiation damage and the subsequent D retention in tungsten irradiated by different ions was studied. Tungsten was irradiated by He, Si, Fe, Cu, W to two damage levels of 0.04 dpa and 0.5 dpa and by H and D to 0.04 dpa in the damage peak maximum with different incident ion energies (0.3-20 MeV). The dislocation microstructure was investigated by transmission electron microscopy (TEM) and the open-volume defects were investigated by positron annihilation lifetime spectroscopy (PALS). D retention in the different irradiated tungsten samples was measured by nuclear reaction analysis (NRA) using D(^{3}He,p)α and thermal desorption spectroscopy (TDS). It was found that the observed depth of the damage zone as identified by TEM is in good agreement with the depth of the damage depth profile calculated by SRIM. Furthermore, the measured D retention depths in all samples agree well with the depth of the calculated damage depth profiles. In the 0.04 dpa samples, the observed damage peak maximum and the maximum in the D depth profiles are also found at the depth predicted by SRIM. Hence, SRIM predicts correctly the damage zone in tungsten for all used ions and a direct comparison from the damage zone and D retention with the SRIM damage depth profile is possible. The observed damage zones of tungsten irradiated by the medium mass ion Si and high mass ion W are very similar at comparable damage levels. In the 0.04 dpa samples dislocation loops and dislocation loop clusters are found. In the 0.5 dpa case a dislocation line network consisting of dislocation lines and dislocation loop chains, with only few isolated dislocation loops is found. By comparison of the observed damage zone with the SRIM damage depth profiles, it was found that a

rearrangement from dislocation loops to lines took place at about 0.08 dpa - 0.1 dpa. As very different energies, which result in different recoil energy spectra, were used, it can be concluded that irradiation with other different high mass ions, like Cu or Fe, would result in a very similar damage zone.
The investigation of open volume defects with PALS showed that for tungsten irradiated by medium to high mass ions, the open volume defect structure is also very similar.
It was shown that the D retention in tungsten irradiated by medium to high mass ions can be considered as identical in the 0.5 dpa case, which represents the saturation regime. In the 0.04 dpa case, only small differences of up to 20% in the D retention in tungsten irradiated by medium to high mass ions were observed. From comparison of the D depth profiles at 0.5 dpa and the SRIM damage profiles, it was shown that the D saturation is reached already at 0.13 - 0.15 dpa. The rearrangement from dislocation loops to lines was observed at slightly lower values of 0.08 - 0.1 dpa.
The dislocation structure of tungsten irradiated by light ions (H, D, He) is significantly different. In the 0.04 dpa case the damage zone consists of three to four subzones with different thicknesses. The appearance of the zones found at the depth of the damage peak depends on the used ion species. The D retention in tungsten irradiated by light ions was also found to be significantly different. Most differences are found in the D desorption spectra in the broad peak structure comprising of the first two desorption peaks.
This work can not answer the question whether dislocations contribute to the D retention or not and if yes how much. The comparison of the dislocation structure with the D retention suggests a correlation between them. The dislocation structure and open volume defect structure of tungsten irradiated by medium to high mass ions is very similar and so does the D retention. The dislocation structure of the damage zone in tungsten irradiated by light ions shows significant differences and so does the D retention. It is widely accepted that the microstructure governs the D retention. The microstructure of the damage zone in tungsten consists of vacancies, vacancy and interstitial clusters and dislocations. As single interstitials are mobile in tungsten at room temperature, they have migrated to sinks, like the surface, grain bounderies or dislocations, and are negligible. From the microstructure only the dislocation structure was observed by TEM as vacancies and small vacany clusters are not detectable by TEM. The dislocation loops and lines are related to the vacancies and interstitials as dislocations are formed by them. Therefore, some aspect of the appearance of the dislocation structure may relate to the D retention. D saturation was observed at 0.13 - 0.15 dpa, just after the dislocation loop-line

transition at 0.08 dpa - 0.1 dpa. It seems that at 0.08 dpa - 0.1 dpa the microstructure of the damage zone changes, which is observed in the loop-to-line transition and in the subsequent D saturation. In tungsten irradiated by He no D saturation and no loop to line transition took place. It seems that the loop to line transition is related to the onset of the D saturation in tungsten.

Since D retention in tungsten irradiated by medium to high mass ions (Si, Fe, Cu, W) is nearly identical for 0.5 dpa and similar for 0.04 dpa, the results presented here are especially useful for comparing of D retention data of tungsten irradiated by different ions. At damage levels high enough for D retention saturation (>0.2 dpa, data from different experiments from medium to high mass ion irradiations can be directly compared. At lower damage levels more caution is needed. If identical integral dpa values are used, a similar D retention can be expected from the irradiation by medium to high mass ions.

Heavy ion irradiation is often used for simulating the displacement damage by 14 MeV neutrons. This is justified by the fact that neutrons produce similar large, dense cascades in tungsten as heavy ions. However, there are significant differences of primary recoil energies between 14 MeV neutron irradiation and heavy ion irradiation. The maximum recoil energy of a tungsten atom after a head on collision with a 14 MeV neutron is about 290 keV, while the maximum primary recoil energies ranged from 3.5 MeV in Si irradiation to 20 MeV in W irradiation in this study. Nevertheless, despite the difference in the recoil energy spectrum, the D retention and the dislocation structure was very similar for medium to high mass ions (Si, Fe, Cu, W). No dependence of the primary recoil energy spectrum on the D retention was found. Molecular dynamics (MD) simulations have shown that cascades from high energetic recoils (>150 keV) tend to split into smaller subcascades, with typical energies lower than 200 keV within the cascades [38]. Hence, the high-energy part of the recoil energy spectrum will lead to similar types of defects. The subcascade splitting is an explanation why the samples irradiated with different medium to high mass ions show similar D retention. MD calculations from [33] have demonstrated that these energetic cascades in tungsten frequently produce large defect clusters [33]. For the H, D and He irradiations in this work the recoil energies never come close to 150 keV, and hence the athermal formation of large clusters in the primary damage is very unlikely. This would explain the significantly different D retention and dislocation structure found in tungsten irradiatedy by light ions. The above considerations and the presented results of this work suggest that neutron irradiation of tungsten will result in a similar D retention and displacement damage

as in tungsten irradiated by medium to high mass ions. Hence the use of heavy ions to simulate displacement damage by neutrons seems justified.

7.2 Outlook

The work presented here points to several research directions for the future. Here, only a short description of few possible projects is given.
As mentioned in the discussion of the TEM observations in Sect. 5.1.7, it is not fully clear whether the four zones observed in tungsten after light ion irradiations are due to the significant differences in the recoil spectra in the given depth interval, or due to the lower damage rate, or simply due to differences in the damage depth profiles. To adress this question further self-irradiation of tungsten to different damage levels with low ions currents ,to obtain a small damage rate, would be needed. A subsequent TEM analysis of the dislocation structure and MD simulations of the recoil energy spectra at given depth intervalls could give the answer.
The observation of the dislocation structure and D retention in tungsten irradiated by He raises the following questions: Will the dislocation loops in tungsten irradiated by He join at a certain damage level to lines? Will D saturate at this damage level? To adress this questions several He irradiations of tungsten to different damage levels and subsequent TEM analysis would be needed. Through the investigation of the dislocation structure of the damage zone and the He bubbles in these samples, interesting facts about the dislocation and He bubble behavior in tungsten could be obtained.
It is known that at high temperatures, voids are formed due to the onset of vacancy and vacancy cluster mobility. It would be very interesting to irradiate tungsten with heavy ions at higher temperatures and to investigate the damage zone with TEM. This would give some information about the dislocation behavior at higher temperatures which might be interesting for simulating the neutron damage in a future fusion reactor.

Bibliography

[1] International Energy Agency, IAE, *World Energy Outlook 2017*, IEA, Paris (2017).

[2] J. Ongena and G. Van Oost, *Energy for Future Centuries: Will Fusion be an Inexhaustible, Safe and Clean Energy Source?*, Fusion Science and Technology **41**, 3 (2002).

[3] A. M. Bradshaw, T. Hamacher and U. Fischer, *Is nuclear fusion a sustainable energy form?*, Fusion Engineering and Design **86**, 2770 (2011).

[4] U. Stroth, *Fusionsforschung*, in *Plasmaphysik: Phänomene, Grundlagen und Anwendungen* (Springer, Berlin, Heidelberg, 2018) Chap. Fusionsforschung, pp. 343–361.

[5] M. Keilhacker et al., *High fusion performance from deuterium-tritium plasmas in JET*, Nuclear Fusion **39**, 209 (1999).

[6] G. Federici et al., *European DEMO design strategy and consequences for materials*, Nuclear Fusion **57**, 092002 (2017).

[7] J. Roth et al., *Recent analysis of key plasma wall interactions issues for ITER*, Journal of Nuclear Materials **390-391**, 1 (2009).

[8] G. Federici et al., *Assessment of erosion and tritium codeposition in ITER-FEAT*, Journal of Nuclear Materials **290-293**, 260 (2001).

[9] J. Roth and K. Schmid, *Hydrogen in tungsten as plasma-facing material*, Physica Scripta **2011**, 014031 (2011).

[10] M. '. t Hoen et al., *Saturation of deuterium retention in self-damaged tungsten exposed to high-flux plasmas*, Nuclear Fusion **52**, 023008 (2012).

[11] J. Knaster, A. Möslang and T. Muroga, *Materials research for fusion*, *Nature Physics*, **12**, 424 (2016).

[12] G. S. Was, *Fundamentals of Radiation Materials Science Metalls and Alloys* (Springer-Verlag Berlin Heidelberg, 2010).

[13] O. Ogorodnikova and V. Gann, *Simulation of neutron-induced damage in tungsten by irradiation with energetic self-ions*, Journal of Nuclear Materials **460**, 60 (2015).

[14] P. Vladimirov and S. Bouffard, *Displacement damage and transmutations in metals under neutron and proton irradiation*, Comptes Rendus Physique **9**, 303 (2008).

[15] B. Tyburska et al., *Deuterium retention in self-damaged tungsten*, Journal of Nuclear Materials **395**, 150 (2009).

[16] O. V. Ogorodnikova et al., *The influence of radiation damage on the plasma-induced deuterium retention in self-implanted tungsten*, Journal of Nuclear Materials **415**, S661 (2011).

[17] G. M. Wright et al., *Hydrogenic retention in irradiated tungsten exposed to high-flux plasma*, Nuclear Fusion **50**, 075006 (2010).

[18] W. R. Wampler and R. P. Doerner, *The influence of displacement damage on deuterium retention in tungsten exposed to plasma*, Nuclear Fusion **49**, 115023 (2009).

[19] M. Fukumoto et al., *Deuterium trapping in tungsten damaged by high-energy hydrogen ion irradiation*, Journal of Nuclear Materials **390-391**, 572 (2009).

[20] $https://www.tf.uni-kiel.de/matwis/amat/def\_en/$.

[21] D. Hull and D. J. Bacon, *Introduction to dislocations* (Elsevier Ltd., 2011).

[22] M. T. Robinson, *Basic physics of radiation damage production*, Journal of Nuclear Materials **216**, 1 (1994).

[23] P. Vajda, *Anisotropy of electron radiation damage in metal crystals*, Rev. Mod. Phys. **49**, 481 (1977).

[24] F. Maury et al., *Frenkel pair creation and stage I recovery in W crystals irradiated near threshold*, Radiation Effects **38**, 53 (1978).

[25] *Standard Practice for Neutron Radiation Damage Simulation by Charge-Particle Irradiation*, Tech. Rep. (ASTM E521-96(2009)e2 ASTM International, West Conshohocken, PA, 2009).

[26] R. S. Averback, *Atomic displacement processes in irradiated metals*, Journal of Nuclear Materials **216**, 49 (1994).

[27] G. H. Kinchin and R. S. Pease, *The Displacement of Atoms in Solids by Radiation*, Reports on Progress in Physics **18**, 1 (1955).

[28] M. J. Norgett, M. T. Robinson and I. M. Torrens, *A proposed method of calculating displacement dose rates*, Nuclear Engineering and Design **33**, 50 (1975).

[29] K. H. Nordlund et al., *Primary Radiation Damage in Materials Review of Current Understanding and Proposed New Standard Displacement Damage Model to Incorporate in Cascade Defect Production Efficiency and Mixing Effects*, OECD Nuclear Energy Agency (2015).

[30] D. Frenkel and B. Smit, in *Understanding Molecular Simulation*, edited by D. Frenkel and B. Smit (Academic Press, San Diego, 2002) 2nd ed., pp. 63 – 107.

[31] M. Mayer et al., *Ion beam analysis of fusion plasma-facing materials and components: Facilities and research challenges*, Nuclear Fusion **60** (2019).

[32] K. Nordlund et al., *Improving atomic displacement and replacement calculations with physically realistic damage models*, Nature Communications **9** (2018).

[33] A. E. Sand, S. L. Dudarev and K. Nordlund, *High-energy collision cascades in tungsten: Dislocation loops structure and clustering scaling laws*, EPL (Europhysics Letters) **103**, 46003 (2013).

[34] A. E. Sand, K. Nordlund and S. L. Dudarev, *Radiation damage production in massive cascades initiated by fusion neutrons in tungsten*, Journal of Nuclear Materials **455**, 207 (2014).

[35] X. Yi et al., *In situ study of self-ion irradiation damage in W and W-5Re at 500° C*, Philosophical Magazine **93**, 1715 (2013).

[36] X. Yi et al., *In-situ TEM studies of 150 keV W^+ ion irradiated W and W-alloys: Damage production and microstructural evolution*, Acta Materialia **112**, 105 (2016).

[37] A. E. Sand et al., *Cascade fragmentation: deviation from power law in primary radiation damage*, Materials Research Letters **5**, 357 (2017).

[38] A. D. Backer et al., *Subcascade formation and defect cluster size scaling in high-energy collision events in metals*, EPL (Europhysics Letters) **115**, 26001 (2016).

[39] X. Yi et al., *Direct observation of size scaling and elastic interaction between nano-scale defects in collision cascades*, EPL (Europhysics Letters) **110**, 36001 (2015).

[40] F. Ferroni et al., *High temperature annealing of ion irradiated tungsten*, Acta Materialia **90**, 380 (2015).

[41] P. Ehrhart, *Defect reactions and annealing stages: Datasheet from Landolt-Börnstein - Group III Condensed Matter · Volume 25: "Atomic Defects in Metals" in Springer Materials*, Springer, Berlin Heidelberg (1991).

[42] X. Yi et al., *Characterisation of radiation damage in W and W-based alloys from 2MeV self-ion near-bulk implantations*, Acta Materialia **92**, 163 (2015).

[43] L. Ciupiński et al., *TEM observations of radiation damage in tungsten irradiated by 20MeV W ions*, Nuclear Instruments and Methods in Physics Research Section B: Beam Interactions with Materials and Atoms **317**, 159 (2013).

[44] J. Grzonka et al., *Electron microscopy observations of radiation damage in irradiated and annealed tungsten*, Nuclear Instruments and Methods in Physics Research Section B: Beam Interactions with Materials and Atoms **340**, 27 (2014).

[45] O. V. Ogorodnikova et al., *Annealing of radiation-induced defects in tungsten: Positron annihilation spectroscopy study*, Journal of Nuclear Materials **517**, 148 (2019).

[46] M. Zibrov, *The Influence of Radiation, Mechanical,and Plasma-Induced Damage onDeuterium Retention in Tungsten*, Ph.D. thesis, Technische Universität München and Universiteit Gent (2018).

[47] H. Eleveld and A. van Veen, *Void growth and thermal desorption of deuterium from voids in tungsten*, Journal of Nuclear Materials **212-215**, 1421 (1994).

[48] A. Debelle, M. F. Barthe and T. Sauvage, *First temperature stage evolution of irradiation-induced defects in tungsten studied by positron annihilation spectroscopy*, Journal of Nuclear Materials **376**, 216 (2008).

[49] E. Markina et al., *Recovery temperatures of defects in tungsten created by self-implantation*, Journal of Nuclear Materials **463**, 329 (2015).

[50] S. A. Ryabtsev et al., *On the annealing of radiation-induced point defects in tungsten*, Journal of Surface Investigation. X-ray, Synchrotron and Neutron Techniques **10**, 658 (2016).

[51] M. R. Gilbert et al., *Inventory Simulations under Neutron Irradiation: Visualization Techniques as an Aid to Materials Design*, Nuclear Science and Engineering **177**, 291 (2014).

[52] T. Noda, M. Fujita and M. Okada, *Transmutation and induced radioactivity of W in the armor and first wall of fusion reactors*, Journal of Nuclear Materials **258-263**, 934 (1998).

[53] T. Tanno et al., *Effects of transmutation elements on the microstructural evolution and electrical resistivity of neutron-irradiated tungsten*, Journal of Nuclear Materials **386-388**, 218 (2009).

[54] M. Fujitsuka et al., *Effect of neutron irradiation on thermal diffusivity of tungsten–rhenium alloys*, Journal of Nuclear Materials **283-287**, 1148 (2000).

[55] M. R. Gilbert et al., *Neutron-induced dpa, transmutations, gas production, and helium embrittlement of fusion materials*, Journal of Nuclear Materials **442**, S755 (2013).

[56] J. Knaster et al., *Overview of the IFMIF/EVEDA project*, Nuclear Fusion **57**, 102016 (2017).

[57] S. Zinkle and L. Snead, *Opportunities and limitations for ion beams in radiation effects studies: Bridging critical gaps between charged particle and neutron irradiations*, Scripta Materialia **143**, 154 (2018).

[58] L. K. Mansur, *Theory and experimental background on dimensional changes in irradiated alloys*, Journal of Nuclear Materials **216**, 97 (1994).

[59] L. K. Mansur, *Correlation of neutron and heavy-ion damage: II. The predicted temperature shift if swelling with changes in radiation dose rate*, Journal of Nuclear Materials **78**, 156 (1978).

[60] E. H. Lee, N. H. Packan and L. K. Mansur, *Effects of pulsed dual-ion irradiation on phase transformations and microstructure in Ti-modified austenitic alloy*, Journal of Nuclear Materials **117**, 123 (1983).

[61] J. G. Gigax et al., *The influence of ion beam rastering on the swelling of self-ion irradiated pure iron at 450 °C*, Journal of Nuclear Materials **465**, 343 (2015).

[62] E. P. Simonen, N. M. Ghoniem and N. H. Packan, *Pulsed flux effects on radiation damage*, Journal of Nuclear Materials **122**, 391 (1984).

[63] R. W. Harrison, *On the use of ion beams to emulate the neutron irradiation behaviour of tungsten*, Vacuum **160**, 355 (2019).

[64] R. Harrison, G. Greaves and S. D. J.A. Hinks, *Engineering self-organising helium bubble lattices in tungsten*, Scientific Reports SP **7** (2017).

[65] P. B. Johnson and D. J. Mazey, *Gas-bubble superlattice formation in bcc metals*, Journal of Nuclear Materials **218**, 273 (1995).

[66] P. B. Johnson and D. J. Mazey, *Hydrogen gas-bubble structure in proton-irradiated copper at 300 K*, Journal of Nuclear Materials **91**, 41 (1980).

[67] R. Rayaprolu et al., *Simulation of neutron irradiation damage in tungsten using higher energy protons*, Nuclear Materials and Energy **9**, 29 (2016).

[68] M. Shimada et al., *Overview of the US–Japan collaborative investigation on hydrogen isotope retention in neutron-irradiated and ion-damaged tungsten*, Fusion Engineering and Design **87**, 1166 (2012).

[69] P. N. Maya et al., *Evaluation of tungsten as divertor plasma-facing material: results from ion irradiation experiments and computer simulations*, Nuclear Fusion **59**, 076034 (2019).

[70] Y. Oya et al., *Recent progress of hydrogen isotope behavior studies for neutron or heavy ion damaged W*, Fusion Engineering and Design **113**, 211 (2016).

[71] O. El-Atwani et al., *In-situ TEM/heavy ion irradiation on ultrafine-and nanocrystalline-grained tungsten: Effect of 3MeV Si, Cu and W ions*, Materials Characterization **99**, 68 (2015).

[72] V. Alimov, J. Roth and M. Mayer, *Depth distribution of deuterium in single- and polycrystalline tungsten up to depths of several micrometers*, Journal of Nuclear Materials **337-339**, 619 (2005).

[73] Y.-W. You et al., *Dissolving, trapping and detrapping mechanisms of hydrogen in bcc and fcc transition metals*, AIP Advances **3**, 012118 (2013).

[74] W. Möller and J. Roth, *Physics of Plasma-Wall Interactions in Controlled Fusion*, in *Physics of Plasma-Wall Interactions in Controlled Fusion*, edited by D. E. Post and R. Behrisch (Springer US, Boston, MA, 1986) Chap. Implantation, Retention and Release of Hydrogen Isotopes in Solids, pp. 439–494.

[75] A. A. Haasz, M. Poon and J. Davis, *The effect of ion damage on deuterium trapping in tungsten*, Journal of Nuclear Materials **266-269**, 520 (1999).

[76] G.-H. Lu, H.-B. Zhou and C. S. Becquart, *A review of modelling and simulation of hydrogen behaviour in tungsten at different scales*, Nuclear Fusion **54**, 086001 (2014).

[77] H. D. Cabstanjen, *Interstitial positions and vibrational amplitudes of hydrogen in metals investigated by fast ion channeling*, physica status solidi (a) **59**, 11 (1980).

[78] R. Frauenfelder, *Solution and Diffusion of Hydrogen in Tungsten*, Journal of Vacuum Science and Technology **6**, 388 (1969).

[79] N. Fernandez, Y. Ferro and D. Kato, *Hydrogen diffusion and vacancies formation in tungsten: Density Functional Theory calculations and statistical models*, Acta Materialia **94**, 307 (2015).

[80] K. Heinola and T. Ahlgren, *Diffusion of hydrogen in bcc tungsten studied with first principle calculations*, Journal of Applied Physics **107**, 113531 (2010).

[81] R. A. Causey, *Hydrogen isotope retention and recycling in fusion reactor plasma-facing components*, Journal of Nuclear Materials **300**, 91 (2002).

[82] V. S. Efimov, Y. M. Gasparyan and A. A. Pisarev, *Investigation of a fine structure of deuterium thermal desorption spectra from tungsten*, Journal of Surface Investigation. X-ray, Synchrotron and Neutron Techniques **7**, 472 (2013).

[83] H. Eleveld and A. van Veen, *Deuterium interaction with impurities in tungsten studied with TDS*, Journal of Nuclear Materials **191-194**, 433 (1992).

[84] M. Poon, A. A. Haasz and J. W. Davis, *Modelling deuterium release during thermal desorption of D^+-irradiated tungsten*, Journal of Nuclear Materials **374**, 390 (2008).

[85] M. Zibrov et al., *Experimental determination of the deuterium binding energy with vacancies in tungsten*, Journal of Nuclear Materials **477**, 292 (2016).

[86] K. Heinola et al., *Hydrogen interaction with point defects in tungsten*, Phys. Rev. B **82**, 094102 (2010).

[87] D. F. Johnson and E. A. Carter, *Hydrogen in tungsten: Absorption, diffusion, vacancy trapping, and decohesion*, Journal of Materials Research **25**, 315–327 (2010).

[88] K. Schmid, U. von Toussaint and T. Schwarz-Selinger, *Transport of hydrogen in metals with occupancy dependent trap energies*, Journal of Applied Physics **116(13)** (2014).

[89] Y. Gasparyan et al., *Deuterium ion-driven permeation and bulk retention in tungsten*, Journal of Nuclear Materials **417**, 540 (2011).

[90] S. Ryabtsev et al., *Deuterium thermal desorption from vacancy clusters in tungsten*, Nuclear Instruments and Methods in Physics Research Section B: Beam Interactions with Materials and Atoms **382**, 101 (2016).

[91] A. Manhard, *Deuterium Inventory inTungsten After Plasma Exposure: A Microstructural Survey*, Ph.D. thesis, Universität Augsburg (2011).

[92] A. Bakaev et al., *Trapping of hydrogen and helium at dislocations in tungsten: ab initio study*, Nuclear Fusion **57**, 126040 (2017).

[93] A. D. Backer et al., *Multiscale modelling of the interaction of hydrogen with interstitial defects and dislocations in BCC tungsten*, Nuclear Fusion **58**, 016006 (2017).

[94] A. McNaab and P.Foster, *A new analysis of the diffusion of hydrogen in iron and ferritic steels*, Transactions of the Metallurgical Society of AIME **227**, 618 (1963).

[95] E. A. Hodille et al., *Macroscopic rate equation modeling of trapping/detrapping of hydrogen isotopes in tungsten materials*, Journal of Nuclear Materials **467**, 424 (2015).

[96] K. Schmid et al., *Recent progress in the understanding of H transport and trapping in W*, Physica Scripta **T170**, 014037 (2017).

[97] R. Bisson et al., *Dynamic fuel retention in tokamak wall materials: An in situ laboratory study of deuterium release from polycrystalline tungsten at room temperature*, Journal of Nuclear Materials **467**, 432 (2015).

[98] G.R.Longhurst, *TMAP7 User Manual*, Idaho National Engineering and Environmental LaboratoryBechtel BWXT Idaho, LLC (2008).

[99] K. Schmid, V. Rieger and A. Manhard, *Comparison of hydrogen retention in W and W/Ta alloys*, Journal of Nuclear Materials **426**, 247 (2012).

[100] K. Schmid, *Diffusion-trapping modelling of hydrogen recycling in tungsten under ELM-like heat loads*, Physica Scripta **T167**, 014025 (2016).

[101] E. A. Hodille et al., *Simulations of atomic deuterium exposure in self-damaged tungsten*, Nuclear Fusion **57**, 056002 (2017).

[102] R. Piechoczek et al., *Deuterium trapping and release in Be(0001), Be(11–20) and polycrystalline beryllium*, Journal of Nuclear Materials **438**, S1072 (2013).

[103] A. A. Pisarev, O. V. Ogorodnikova and M. O. Titkov, *Plasma driven tritium uptake and leakage through plasma facing materials*, Fusion Engineering and Design **41**, 103 (1998).

[104] M. '. Hoen et al., *Surface morphology and deuterium retention of tungsten after low- and high-flux deuterium plasma exposure*, Nuclear Fusion **54**, 083014 (2014).

[105] L. Buzi et al., *Influence of tungsten microstructure and ion flux on deuterium plasma-induced surface modifications and deuterium retention*, Journal of Nuclear Materials **463**, 320 (2015).

[106] O. Ogorodnikova and V. Gann, *Simulation of neutron-induced damage in tungsten by irradiation with energetic self-ions*, Journal of Nuclear Materials **460**, 60 (2015).

[107] V. Alimov et al., *Deuterium retention in tungsten damaged with W ions to various damage levels*, Journal of Nuclear Materials **441**, 280 (2013).

[108] T. Schwarz-Selinger, *private communication*.

[109] V. G. Glebovsky, V. N. Semenov and V. V. Lomeyko, *Influence of the crystallization conditions on the structural perfection of molybdenum and tungsten single crystals*, Journal of Crystal Growth **87**, 142 (1988).

[110] V. Glebovsky, *Crystal Growth: Substructure and Recrystallization Ch. 4 in Recrystallization*, edited by K. Sztwiertnia (IntechOpen, Rijeka, 2012).

[111] *PLANSEE Metall GmbH - High Perfomance Materials, Austria*.

[112] A. Manhard, M. Balden and S. Elgeti, *Quantitative Microstructure and Defect Density Analysis of Polycrystalline Tungsten Reference Samples after Different Heat Treatments*, Practical Metallography (2015).

[113] T. Schwarz-Selinger, *Deuterium retention in MeV self-implanted tungsten: Influence of damaging dose rate*, Nuclear Materials and Energy **12**, 683 (2017).

[114] A. Manhard et al., *Microstructure and defect analysis in the vicinity of blisters in polycrystalline tungsten*, Nuclear Materials and Energy **12**, 714 (2017).

[115] P. Bazarnik, *The role of grain boundaries on the mechanical properties in aluminium alloy 5483 obtained by different severe plastic deformation methods*, Ph.D. thesis, Warsaw University of Technology (2017).

[116] D. B. Williams and C. B. Carter, *Transmission Electron Microscopy, A Textbook for Materials Science* (Springer Science + Business Media New York, 1996).

[117] J. W. Edington, *Practical Electron Microscopy in Materials Science, Monograph One, The operation and calibration of the electron microscope* (MACMILLAN Philips Technical Library, 1974).

[118] J. W. Edington, *Practical Electron Microscopy in Materials Science, Monograph Two, Electron Diffraction in the Electron Microscope* (MACMILLAN Philips Technical Library, 1974).

[119] M. L. Jenkins, *Characterisation of radiation-damage microstructures by TEM*, Journal of Nuclear Materials **216**, 124 (1994).

[120] A. Prokhodtseva et al., *Impact of He and Cr on defect accumulation in ion-irradiated ultrahigh-purity Fe(Cr) alloys*, Acta Materialia **61**, 6958 (2013).

[121] B. L. Eyre and R. Bullough, *On the formation of interstitial loops in b.c.c. metals*, The Philosophical Magazine: A Journal of Theoretical Experimental and Applied Physics **12**, 31 (1965).

[122] W. Jäger and M. Wilkens, *Formation of vacancy-type dislocation loops in tungsten bombarded by 60 keV Au ions*, physica status solidi (a) **32**, 89 (1975).

[123] B. C. Masters, *Dislocation loops in irradiated iron*, The Philosophical Magazine: A Journal of Theoretical Experimental and Applied Physics **11**, 881 (1965).

[124] D. M. Norfleet et al., *Dislocation structures and their relationship to strength in deformed nickel microcrystals*, Acta Materialia **56**, 2988 (2008).

[125] H. O. U. Martin, U. Mühle, *The Qunatitative Measurement of Dislocation Density in the Transmission Electron Microscope*, Prakt. Metallogr. 32 (1995).

[126] J. Čížek, *Characterization of lattice defects in metallic materials by positron annihilation spectroscopy: A review*, Journal of Materials Science & Technology **34**, 577 (2018).

[127] W. Egger, *Physics with many positrons: Proceedings of the International School of Physics "Enrico Fermi" Course CLXXIV*, edited by A. D. R. Brusa and A. A. Mills IOS Press, Vol. p.416 (2010).

[128] P. J. Schultz and K. G. Lynn, *Interaction of positron beams with surfaces, thin films, and interfaces*, Rev. Mod. Phys. **60**, 701 (1988).

[129] T. Troev et al., *Positron simulations of defects in tungsten containing hydrogen and helium*, Nuclear Instruments and Methods in Physics Research Section B: Beam Interactions with Materials and Atoms **267**, 535 (2009).

[130] C. Hugenschmidt et al., *The NEPOMUC upgrade and advanced positron beam experiments*, New Journal of Physics **14**, 055027 (2012).

[131] P. Sperr et al., *Status of the pulsed low energy positron beam system (PLEPS) at the Munich Research Reactor FRM-II*, Applied Surface Science **255**, 35 (2008).

[132] A. Manhard, T. Schwarz-Selinger and W. Jacob, *Quantification of the deuterium ion fluxes from a plasma source*, Plasma Sources Science and Technology **20**, 015010 (2011).

[133] J. Bauer et al., *Influence of near-surface blisters on deuterium transport in tungsten*, Nuclear Fusion **57**, 086015 (2017).

[134] M. Mayer et al., *Quantitative Depth Profiling of Deuterium up to very Large Depths*, Nuclear Instruments and Methods in Physics Research Section B **267**, 506 (2009).

[135] V. K. Alimov, M. Mayer and J. Roth, *Differential cross-section of the D(^{3}He,p)^{4}He nuclear reaction and depth profiling of deuterium up to large depths*, Nuclear Instruments and Methods in Physics Research Section B: Beam Interactions with Materials and Atoms **234**, 169 (2005).

[136] B. Wielunska et al., *Cross section data for the D(^{3}He,p)^{4}He nuclear reaction from 0.25 to 6MeV*, Nuclear Instruments and Methods in Physics Research Section B: Beam Interactions with Materials and Atoms **371**, 41 (2016).

[137] H. S. Bosch and G. M. Hale, *Improved Formulas for Fusion Cross Sections and Thermal Reactivites*, Nuclear Fusion **32**, 111 (1992).

[138] M. Mayer, *SIMNRA user's guide* (Tech. Rep. IPP 9/113. Garching: Max-Planck-Institut fur Plasmaphysik, 1997).

[139] K. Schmid and U. von Toussaint, *Statistically sound evaluation of trace element depth profiles by ion beam analysis*, Nuclear Instruments and Methods in Physics Research Section B: Beam Interactions with Materials and Atoms **281**, 64 (2012).

[140] M. Mayer, *RESOLNRA: A new program for optimizing the achievable depth resolution of ion beam analysis methods*, Nuclear Instruments and Methods in Physics Research Section B: Beam Interactions with Materials and Atoms **266**, 1852 (2008).

[141] S. Kapser, *Deuterium Permeation Through Tungsten Driven by Plasma-Based Low-Energy Ion Implantation*, Ph.D. thesis, Technische Universtät München, Fakultät für Physik (2018).

[142] M. Zibrov et al., *Deuterium trapping by deformation-induced defects in tungsten*, Nuclear Fusion **59**, 106056 (2019).

[143] W. Möller and F. Besenbacher, *A note on the ^3He + D nuclear-reaction cross section*, Nuclear Instruments and Methods **168**, 111 (1980).

[144] E. Salançon et al., *Redeposition of amorphous hydrogenated carbon films during thermal decomposition*, Journal of Nuclear Materials **376**, 160 (2008).

[145] J. F. Ziegler, J. P. Biersack and M. D. Ziegler, *The Stopping and Range of Ions in Matter* (SRIM co., 2008).

[146] R. S. Averback and T. Diaz de la Rubia, *Displacement Damage in Irradiated Metals and Semiconductors*, *Solid State Physics*, (1998).

[147] R. E. Stoller et al., *On the use of SRIM for computing radiation damage exposure*, Nuclear Instruments and Methods in Physics Research Section B: Beam Interactions with Materials and Atoms **310**, 75 (2013).

[148] K. Nordlund, *Molecular dynamics simulation of ion ranges in the 1–100 keV energy range*, Computational Materials Science **3**, 448 (1995).

[149] J. F. Ziegler, U. Littmark and J. P. Biersack, *The stopping and range of ions in solids*, Vol. p.321 (Pergamon New York, 1985).

[150] M. R. Gilbert, J. Marian and J.-C. Sublet, *Energy spectra of primary knock-on atoms under neutron irradiation*, Journal of Nuclear Materials **467**, 121 (2015).

[151] M. Miyamoto et al., *Systematic investigation of the formation behavior of helium bubbles in tungsten*, Journal of Nuclear Materials **463**, 333 (2015).

[152] V. T. Astrelin et al., *Blistering of the selected materials irradiated by intense 200 keV proton beam*, Journal of Nuclear Materials **396**, 43 (2010).

[153] N. Enomoto et al., *Grazing-incidence electron microscopy of surface blisters in single- and polycrystalline tungsten formed by H^+, D^+ and He^+ irradiation*, Journal of Nuclear Materials **385**, 606 (2009).

[154] W. Wang et al., *Blister formation of tungsten due to ion bombardment*, Journal of Nuclear Materials **299**, 124 (2001).

[155] I. N. Bronshtein et al., *Handbook of Mathematics* (Springer Berlin Heidelberg, 2015).

[156] R. Kobayashi et al., *A molecular dynamics study on bubble growth in tungsten under helium irradiation*, Journal of Nuclear Materials **463**, 1071 (2015).

[157] X. Yi et al., *A study of helium bubble production in 10 keV He^+ irradiated tungsten*, Fusion Engineering and Design **125**, 454 (2017).

[158] T. Wejrzanowski and K. J. Kurzydlowski, in *Interfacial Effects and Novel Properties of Nanomaterials*, Solid State Phenomena, Vol. 94 (Trans Tech Publications Ltd, 2003) pp. 221–228.

[159] T. Wejrzanowski, M. Lewandowska and K. J. Kurzydłowski, *Stereology of nano-materials*, Image Analysis & Stereology **29**, 1 (2010).

[160] W. Chrominski et al., *TEM investigation of the influence of dose rate on radiation damage and deuterium retention in tungsten*, Materials Characterization **154**, 1 (2019).

[161] S. Markelj, T. Schwarz-Selinger and A. Založnik, *Hydrogen isotope accumulation in the helium implantation zone in tungsten*, Nuclear Fusion **57**, 064002 (2017).

[162] N. Juslin and B. D. Wirth, *Molecular dynamics simulation of the effect of subsurface helium bubbles on hydrogen retention in tungsten*, Journal of Nuclear Materials **438**, S1221 (2013).

[163] N. Hashimoto et al., *Microstructural analysis on helium retention of ion-irradiated and annealed tungsten foils*, Journal of Nuclear Materials **347**, 307 (2005).

[164] S. B. Gilliam et al., *Retention and surface blistering of helium irradiated tungsten as a first wall material*, Journal of Nuclear Materials **347**, 289 (2005).

[165] A. Debelle et al., *Helium behaviour and vacancy defect distribution in helium implanted tungsten*, Journal of Nuclear Materials **362**, 181 (2007).

[166] B. Wielunska, M. Mayer and T. Schwarz-Selinger, *Optimization of the depth resolution for deuterium depth profiling up to large depths*, Nuclear Instruments and Methods in Physics Research Section B: Beam Interactions with Materials and Atoms **387**, 103 (2016).

[167] B. Wielunska, M. Mayer and T. Schwarz-Selinger, *Corrigendum to "Optimization of the depth resolution for deuterium depth profiling up to large depths" [Nucl. Instrum. Methods Phys. Res. B 387 (2016) 103–114]*, Nuclear Instruments and Methods in Physics Research Section B: Beam Interactions with Materials and Atoms **440**, 202 (2019).

[168] S. Markelj et al., *Displacement damage stabilization by hydrogen presence under simultaneous W ion damage and D ion exposure*, Nuclear Fusion **59**, 086050 (2019).

[169] A. D. Backer et al., *Hydrogen accumulation around dislocation loops and edge dislocations: from atomistic to mesoscopic scales in BCC tungsten*, Physica Scripta **T170**, 014073 (2017).

Acknowledgments

The work presented in this thesis would not have been possible without the help and support of many people. I would like to express my gratitude to all of them.

First of all, I would like to thank my academic supervisor Prof. Rudolf Neu and the head of the Plasma Edge and Wall division Prof. Ulrich Stroth for giving me the opportunity to carry out the research presented in this thesis. Despite his busy schedule, Prof. Neu always found time for scientific discussions and followed the progress of my work closely. I would especially like to thank him for his support in administrative issues related to my business travels to Poland.

I thank our group leader Dr. habil. Wolfgang Jacob for organizing and leading the work group. I am also grateful for his suggestions and corrections for this thesis.

I would like to express my gratitude to my supervisor Dr. Matej Mayer, his patience and help in solving theoretical and practical problems and to Dr. Thomas Schwarz-Selinger for the introduction to the PlaQ and TESS laboratories, the discussions and the motivation.

Many thanks to Thomas Dürbeck for his guidance in the TDS measurements. I am grateful to Joachim Dorner, Michael Fußeder and Arno Weghorn for their support in the particle accelerator laboratory and their help with my bicycle and car. I would like to thank Dr. Mikhail Zibrov for his help solving theoretical questions.

A large part of the thesis was accomplished in the framework of a collaboration between the IPP and the Faculty of Material Science and Engineering at the Technical University of Warsaw. Thanks to Prof. Lewandowska and Dr. Cuipinki for hosting me at the faculty. I also owe thanks to Dr. Tomasz Plocinski for patiently introducing me to the world of electron microscopy, and for Dr. Witold Zielinski for teaching me the operation of the transmission electron microscopes.

Thanks to Dr. Witold Chromiski and Dr. Agnieszka Krawczynska for the many discussions about transmission electron microscopy. I am also grateful to Dr. Piotr Bazarnik for his support in various issues in the microscopy laboratory.

I would like to thank all colleagues in Garching and in Warsaw for the many scientific discussions and the warm work environment.

Last but not least, I owe a big thanks to my parents, who supported me from the very beginning.